



# Orogenic development of the Adrar des Iforas (Tuareg Shield, NE Mali): New geochemical and geochronological data and geodynamic implications

Delphine Bosch, Olivier Bruguier, Renaud Caby, Francois Buscail, Dalila Hammor

## ► To cite this version:

Delphine Bosch, Olivier Bruguier, Renaud Caby, Francois Buscail, Dalila Hammor. Orogenic development of the Adrar des Iforas (Tuareg Shield, NE Mali): New geochemical and geochronological data and geodynamic implications. *Journal of Geodynamics*, 2016, 96, pp.104-130. 10.1016/j.jog.2015.09.002 . hal-01825654

HAL Id: hal-01825654

<https://hal.science/hal-01825654v1>

Submitted on 23 Oct 2024

**HAL** is a multi-disciplinary open access archive for the deposit and dissemination of scientific research documents, whether they are published or not. The documents may come from teaching and research institutions in France or abroad, or from public or private research centers.

L'archive ouverte pluridisciplinaire **HAL**, est destinée au dépôt et à la diffusion de documents scientifiques de niveau recherche, publiés ou non, émanant des établissements d'enseignement et de recherche français ou étrangers, des laboratoires publics ou privés.

# Orogenic development of the Adrar des Iforas (Tuareg Shield, NE Mali): New geochemical and geochronological data and geodynamic implications

Delphine Bosch<sup>a,\*</sup>, Olivier Bruguier<sup>a</sup>, Renaud Caby<sup>a</sup>, François Buscail<sup>b</sup>, Dalila Hammor<sup>c</sup>

<sup>a</sup> Géosciences Montpellier, CNRS-UMR 5243, Université de Montpellier, Place E. Bataillon, 34 095 Montpellier cedex 5, France

<sup>b</sup> GEOTER, Pôle GéoEnvironnement, 3 rue Jean Monnet, 34 830 Clapiers, France

<sup>c</sup> Laboratoire de Recherche Géologie, Faculté des Sciences de la Terre, Université Badji Mokhtar, BP12, Annaba 23000, Algeria

## A B S T R A C T

Laser-ablation U–Th–Pb analyses of zircon and allanite from magmatic and metamorphic rocks of the Adrar des Iforas in Northern Mali allow re-examining the relationships between the different crustal units constituting the western part of the Tuareg Shield, as well as the timing of magmatic and metamorphic events in the West Gondwana Orogen. Granulite-facies metamorphism in the Iforas Granulitic Unit (IGU) and at In Bezzeg occurred at  $1986 \pm 7$  Ma and  $1988 \pm 5$  Ma respectively. This age is slightly younger, but consistent with that of the HT granulite facies event characterizing the In Ouzzal granulitic unit (IOGU), thereby substantiating the view that these units once formed a single granulitic belt of c. 800 km long. High-grade metamorphic basement units of the Kidal terrane surrounding the IGU contain Paleoproterozoic magmatic rocks crystallized between  $1982 \pm 8$  Ma and  $1966 \pm 9$  Ma. Inherited components in these rocks (2.1 Ga and 2.3–2.5 Ga) have ages similar to that of detrital zircons at In Bezzeg and to that of basement rocks from the IGU. This is taken as evidence that the Kidal terrane and the IGU formed a single crustal block at least until 1.9 Ga. East of the Adrar fault, the Tin Essako orthogneiss is dated at  $2020 \pm 5$  Ma, but escaped granulite facies metamorphism. During the Neoproterozoic, the Kidal terrane underwent a long-lived continental margin magmatism. To the west, this terrane is bounded by the Tilemsi intra-oceanic island arc, for which a gneissic sub-alkali granite was dated at  $716 \pm 6$  Ma. A synkinematic diorite extends the magmatic activity of the arc down to  $643 \pm 4$  Ma, and, along with literature data, indicates that the Tilemsi arc has a life span of about 90 Ma. Backward docking to the western margin of the Kidal terrane is documented by migmatites dated at  $628 \pm 6$  Ma. Subduction related processes and the development of the Kidal active margin was responsible for the development of a back-arc basin in the Tafeliant area, with deposition of sediments intruded by basaltic and dacitic lavas, one of which was dated at  $623 \pm 6$  Ma. East of the IGU, in the Tamaradant domain, metagabbros and meta-anorthosites emplaced within greywackes have geochemical characteristics typical of subduction-related environments (enrichment in LILE and HFSE depletion). A metadiorite intruding the Tamaradant sediments gave an age of  $630 \pm 6$  Ma, which is tentatively taken as evidence for a Pan-African age for the subduction processes that took place east of the IGU. Collision of the Kidal terrane with the eastern margin of the West African Craton is best dated by a syncollisional tonalite, which provides an age of  $604 \pm 5$  Ma. Late kinematic processes shortly followed at  $599 \pm 4$  Ma as exemplified by the emplacement of a monzogranite belonging to the complex Central Batholith. The geochronological and geochemical evidences provided by this study allow proposing that the Kidal terrane, the IGU and Tamaradant domain of the Adrar des Iforas once belonged to a single terrane, which probably extended northward to include the IOGU, and which was later dissected by major lithospheric scale faults during the late Pan-African orogenic phases.

*Keywords:*  
Tuareg shield  
Paleo-margin  
Proterozoic  
Geochemistry  
U–Pb ages  
Mali  
Subduction  
Collision

## 1. Introduction

Part of the West Gondwana Orogen exposed in Northeast Mali constitutes a c. 300 km wide longitudinal belt parallel to the main Neoproterozoic suture (Caby et al., 2008). Along this suture, that

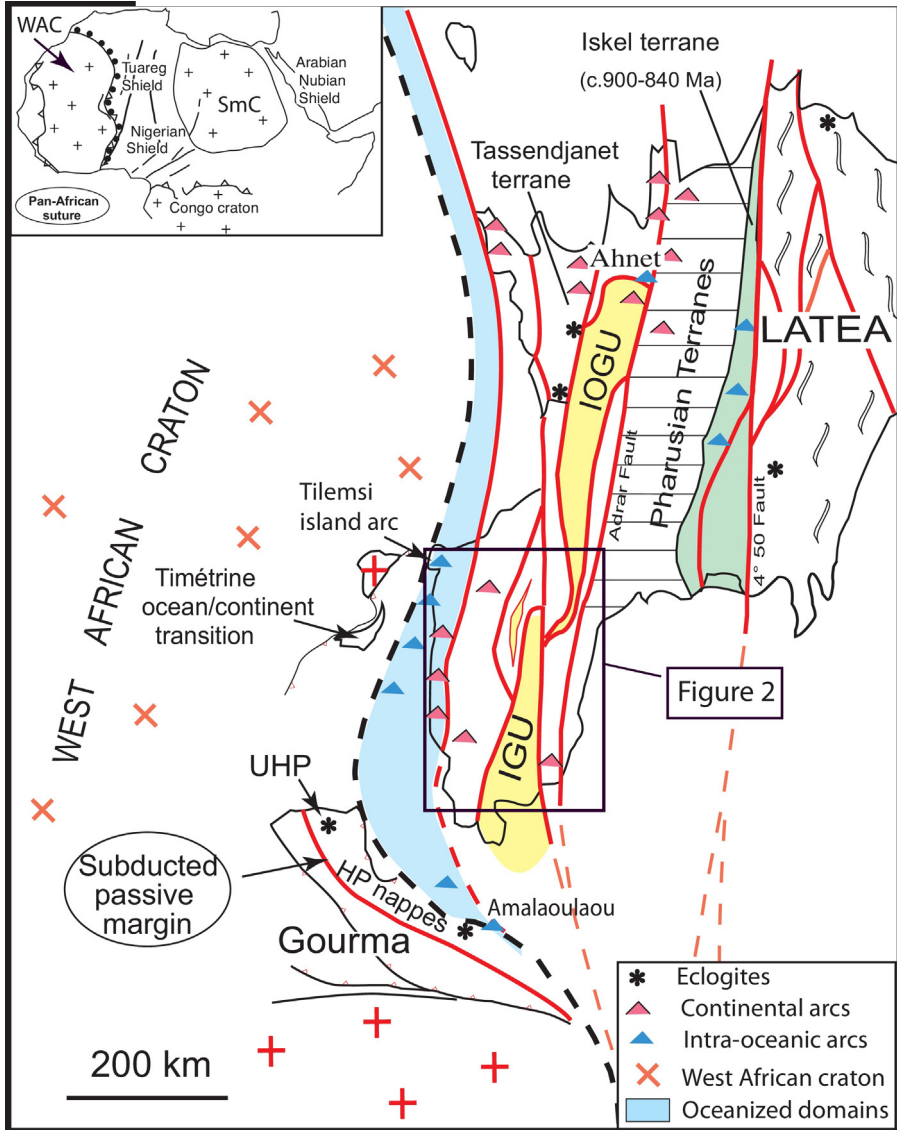


**Fig. 1.** Structural sketch map of the southwestern part of the Tuareg shield. Square corresponds to the studied area detailed in Fig. 2. Inset shows the geographical position of the studied area relative to the West African Craton (WAC).

can be traced to the south in South America, continental subduction took place simultaneously over  $\geq 2500$  km during the Ediacaran period (Ganade de Araujo et al., 2014). Black et al. (1994) proposed that the Tuareg shield ( $500,000 \text{ km}^2$ ), east of the West African Craton (WAC) is composed of amalgamated terranes separated by N-S megashear zones (Fig. 1) such as the Raghane- $8^{\circ}30'$  shear zone or the  $4^{\circ}50'$  shear zone (e.g. Nouar et al., 2011). The main relative movements of these terranes resulted from a northern transpressional tectonic escape due to their squeezing between the WAC to the west and the Saharan metacraton (SmC) to the east (Abdelsalam et al., 2002; Liégeois et al., 2013). These terranes suffered diachronous events, and final accretion was related to a long-lived history of docking and collage. This configuration hampers E-W tectonic correlations throughout the shield, but gives rise to major issues including the timing of amalgamation of these terranes, their respective tectonometamorphic evolution and their origin and possible affinities between each others. Whereas recent studies have been focussed on the Central and Eastern part of the Tuareg Shield (Central and Eastern Hoggar; e.g. Henry et al., 2009; Fezaa et al., 2010; Doukkari et al., 2014), the western part has received little attention except the

In Ouzzal terrane in the north, which is characterized by the development of ultra-high temperature ( $>900^{\circ}\text{C}$ ) metamorphism (Ouzegane et al., 2003) of Paleoproterozoic age (Peucat et al., 1996). The southwestern part of the Tuareg Shield (Adrar des Iforas) has not been the subject of recent studies due to accessibility issues. This area represents a fossil Neoproterozoic Andean-type active margin developed during subduction of the WAC beneath the western terranes of the Tuareg Shield (namely the Tassendjanet, Adrar des Iforas and In Ouzzal, see Fig. 1) (e.g. Bertrand et al., 1984; Boullier, 1986; Boullier et al., 1986; Liégeois et al., 1987). In addition the western boundary of the Adrar des Iforas hosts the suture zone between the Shield and the WAC and displays remnants of oceanic lithosphere (Tilemsi oceanic island arc in the northwestern part) that became trapped between the colliding continental landmasses. To the south, in the Gourma region, high-pressure (HP) and ultrahigh-pressure (UHP) eclogites (Caby, 1994; Caby et al., 2008) and granulite facies arc assemblages (Berger et al., 2011) are also exposed along the suture at deep crustal levels. In this paper, the geodynamic evolution of the Adrar des Iforas is reexamined in the light of new fieldwork, geochemical and geochronological (U-Th-Pb) data that allow presenting a revised evolution of this

Pan-African segment and reexamining its role in the West Gondwana assembly.

## 2. Geological Setting of the Adrar des Iforas and sampling

The Adrar des Iforas region (Fig. 1), registered the succession of Pan-African tectono-metamorphic events that ultimately resulted in the collision between the WAC and continental landmasses to the east. The western part of the belt exposed in northern Mali includes three major paleogeodynamic domains (Fig. 1): i/an active continental paleo-margin to the east (Kidal terrane) limited to the east by the Archean and Paleoproterozoic rocks of the Iforas Granulitic Unit (IGU). Both domains contain abundant pre-, syn- and post-kinematic Neoproterozoic magmatism; ii/the suture zone delineated to the north by the Tilemsi oceanic island arc and to the south by the Amalaoulaou massif (eastern Gourma). Regional considerations and comparisons with the northern Adrar des Iforas massif allow proposing that the Amalaoulaou massif represents the thrusted deeper part of an intra-oceanic arc (Berger et al., 2009, 2011) similar to the Tilemsi arc (Caby et al., 1989) that delineates the Pan-African suture in the northwestern part of the Adrar des Iforas (Caby, 2003); iii/a deformed continental passive paleo-margin (Gourma region) to the west, which is only composed of metasediments and is entirely free of any Pan-African magmatism. This domain represents the eastern edge of the WAC.

Representative samples were collected during extensive field-work carried out by several members of our team (Caby and Buscail, 2005). The location of the studied samples is presented in the geological map of Fig. 2. Samples for U-Pb geochronology include eight samples from the Kidal terrane, two samples from the Iforas Granulitic Unit (IGU) and from the In Bezzeg granulitic inlier, and two samples from the Tamaradant-Tin Essako domain, east of the IGU. Samples analyzed for trace elements and Sr-Nd isotopes include six samples from the Kidal terrane and two samples from the Tamaradant domain. The characteristics of the different parts of the Adrar des Iforas and of the studied samples are summarized below.

### 2.1. Kidal terrane

The Kidal terrane in the Adrar des Iforas constitutes, similarly to the Tassendjanet terrane of Western Hoggar, a paleo-continental active margin beneath which an oceanic domain, the Pharusian Ocean, located between the WAC and these continental blocks, disappeared by subduction. An Andean-type margin developed since c. 700 Ma (Caby, 2003), but subduction processes already affected the Pharusian ocean as early as 730–710 Ma as suggested by the age of the intra-oceanic Tilemsi island-arc (Caby et al., 1989). In the Kidal terrane, basement gneisses are clearly polymetamorphic. Prismatic sillimanite-bearing metapelites, diatexites, anatetic amphibolites and various orthogneisses among which anatetic quartz-syenitic to syenitic gneisses record a rarely well-preserved pre-Pan-African metamorphic history owing to the monocyclic greenschist facies metamorphism in the sedimentary cover. From the southwest to the northeast, a thermal metamorphic field gradient has been evidenced in this basement from upper greenschist to amphibolite facies and anatexis. Estimates calculated for peak conditions in the northern part, close to the IGU, are  $T = 700 \pm 50^\circ\text{C}$  and  $P = 10 \pm 1 \text{ kbar}$  (Champenois et al., 1987). The magmatic activity is characterized by the emplacement of subduction-related dioritic and tonalitic plutons, with ages as old as 696 Ma (Caby and Andréopoulos-Renaud, 1985). Closure of the oceanic domain and docking of the Tilemsi island arc to the Kidal terrane may have occurred at around 635 Ma (Caby, 2003). Syn-collisional, calc-alkaline granitic plutons were emplaced between 620 and

590 Ma in the Kidal terrane (Caby et al., 1985; Liégeois et al., 1987; Caby and Andréopoulos-Renaud, 1989). In the Tassendjanet terrane (Western Hoggar), syn-collisional exhumation of high-pressure units including metasediments and garnet amphibolites, previously subducted eastward beneath the IOGU, occurred at  $623 \pm 2 \text{ Ma}$  (Berger et al., 2014). This exhumation in the north is thus coeval with the oldest syn-collisional magmatism in the Kidal terrane. The age of late- to post-collisional plutons is bracketed between 595 and 545 Ma (Liégeois et al., 1987, 1996; Liégeois and Black, 1987). However, a late-kinematic pluton was dated in the Central Tuareg Shield at 523 Ma (Paquette et al., 1998), thus demonstrating that the Pan-African event *s.l.* in some structural domains includes the Cambrian period.

Samples collected for U-Pb geochronology and for major and trace elements and Sr-Nd analyses (see Fig. 2 for location) are briefly presented below.

i/The pre-Pan-African basement of the Kidal terrane is represented by sample IC622, a red anatetic orthogneiss of syenitic composition collected south of Kidal. The sample contains perthitic orthoclase, less abundant than Na-plagioclase, rare quartz, biotite, fluorite and calcite. Trails enriched in accessory minerals contain ilmenite, titanite, apatite, zircon and metamict allanite. Leucocratic bands and veins cut the tectono-metamorphic banding. Abundant calcite, zoisite, minute biotite, chlorite and severe ferroalitisation of feldspars is tentatively related to a Pan-African metamorphism. A second sample was collected east of the IGU, in the Tin Elor area (migmatitic gneiss 04-35). The sample is part of the reworked basement near Ibedouyen and belonging or adjacent to the southernmost mylonitic extremity of the IGU. The rock displays a coarse-grain porphyroblastic metamorphic/migmatitic fabric with minor post-mineral deformation. Lobate monocrystalline quartz, untwinned perthitic orthoclase displaying inclusions of euhedral plagioclase and dark brown to opaque amphibole are observed. The sample contains  $\geq 5\%$  of ilmenite in syncrystallization with amphibole. Titanite, allanite, ilmenite, apatite and zircon are accessory minerals. The leucosomes are devoid of ilmenite. Two garnet-bearing rocks were sampled north (sample 04-27A) and east (sample 04-31) of the IGU. Sample 04-31 is made up of coarse-grained garnet with a triple point magmatic microstructure with pink orthopyroxene overgrown by cummingtonite and quartz (10%) more abundant than plagioclase (<5%). Ilmenite, apatite and minute zircon are the accessory minerals. Sample 04-27A is a coarse-grained mafic rock with some parts containing up to 50% of garnet associated to green clinopyroxene, quartz (up to 10%), brown amphibole, ilmenite and rutile (Fig. 3A).

ii/Base rocks are unconformably covered by a sequence of characteristic horizons of limestones and dolomites. This sequence has been studied in details in the In Bezzeg area and is labeled here the Ourdjan Group. Above granitic gneisses the undetached basal quartzite member (20–50 m) is overlain by c. 1000 m of alternating limestones and dolomites containing rarely preserved remnants of columnar stromatolites, followed by a sequence of black shales in which acritarchs are observed (Amard, 1983). The black shales also occur as neptunian dykes cutting a massive limestone horizon containing *Conophyton* relics. This group is very similar to the “Stromatolite Series” of NW Hoggar (Caby and Monié, 2003). It is tentatively correlated with the 1.1 Ga Atar Group, the monotonous cratonic series deposited on the WAC (e.g. Rooney et al., 2010). Only marbles are preserved in the Kidal area, but at Ourdjan the carbonates are overlain by basaltic metatuffs and there is an apparent gradual passage upward into magnetite and Mn-quartzites, graphitic and pyritic schists of assumed deep sea character that are overlain in unconformity by volcanic metagreywackes. Similar quartzites, carbonates, black shales and strongly retrogressed troctolite to ultramafic sills are exposed over the c. 50 km long Ibedouyen belt (Leterrier and Bertrand, 1986). This assemblage is

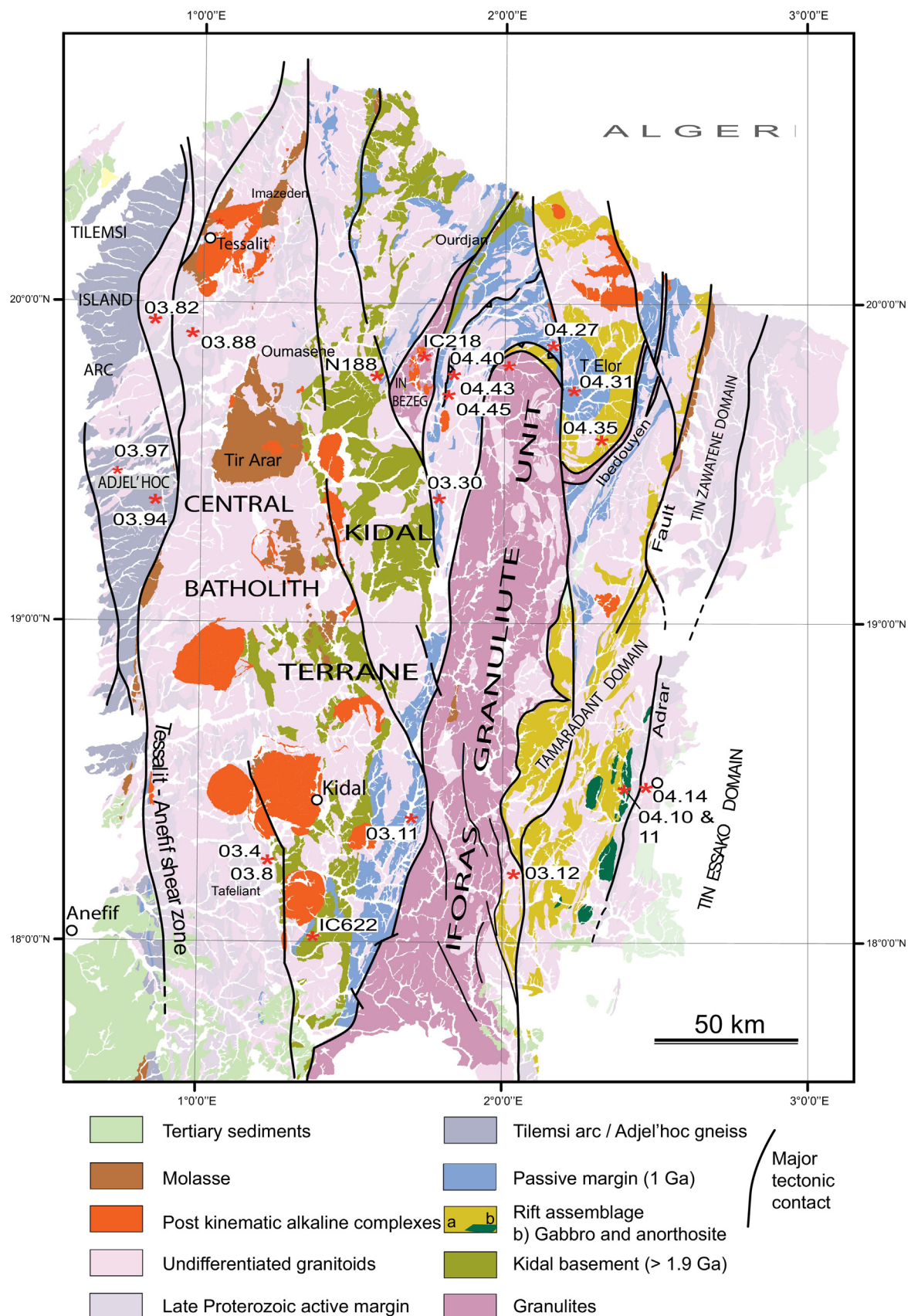
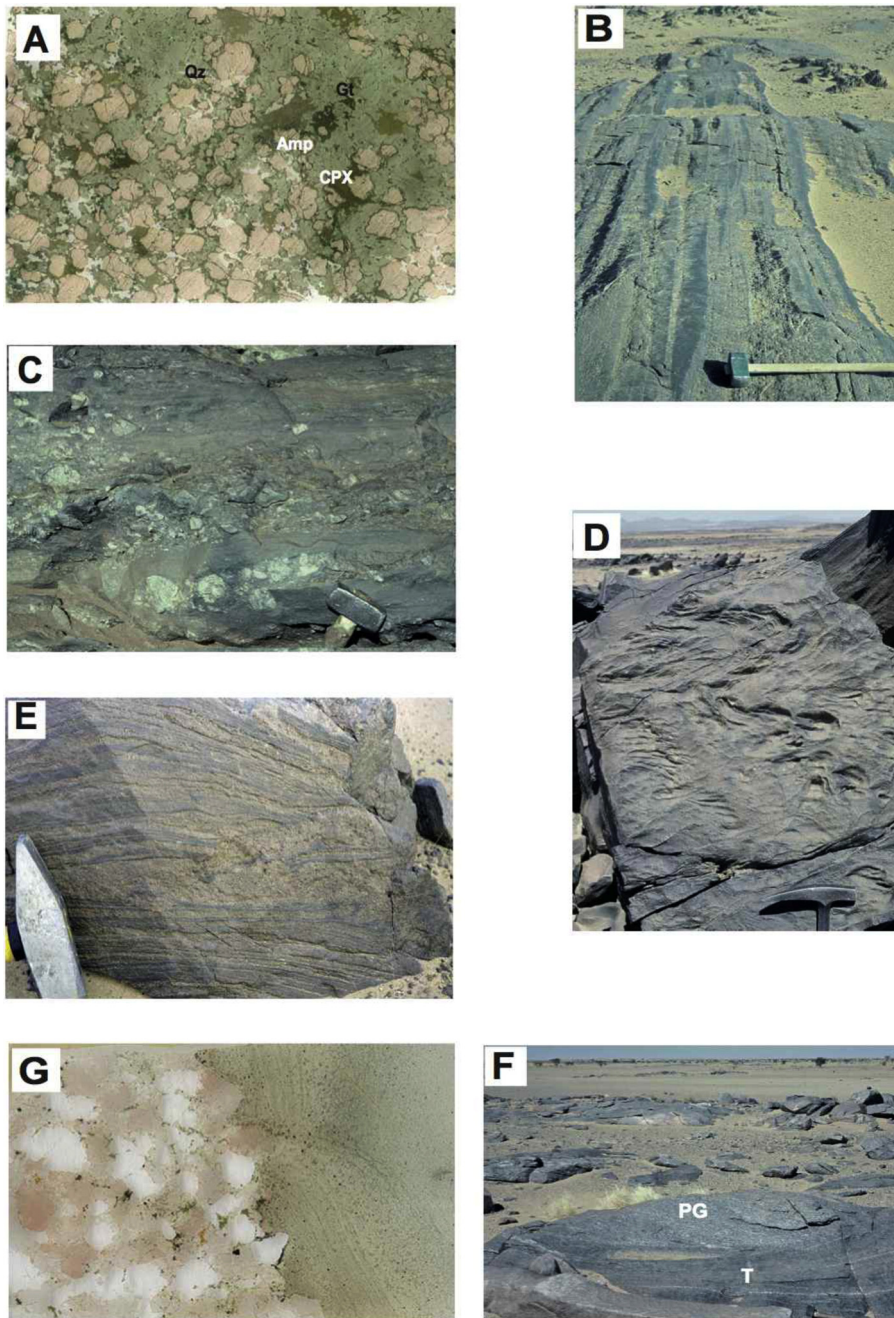


Fig. 2. Geological map of the central Adrar des Iforas massif (modified after Caby and Buscaill, 2005). Location of the studied samples is indicated.



**Fig. 3.** (A) Metabasalt 04.27A. Brown amphibole has grown after pale green pyroxene and as a reaction rim around garnet. (B) Vertical sheeted dyke complex of diorite/monzonodiorite, associated with a branch of the Tessalit-Aneif shear zone, west Tafeliant. (C) Metaconglomerate from the Tafeliant Group. (D) Slumped volcanic metagreywacke from the Tafeliant Group. (E) Horizontal amphibole-pyroxene diatexite interleaved with mafic tonalite (Oumasène). (F) Recumbent magmatic foliation in layered tonalite (T) and porphyritic granodiorite (PG), Achiou pluton (sample N188). (G) Sharp contact of undeformed monzogranite and quartz-rich hornfels (sample 03.88).

overlain in apparent continuity by polymictic conglomerates and volcanic metagreywackes though a strong difference in structural style is observed between both groups (Boullier, 1982). Such difference may relate to the synformal character of the rocks of the Ourdjan Group only affected in this belt by greenschist facies metamorphism and by two-mica-andalusite assemblages approaching the Pan-African plutons. One outlier of Proterozoic cover about 400 m thick is preserved on top of the IGU and comprises weakly recrystallized cross-bedded quartzites, siltstones and shales cut by metabasic sills. This outlier possibly represents the lowermost part of the Mesoproterozoic cover and was only affected by a faint upright pressure solution cleavage delineated

by biotite that is axial planar of N-S trending open folding coeval with greenschist facies. North of the IGU, in the Tin Elor area, basic rocks have also been described (Leterrier and Bertrand, 1986) and interpreted for some of them as basic dykes emplaced in a back-arc setting and intruding the middle Proterozoic quartzites. The  $P-T$  estimations for the deformation of these dykes have been estimated at  $700 \pm 50^\circ\text{C}$  and 10 kbar (Champenois et al., 1987). Samples analyzed for trace elements and Sr-Nd isotopes were collected west, north and northeast of the IGU (see Fig. 2). Amphibolites and metabasalts (03-11B, 03-30, 04-43 and 04-45) have been collected west of the IGU where they are intercalated in between the carbonates cover in the Kidal terrane. Samples 04-43

and 04-45 are fine-grained metabasalts corresponding to the core of pillows whereas samples 03-11B and 03-30 are amphibolites.

iii/Subduction related plutons include a sub-alkaline gneissic granite from the Adjel'Hoc gneisses (03-82) collected south of Tessalit, in a branch of the Tessalit-Anefif shear-zone which contains granites and vertical sheeted dykes of diorite/monzodiorite (Fig. 3B). The sample contains large globular quartz phenocrysts (cm size) that include orthoclase phenocrysts, which in turn contain inclusions of sub-euhedral Na-plagioclase, some of which are disposed in synneusis. Dark brown Fe biotite is less abundant than magnetite and ilmenite mostly included in quartz. The second sample is a porphyritic metadacite (03-8) collected south of Kidal in the Tafeliant Group. The sample comes from the massive part of a 3 m thick dyke crosscutting metagreywackes and spotted andalusite-cordierite metapelites of the Tafeliant Group. Fine-grained margins of the dyke suffered ductile deformation as observed from the stretched quartz phenocrysts (5 mm). Plagioclase phenocrysts (3 mm) display oscillatory zoning and brown magmatic biotite is kinked. The schistosity of the siliceous matrix is delineated by green biotite. Acicular apatite and rare fluorite are also observed. Two metabasalts (03-4A and 03-4B) from the Tafeliant Group were also collected close to the metadacite 03-08 for trace elements and Sr-Nd isotope analyses. Sample 03-4A is a porphyric metabasalt with plagioclase phenocrysts. Sample 03-4B is a fined-grained facies. Both probably constitute pillow basalt cores. The metasedimentary units of the Tafeliant Group ( $\geq 3000$  m, Fig. 3C and D) are essentially represented by metavolcanics and metagreywackes (Dostal et al., 1994) deposited in the western part of the Kidal terrane where they unconformably overlie a tonalite dated at 696 Ma (Caby and Andréopoulos-Renaud, 1985).

iv/Syn-collisional rocks are represented by two samples from the Adjel'hoc gneisses. Sample 03-97 is a foliated diorite. The sample contains quartz, green hornblende, biotite, large plagioclase and titanite. Rare chlorite and epidote are also observed. Sample 03-94 is a diatexite (Fig. 3E) containing brown biotite, plagioclase, quartz and polycrystalline cordierite. Sample N188 (Fig. 3F) was collected close to the In Bezzeg granulitic outcrop. The foliated rock displays a purely magmatic mineralogy and microstructure. Quartz, pale-green acicular augite and hornblende are included in subhedral plagioclase displaying oscillatory zoning. Rare untwinned perthitic K-feldspar includes the plagioclase with myrmekitic rims. Acicular apatite is free of deformation. Titanite, allanite and euhedral zircon are abundant.

v/The age of late kinematic intrusions was investigated through the study of sample 03-88, a pink monzogranite collected south of In Darset (Fig. 3G). The collected sample is characteristic of the central batholith considered as late to post-kinematic (in the 620–580 Ma age range) by Black et al. (1985) and Liegeois (1988) (Fig. 4A and B). The collected sample is composed of brown-green biotite, quartz, plagioclase, and rare green amphibole associated with magnetite and titanite. The crystallization of pistacite in plagioclase, of chlorite around biotite aggregates and the undulose extinction of quartz allow arguing for significant late-magmatic recrystallization and fluid infiltration possibly linked with the emplacement of post-kinematic dykes and alkaline complexes that cross-cut all the structures.

## 2.2. Iforas Granulitic Unit and In Bezzeg Granulitic inlier

The structural setting of the Iforas Granulitic Unit (IGU) is still unclear. This unit, along with other outcrops of granulitic units in the Adrar des Iforas such as In Bezzeg, is regarded by some authors as a granulitic basement nappe, thrusted over higher structural levels of the Kidal basement (Boullier et al., 1978; Boullier, 1979, 1982, 1986; Champenois et al., 1987). Alternatively, the IGU is interpreted as a slice of an Archean/Paleoproterozoic microcontinent

that may constitute a terrane distinct from the Kidal terrane and bounded by vertical lithospheric scale faults (Black et al., 1994; Caby, 1996). In both cases, the IGU is considered to be equivalent to the In Ouzzal Granulitic Unit (IOGU) in Algeria (Boullier et al., 1978). The age of high-grade metamorphism in the IGU is constrained at  $2120 \pm 20$  Ma, on the ground of U-Pb dating of zircon fractions extracted from sub-alkaline leptynites (Lancelot et al., 1983). This age is c. 120 Ma older than the age of the UHT granulite facies event in the IOGU, which is dated between  $2002 \pm 14$  Ma and  $1983 \pm 15$  Ma (Peucat et al., 1996). Conversely to the IOGU, the IGU suffered a Pan-African metamorphic overprint (Boullier and Barbey, 1988; Boullier, 1991) and was cut by a widespread calc-alkaline magmatism (Boullier, 1982; Bertrand et al., 1984; Leterrier and Bertrand, 1986; Liégeois et al., 1987). The sample collected in the IGU (sample 04-40) is from an allanite-rich graphitic horizon, 1–2 m thick, interlayered with cordierite-sillimanite kinzigite and khondalite. The sample contains coarse-grained allanite crystals (75%), altered plagioclase (5%), epidote, apatite and rare quartz (Fig. 4C). A narrow slice of granulitic basement also crops out northwest of the IGU (In Bezzeg), and exposes diversely retrogressed metasedimentary granulites alternating with spinel- and garnet-pyroxenites. The granulitic units in this area are lithologically comparable to those cropping out in the IGU, and include kinzigites, garnetites and pyrigarnites. Pre-metamorphic mafic dykes affected by greenschist to amphibolite facies overprint and abundant Pan-African plutons (ca. 20%) were emplaced in the IGU, among which calc-alkaline gabbros and tonalite/monzodiorite/granodiorite masses (Boullier, 1982; Bertrand et al., 1984; Leterrier and Bertrand, 1986).

Basement rocks from the In Bezzeg unit are also cross cut by numerous plutons and dykes considered as Pan-African in age (Boullier, 1982). The sample collected at In Bezzeg (sample IC218A) is a garnetite composed of coarse-grained garnet (50%), quartz, altered plagioclase, tremolite pseudomorphs after pyroxene, spinel and ilmenite. Minute secondary biotite occurs in the matrix and around garnet as reaction rim.

The southern extremity or “tail” of the IOGU exposes in Mali two narrow belts of protomylonitic to mylonitic granulites recognized through the preservation of mesoperthite clasts (Boullier et al., 1978), whereas cross-cutting mafic dykes were converted into mylonitic amphibolite. These granulitic ribbons have mylonitic contacts (Fig. 4D) with the gneissic assemblages and the mylonitic foliation developed under amphibolite facies conditions (Champenois et al., 1987).

## 2.3. Eastern Iforas domain (Tamaradant-Tin Essako-Tin Zawatene domains)

In the course of this study, two samples were collected east of the IGU, close to the Adrar fault, which represents the southern tip of a 600 km long fault (Caby, 2003). The goal was to compare the ages of these units with those known in the Kidal terrane. Three dissimilar domains are exposed to the east of the IGU. From the west to the east, these are the Tamaradant domain truncated by the Adrar fault, the Tin Zawatene domain, and the Tin Essako domain. The three domains, studied by Davison (1980), include monocyclic metasedimentary sequences and several metaigneous complexes, all cut by syn- and late-Pan-African granitoids. The Tin Essako domain is constituted by a granitic basement, that delimits to the west the Tamaradant domain. The latter is composed of quartzite intruded by sub-alkali felsic magmatic rocks that have been related to a late Paleoproterozoic rifting event (Caby and Andréopoulos-Renaud, 1983). Metagabbros, anorthosites, troctolites, pyroxenites and meta-peridotites, tentatively associated to this event, occur in this domain (Fig. 4E). These formations are unconformably overlain by Neoproterozoic greywackes, comparable to the Tafeliant

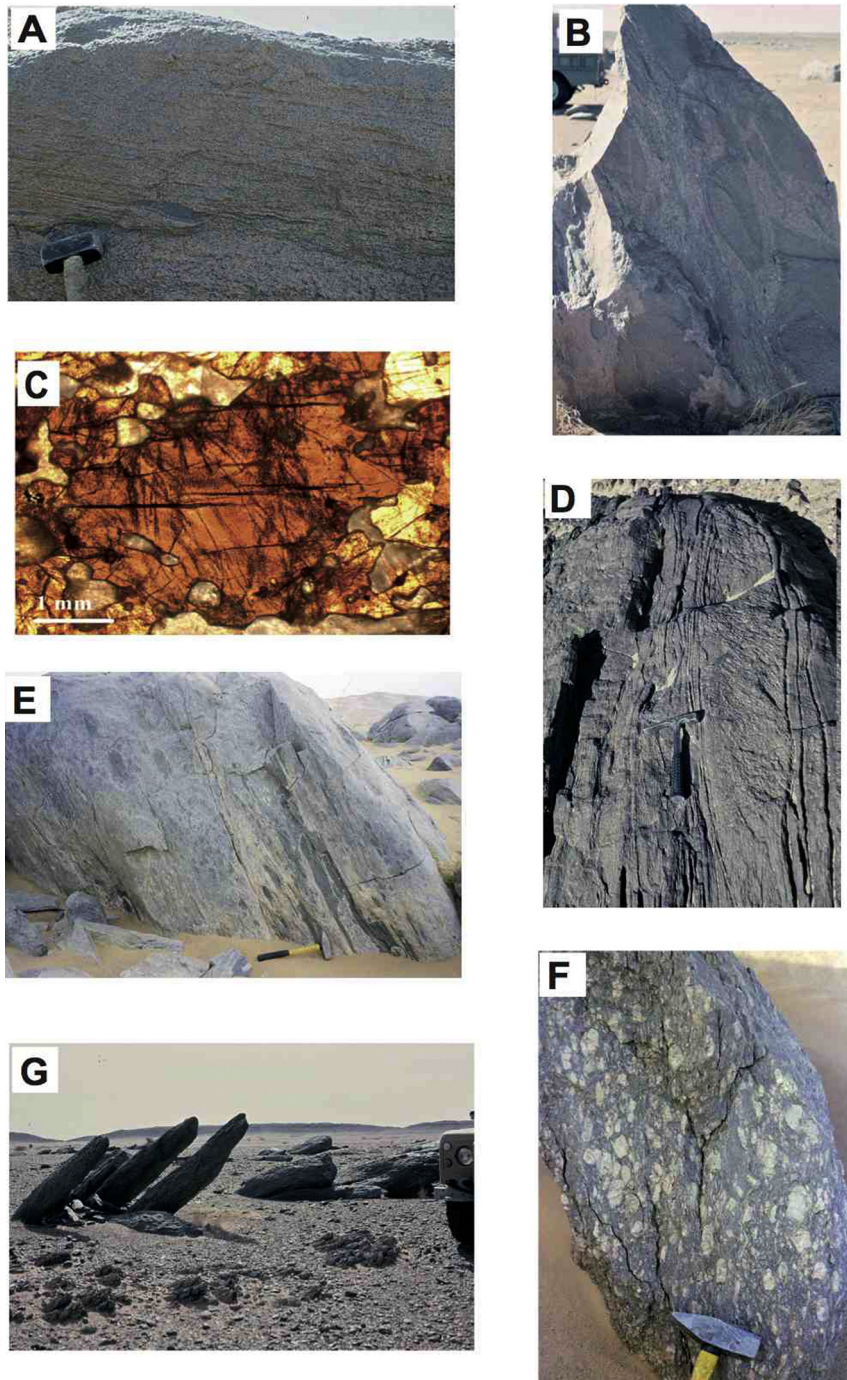


**Fig. 4.** (A) Granodiorite with flow structure and mafic enclaves, southern part of the batholith southeast of Kidal. (B) Mixing/mingling between mafic diorite and granodiorite with flow structure, central part of the batholith. (C) Coarse allanite from sample 04.40. (D) Foliated meta-anorthosite from the Tamaradant domain containing stretched mafic enclaves (04-11). (E) Greenschist facies mylonitic granulite. (F) Tin Essako orthogneiss (sample 04.14). (G) Strongly foliated and lineated metadiorite from the eastern margin of the Tamaradant domain (sample 03.12).

Group. The first studied sample, the Tin Essako orthogneiss 04-14 (Fig. 4F), is an augen gneiss containing quartz, perthitic K-feldspar phenocrysts, albitised plagioclase and partly preserved magmatic biotite. The sample displays a foliation defined by K-feldspar and quartz alignments and outlined by polycrystalline ribbons of secondary brown biotite and white mica. The metamorphic paragenesis, defined by brown biotite, white mica, albite, quartz, epidote and carbonate, indicates a greenschist facies metamorphic overprint. The second sample is a metadiorite (03-12) collected in the Tamaradant domain (Fig. 4G). It contains plagioclase, amphibole

phenocrysts and secondary brown biotite developed at the expense of primary magmatic biotite. The metamorphic matrix derived from a microcrystalline magmatic mesostase is completely recrystallized in a mosaic of quartz, plagioclase, brown biotite and epidote. The metamorphic overprint observed in both rocks suggests that they were emplaced and subsequently deformed before the upper greenschist-lower amphibolite facies regional metamorphism. In addition, two samples (meta-anorthosite 04-10, and meta-gabbro 04-11) were collected in the Tamaradant domain for trace elements and Sr-Nd isotope analyses. Sample 04-11 is a layered meta-gabbro

that contains clinopyroxene, plagioclase and amphibole. Sample 04-10 comes from a decimetric band of meta-anorthosite commonly observed in the meta-gabbro 04-11.

### 3. Analytical methods

Zircons from the studied samples were extracted following standard techniques (e.g. Bosch et al., 1996). In order to select the best quality grains, zircons were subsequently hand-picked in alcohol under binocular examination, and mounted in epoxy plugs with chips of the G91500 zircon standard (Wiedenbeck et al., 1995). U-Th-Pb analyses were performed using a Compex 102 Lambda-Physik excimer laser operating at 4 Hz with an energy density of 12 J/cm<sup>2</sup> and a spot diameter of 26 µm. Samples were ablated under He and the ablation products were transported to the torch of a VG Plasmaquad II quadrupole ICP-MS by addition of a small amount of Ar gas (for details see Dhuime et al., 2007 and Bruguier et al., 2009). Signals were acquired in the peak-jumping mode. Pb/Pb ratios in the unknowns were mass-bias corrected using a power law whose parameters were determined by repetitive analysis of the reference material measured during the whole analytical session. This mass bias factor was used to correct the <sup>207</sup>Pb/<sup>206</sup>Pb ratios measured on the unknowns and its associated error was added in quadrature to the <sup>207</sup>Pb/<sup>206</sup>Pb ratios measured on each unknown following the procedure described in Horstwood et al. (2003). Inter-element fractionation for U and Pb is more sensitive to analytical conditions and the Pb/U ratios of each batch of five unknowns were calibrated against the bias factor calculated using four standards bracketing the five unknowns. The mean Pb/U ratio of the four measured standards was used to calculate the inter-element fractionation and its error was then added in quadrature to the individual error measured on each <sup>206</sup>Pb/<sup>238</sup>U unknown. Accurate common lead correction is difficult to achieve, mainly because of the isobaric interference of <sup>204</sup>Hg on <sup>204</sup>Pb. The contribution of <sup>204</sup>Hg on <sup>204</sup>Pb was estimated by measuring the <sup>202</sup>Hg and assuming a <sup>204</sup>Hg/<sup>202</sup>Hg natural isotopic composition of 0.2298. This allows monitoring the common lead content of the analyzed grain, but corrections are often inaccurate. Analyses yielding <sup>204</sup>Pb were thus rejected and Table 1 reports only analyses for which no <sup>204</sup>Pb was detected. Quoted ratios correspond to measured ratios corrected for background and mass discrimination (+ elemental fractionation for the <sup>206</sup>Pb/<sup>238</sup>U ratios). All ages have been calculated using the U and Th decay constants recommended by Steiger and Jäger (1977). Analytical data were plotted and ages were calculated using the IsoplotEx program (Ludwig, 2000). Individual analyses in Table 1 and in concordia plots are  $\pm 1\sigma$  errors and uncertainties in ages are quoted in the text at the  $2\sigma$  level. Analyses are considered concordant to sub-concordant when their discordance degree is less than  $\pm 5\%$ .

Rock samples were crushed then powdered in an agate mill for whole rock (WR) analyses. Major elements (Table 2) were analyzed by ICP-AES at SARM (Nancy). Whole-rock trace element concentrations were determined using a high resolution inductively plasma mass spectrometer (ICP-MS) Thermo Element II at the technical platform AEET (Montpellier). For the Sr-Nd isotope analyses, whole-rock powders were leached with 6 N HCl during one hour and a half at 95 °C and then rinsed three times with ultrapure water and centrifugated during 20 min for each step. After this leaching treatment, samples were dissolved during 72 h on a hot plate at 140 °C with a mixture of concentrated pure 48% HF and 13 N HNO<sub>3</sub> (1:1) and small amounts of HClO<sub>4</sub>. After evaporation to dryness, 2 ml of HNO<sub>3</sub> was added to the residue and kept at about 110 °C for 48 h before evaporation to dryness. The total blanks for Sr, and Nd were respectively lower than 20 pg and 8 pg and were considered negligible for the present analyses. The Sr isotopic ratios were

measured by thermal ionization mass spectrometry using a Triton Finnigan Mat spectrometer from the Labogis of the Nîmes University. Nd isotopic ratios were measured using the Nu-Instruments 500-HR MC-ICP-MS from the Ecole Normale Supérieure (ENS) of Lyon. To assess the reproducibility and accuracy of the isotopic ratios, standards were repeatedly run during this study. The standard average values were  $0.710245 \pm 0.09$  ( $2\sigma$ ) ( $n=6$ ) for NBS987 Sr standard and  $0.5119630 \pm 6$  ( $2\sigma$ ) ( $n=8$ ) for the AMES-Rennes Nd standard (Chauvel and Blachert-Toft, 2001). Following Stern (2002), Nd T<sub>DM</sub> model ages were calculated only for samples with low <sup>147</sup>Sm/<sup>144</sup>Nd, considering that samples with <sup>147</sup>Sm/<sup>144</sup>Nd > 0.165 may give unreliable model ages.

### 4. Results

For the purpose of clarity, geochronological results of the studied samples are presented following a broad west-east transect, which corresponds to the structural architecture of the Adrar des Iforas (see Fig. 2). This corresponds to the Tilemsi/Adjel'Hoc terrane (west of the Tessalit-Anéfif shear zone), to the Kidal terrane, to the Iforas granulitic unit (IGU) and In Bezzeg inlier, and to the Tamaradant-Tin Essako-Tin Zawatene domain (TTT), east of the IGU. Major, trace elements and Sr-Nd isotopic results of the samples collected in the Kidal terrane and TTT domain are presented after the U-Pb results.

#### 4.1. Tilemsi/Adjel'Hoc terrane

##### 4.1.1. Synkinematic diorite 03-97

Zircon grains from the diorite are translucent colorless, euhedral to subhedral with oscillatory zoning (Fig. 5a). The magmatic characteristics of the zircon grains (euohedral shapes and oscillatory zoning) and their high Th/U ratios (>0.4 and up to 1.34) are consistent with their crystallization from the dioritic magma. Twenty-six analyses were performed on twenty grains displaying oscillatory zoning. The main batch of analyses (24 out of 26) constitutes a coherent population (Fig. 6a) with a <sup>206</sup>Pb/<sup>238</sup>U age of  $643 \pm 4$  Ma (MSWD = 1.1). Two analyses of euhedrally zoned grains (#25 and #26) provide slightly older ages of  $722 \pm 20$  Ma and  $748 \pm 46$  Ma ( $2\sigma$ ), attributed to an inherited component.

##### 4.1.2. Diatexite 03-94A

The sample contains a uniform population of honey-colored translucent zircon grains with euhedral to subhedral shapes (Fig. 5b). Analyzed grains yield low Th/U ratios classically attributed to metamorphic zircons (e.g. Williams and Claesson, 1987). The euhedral shape of the grains and their oscillatory zoning however indicate crystallization from a melt, and we therefore interpret these zircons as crystallized during partial melting of the protolith of the diatexite. The low Th/U ratios indicate small degree of partial melting where monazite is a residual phase (Stepanov et al., 2012). Euhedrally zoned grains yield concordant analyses (Fig. 6b) plotting between  $592 \pm 10$  Ma and  $653 \pm 90$  Ma ( $2\sigma$ ). The youngest analysis was considered as an outlier during calculation and may be related to younger disturbances. The remaining analyses define an age of  $626 \pm 8$  Ma (MSWD = 1.9) that we relate to crystallization of the zircon in the leucocratic part of the diatexite. Two analyses performed on the central part of grains #20 and #21 provide ages of  $729 \pm 22$  Ma and  $769 \pm 44$  Ma ( $2\sigma$ ), which may represent the age of the protolith that underwent migmatitisation.

##### 4.1.3. Sub-alkali orthogneiss 03-82

Zircon grains are translucent colorless and subhedral with oscillatory zoned domains (Fig. 5c). Twenty-four analyses were performed on twenty grains and they plot concordantly at about 700 Ma (Fig. 6c). The <sup>206</sup>Pb/<sup>238</sup>U weighted mean age is  $716 \pm 6$  Ma

**Table 1**

Laser ablation U–Pb analyses for rocks of the Adrar des Iforas.

| Sample  | Pb* (ppm) | U (ppm) | Th (ppm) | Th/U | 208Pb/206Pb | 207Pb/206Pb | ± (1σ) | 207Pb/235U | ± (1σ) | 206Pb/238U | ± (1σ) | Rho  | Apparent ages (Ma) |           |             |           | Disc% |
|---|-----------|---------|----------|------|-------------|-------------|--------|------------|--------|------------|--------|------|--------------------|-----------|-------------|-----------|-------|
|   |           |         |          |      |             |             |        |            |        |            |        |      | 206Pb/238U         | ± (1(1σ)) | 207Pb/206Pb | ± (1(1σ)) |       |
| <b>Synkinematic diorite 03-97 (Adjel'Hoc)</b> |           |         |          |      |             |             |        |            |        |            |        |      |                    |           |             |           |       |
| #1*   | 23        | 198     | 233      | 1.18 | 0.30        | 0.0615      | 0.0009 | 0.863      | 0.019  | 0.102      | 0.002  | 0.73 | 625                | 9         | 658         | 31        | 6.0   |
| #2*   | 14        | 132     | 131      | 0.99 | 0.24        | 0.0612      | 0.0004 | 0.853      | 0.040  | 0.101      | 0.005  | 0.99 | 621                | 27        | 648         | 13        | 4.2   |
| #3*   | 14        | 128     | 54       | 0.42 | 0.14        | 0.0618      | 0.0008 | 0.869      | 0.015  | 0.102      | 0.001  | 0.66 | 627                | 7         | 666         | 27        | 5.9   |
| #4*   | 10        | 89      | 69       | 0.77 | 0.21        | 0.0620      | 0.0004 | 0.876      | 0.050  | 0.102      | 0.006  | 0.99 | 629                | 34        | 673         | 14        | 6.6   |
| #5*   | 12        | 100     | 120      | 1.20 | 0.32        | 0.0650      | 0.0022 | 0.920      | 0.045  | 0.103      | 0.004  | 0.72 | 630                | 21        | 776         | 70        | 18.8  |
| #6*   | 16        | 144     | 86       | 0.60 | 0.19        | 0.0618      | 0.0014 | 0.879      | 0.023  | 0.103      | 0.001  | 0.49 | 633                | 8         | 667         | 48        | 5.1   |
| #7*   | 8         | 74      | 52       | 0.70 | 0.22        | 0.0629      | 0.0012 | 0.898      | 0.025  | 0.104      | 0.002  | 0.74 | 635                | 12        | 703         | 40        | 9.7   |
| #8*   | 6         | 55      | 31       | 0.55 | 0.19        | 0.0614      | 0.0017 | 0.881      | 0.069  | 0.104      | 0.008  | 0.93 | 638                | 44        | 653         | 58        | 2.2   |
| #9*   | 14        | 130     | 82       | 0.63 | 0.20        | 0.0601      | 0.0008 | 0.863      | 0.017  | 0.104      | 0.002  | 0.75 | 639                | 9         | 609         | 27        | -4.9  |
| #10*  | 17        | 149     | 157      | 1.05 | 0.24        | 0.0623      | 0.0016 | 0.896      | 0.042  | 0.104      | 0.004  | 0.84 | 639                | 24        | 685         | 54        | 6.6   |
| #11*  | 11        | 94      | 50       | 0.53 | 0.19        | 0.0631      | 0.0009 | 0.908      | 0.042  | 0.104      | 0.005  | 0.95 | 640                | 27        | 712         | 31        | 10.1  |
| #12*  | 14        | 116     | 101      | 0.88 | 0.24        | 0.0658      | 0.0011 | 0.949      | 0.019  | 0.105      | 0.001  | 0.59 | 641                | 7         | 800         | 34        | 19.8  |
| #13*  | 19        | 139     | 187      | 1.34 | 0.40        | 0.0648      | 0.0010 | 0.946      | 0.017  | 0.106      | 0.001  | 0.50 | 649                | 6         | 767         | 33        | 43.1  |
| #14*  | 10        | 84      | 36       | 0.43 | 0.22        | 0.0606      | 0.0001 | 0.888      | 0.028  | 0.106      | 0.003  | 1.00 | 651                | 19        | 624         | 4         | -4.3  |
| #15*  | 11        | 93      | 81       | 0.88 | 0.22        | 0.0606      | 0.0004 | 0.889      | 0.020  | 0.106      | 0.002  | 0.95 | 652                | 13        | 625         | 15        | -4.2  |
| #16*  | 11        | 89      | 62       | 0.69 | 0.22        | 0.0598      | 0.0005 | 0.877      | 0.011  | 0.106      | 0.001  | 0.69 | 652                | 5         | 595         | 19        | -9.7  |
| #17*  | 17        | 153     | 134      | 0.88 | 0.25        | 0.0605      | 0.0011 | 0.888      | 0.061  | 0.106      | 0.007  | 0.97 | 652                | 41        | 621         | 38        | -4.9  |
| #18*  | 13        | 106     | 85       | 0.81 | 0.28        | 0.0605      | 0.0012 | 0.891      | 0.044  | 0.107      | 0.005  | 0.92 | 654                | 28        | 621         | 42        | -5.4  |
| #19*  | 11        | 90      | 104      | 1.16 | 0.30        | 0.0632      | 0.0021 | 0.933      | 0.038  | 0.107      | 0.003  | 0.60 | 656                | 15        | 715         | 69        | 8.3   |
| #20*  | 14        | 119     | 57       | 0.48 | 0.21        | 0.0613      | 0.0007 | 0.909      | 0.015  | 0.108      | 0.001  | 0.73 | 658                | 8         | 649         | 25        | -1.5  |
| #21*  | 15        | 125     | 104      | 0.83 | 0.25        | 0.0629      | 0.0023 | 0.934      | 0.075  | 0.108      | 0.008  | 0.89 | 659                | 44        | 706         | 77        | 6.6   |
| #22*  | 15        | 114     | 98       | 0.86 | 0.29        | 0.0627      | 0.0008 | 0.930      | 0.042  | 0.108      | 0.005  | 0.96 | 659                | 27        | 697         | 27        | 5.4   |
| #23*  | 10        | 80      | 59       | 0.74 | 0.22        | 0.0596      | 0.0015 | 0.896      | 0.039  | 0.109      | 0.004  | 0.82 | 667                | 23        | 588         | 53        | -13.5 |
| #24*  | 10        | 94      | 89       | 0.95 | 0.22        | 0.0610      | 0.0019 | 0.920      | 0.099  | 0.109      | 0.011  | 0.96 | 669                | 65        | 640         | 65        | -4.5  |
| #25   | 14        | 106     | 85       | 0.80 | 0.24        | 0.0617      | 0.0018 | 1.008      | 0.033  | 0.119      | 0.002  | 0.46 | 722                | 10        | 664         | 61        | -8.8  |
| #26   | 6         | 44      | 29       | 0.67 | 0.26        | 0.0595      | 0.0012 | 1.010      | 0.039  | 0.123      | 0.004  | 0.84 | 748                | 23        | 586         | 44        | -27.7 |
| <b>Diatexite 03-94A (Adjel'Hoc)</b>           |           |         |          |      |             |             |        |            |        |            |        |      |                    |           |             |           |       |
| #1  | 25        | 286     | 1        | 0.01 | 0.00        | 0.0589      | 0.0019 | 0.781      | 0.026  | 0.096      | 0.001  | 0.29 | 592                | 5         | 564         | 69        | -5.0  |
| #2*   | 12        | 129     | 1        | 0.00 | 0.02        | 0.0610      | 0.0011 | 0.823      | 0.023  | 0.098      | 0.002  | 0.74 | 602                | 12        | 638         | 40        | 5.7   |
| #3*   | 25        | 267     | 2        | 0.01 | 0.01        | 0.0610      | 0.0017 | 0.841      | 0.024  | 0.100      | 0.001  | 0.25 | 614                | 4         | 639         | 60        | 3.8   |
| #4*   | 9         | 94      | 1        | 0.01 | 0.00        | 0.0576      | 0.0003 | 0.794      | 0.015  | 0.100      | 0.002  | 0.97 | 615                | 11        | 513         | 10        | -19.9 |
| #5*   | 22        | 225     | 3        | 0.01 | 0.01        | 0.0597      | 0.0018 | 0.827      | 0.028  | 0.100      | 0.002  | 0.45 | 617                | 9         | 593         | 65        | -4.1  |
| #6*   | 26        | 294     | 2        | 0.01 | 0.01        | 0.0609      | 0.0029 | 0.846      | 0.071  | 0.101      | 0.007  | 0.82 | 618                | 41        | 637         | 102       | 3.0   |
| #7*   | 28        | 300     | 1        | 0.00 | 0.06        | 0.0630      | 0.0015 | 0.886      | 0.093  | 0.102      | 0.010  | 0.98 | 626                | 61        | 708         | 49        | 11.5  |
| #8*   | 35        | 360     | 2        | 0.01 | 0.00        | 0.0601      | 0.0008 | 0.846      | 0.030  | 0.102      | 0.003  | 0.92 | 626                | 20        | 607         | 29        | -3.1  |
| #9*   | 7         | 74      | 0        | 0.01 | 0.01        | 0.0637      | 0.0017 | 0.902      | 0.045  | 0.103      | 0.004  | 0.78 | 631                | 23        | 730         | 52        | 29.0  |
| #10*  | 33        | 377     | 2        | 0.01 | 0.01        | 0.0609      | 0.0019 | 0.864      | 0.076  | 0.103      | 0.008  | 0.93 | 631                | 49        | 636         | 68        | 0.7   |
| #11*  | 9         | 95      | 0        | 0.00 | 0.00        | 0.0598      | 0.0012 | 0.853      | 0.022  | 0.103      | 0.002  | 0.65 | 634                | 10        | 597         | 43        | -6.4  |
| #12*  | 10        | 105     | 1        | 0.00 | 0.01        | 0.0624      | 0.0015 | 0.896      | 0.031  | 0.104      | 0.003  | 0.71 | 639                | 15        | 686         | 53        | 6.9   |
| #13*  | 34        | 348     | 1        | 0.00 | 0.01        | 0.0602      | 0.0008 | 0.872      | 0.018  | 0.105      | 0.002  | 0.74 | 643                | 9         | 612         | 30        | -5.2  |
| #14*  | 8         | 77      | 0        | 0.00 | 0.04        | 0.0610      | 0.0012 | 0.884      | 0.024  | 0.105      | 0.002  | 0.71 | 644                | 12        | 639         | 41        | -0.9  |
| #15*  | 56        | 582     | 7        | 0.01 | 0.00        | 0.0598      | 0.0009 | 0.868      | 0.017  | 0.105      | 0.001  | 0.64 | 645                | 8         | 596         | 33        | -8.2  |
| #16*  | 22        | 237     | 2        | 0.01 | 0.01        | 0.0583      | 0.0018 | 0.850      | 0.037  | 0.106      | 0.003  | 0.71 | 648                | 19        | 543         | 66        | -19.3 |
| #17*  | 21        | 212     | 1        | 0.01 | 0.01        | 0.0605      | 0.0015 | 0.882      | 0.031  | 0.106      | 0.003  | 0.71 | 648                | 15        | 620         | 53        | -4.5  |
| #18*  | 24        | 233     | 4        | 0.02 | 0.03        | 0.0623      | 0.0032 | 0.909      | 0.057  | 0.106      | 0.004  | 0.56 | 648                | 21        | 684         | 111       | 5.2   |
| #19*  | 10        | 101     | 2        | 0.02 | 0.02        | 0.0611      | 0.0004 | 0.897      | 0.065  | 0.107      | 0.008  | 1.00 | 653                | 45        | 642         | 14        | -1.6  |
| #20   | 12        | 107     | 0        | 0.00 | 0.02        | 0.0620      | 0.0006 | 1.022      | 0.019  | 0.120      | 0.002  | 0.83 | 729                | 11        | 672         | 22        | -8.4  |
| #21   | 12        | 62      | 20       | 0.32 | 0.28        | 0.0657      | 0.0037 | 1.148      | 0.074  | 0.127      | 0.004  | 0.48 | 769                | 22        | 797         | 118       | 3.5   |

Table 1 (Continued)

| Sample  | Pb <sup>+</sup> (ppm) | U (ppm) | Th (ppm) | Th/U | 208Pb/206Pb | 207Pb/206Pb | ± (1σ) | 207Pb/235U | ± (1σ) | 206Pb/238U | ± (1σ) | Rho  | Apparent ages (Ma) |           |             |           | Disc% |
|---|-----------------------|---------|----------|------|-------------|-------------|--------|------------|--------|------------|--------|------|--------------------|-----------|-------------|-----------|-------|
|   |                       |         |          |      |             |             |        |            |        |            |        |      | 206Pb/238U         | ± (1(1σ)) | 207Pb/206Pb | ± (1(1σ)) |       |
| <b>Sub-alkali orthogneiss 03-82 (Adjel'Hoc)</b> |                       |         |          |      |             |             |        |            |        |            |        |      |                    |           |             |           |       |
| #1 <sup>*</sup>                                 | 21                    | 173     | 88       | 0.51 | 0.15        | 0.0648      | 0.0005 | 1.056      | 0.013  | 0.118      | 0.001  | 0.76 | 720                | 6         | 768         | 17        | 6.3   |
| #2 <sup>*</sup>                                 | 21                    | 159     | 101      | 0.64 | 0.19        | 0.0632      | 0.0006 | 1.020      | 0.019  | 0.117      | 0.002  | 0.86 | 714                | 11        | 715         | 20        | 0.2   |
| #3 <sup>*</sup>                                 | 21                    | 165     | 92       | 0.55 | 0.17        | 0.0632      | 0.0004 | 1.008      | 0.036  | 0.116      | 0.004  | 0.98 | 705                | 23        | 715         | 15        | 1.4   |
| #4 <sup>*</sup>                                 | 24                    | 199     | 113      | 0.57 | 0.17        | 0.0644      | 0.0011 | 1.003      | 0.025  | 0.113      | 0.002  | 0.72 | 690                | 12        | 754         | 37        | 8.4   |
| #5 <sup>*</sup>                                 | 52                    | 373     | 201      | 0.54 | 0.17        | 0.0635      | 0.0003 | 1.104      | 0.026  | 0.126      | 0.003  | 0.99 | 766                | 17        | 725         | 8         | -5.7  |
| #6 <sup>*</sup>                                 | 17                    | 141     | 70       | 0.49 | 0.16        | 0.0627      | 0.0006 | 1.009      | 0.021  | 0.117      | 0.002  | 0.90 | 712                | 13        | 699         | 19        | -1.9  |
| #7 <sup>*</sup>                                 | 25                    | 202     | 102      | 0.50 | 0.16        | 0.0642      | 0.0004 | 1.048      | 0.024  | 0.118      | 0.003  | 0.97 | 721                | 15        | 749         | 12        | 3.8   |
| #8 <sup>*</sup>                                 | 21                    | 170     | 97       | 0.57 | 0.17        | 0.0639      | 0.0007 | 1.026      | 0.017  | 0.116      | 0.001  | 0.74 | 710                | 8         | 740         | 23        | 4.0   |
| #9 <sup>*</sup>                                 | 33                    | 256     | 181      | 0.71 | 0.21        | 0.0640      | 0.0004 | 1.052      | 0.021  | 0.119      | 0.002  | 0.95 | 727                | 13        | 740         | 13        | 1.8   |
| #10 <sup>*</sup>                                | 23                    | 193     | 91       | 0.47 | 0.15        | 0.0637      | 0.0006 | 1.026      | 0.019  | 0.117      | 0.002  | 0.87 | 712                | 11        | 731         | 19        | 2.6   |
| #11 <sup>*</sup>                                | 27                    | 212     | 123      | 0.58 | 0.20        | 0.0636      | 0.0004 | 1.038      | 0.023  | 0.118      | 0.002  | 0.95 | 721                | 14        | 729         | 15        | 1.1   |
| #12 <sup>*</sup>                                | 30                    | 245     | 149      | 0.61 | 0.20        | 0.0642      | 0.0010 | 1.029      | 0.043  | 0.116      | 0.005  | 0.93 | 709                | 26        | 748         | 34        | 5.2   |
| #13 <sup>*</sup>                                | 21                    | 181     | 98       | 0.54 | 0.18        | 0.0633      | 0.0003 | 0.996      | 0.033  | 0.114      | 0.004  | 0.99 | 697                | 22        | 719         | 9         | 3.1   |
| #14 <sup>*</sup>                                | 18                    | 144     | 74       | 0.51 | 0.16        | 0.0629      | 0.0007 | 1.049      | 0.015  | 0.121      | 0.001  | 0.69 | 735                | 7         | 706         | 23        | -4.2  |
| #15 <sup>*</sup>                                | 18                    | 142     | 84       | 0.59 | 0.17        | 0.0615      | 0.0009 | 0.981      | 0.019  | 0.116      | 0.001  | 0.65 | 706                | 8         | 657         | 31        | -7.4  |
| #16 <sup>*</sup>                                | 21                    | 151     | 73       | 0.48 | 0.17        | 0.0651      | 0.0006 | 1.146      | 0.026  | 0.128      | 0.003  | 0.92 | 774                | 15        | 779         | 19        | 0.6   |
| #17 <sup>*</sup>                                | 27                    | 221     | 132      | 0.60 | 0.18        | 0.0636      | 0.0009 | 0.994      | 0.022  | 0.113      | 0.002  | 0.79 | 693                | 12        | 727         | 29        | 4.7   |
| #18 <sup>*</sup>                                | 21                    | 157     | 104      | 0.66 | 0.19        | 0.0629      | 0.0007 | 1.051      | 0.022  | 0.121      | 0.002  | 0.85 | 737                | 12        | 706         | 23        | -4.4  |
| #19 <sup>*</sup>                                | 19                    | 153     | 75       | 0.49 | 0.16        | 0.0626      | 0.0003 | 1.020      | 0.021  | 0.118      | 0.002  | 0.97 | 720                | 14        | 693         | 11        | -3.9  |
| #20 <sup>*</sup>                                | 14                    | 113     | 65       | 0.57 | 0.17        | 0.0638      | 0.0012 | 1.000      | 0.028  | 0.114      | 0.002  | 0.73 | 694                | 13        | 736         | 41        | 5.7   |
| #21 <sup>*</sup>                                | 28                    | 230     | 124      | 0.54 | 0.16        | 0.0630      | 0.0007 | 1.029      | 0.022  | 0.118      | 0.002  | 0.85 | 721                | 13        | 710         | 24        | -1.6  |
| #22 <sup>*</sup>                                | 23                    | 195     | 113      | 0.58 | 0.19        | 0.0642      | 0.0009 | 1.014      | 0.029  | 0.115      | 0.003  | 0.87 | 699                | 17        | 749         | 29        | 6.7   |
| #23 <sup>*</sup>                                | 15                    | 121     | 47       | 0.39 | 0.12        | 0.0655      | 0.0006 | 1.080      | 0.028  | 0.119      | 0.003  | 0.94 | 728                | 17        | 792         | 18        | 8.1   |
| #24 <sup>*</sup>                                | 23                    | 187     | 104      | 0.56 | 0.17        | 0.0645      | 0.0006 | 1.043      | 0.022  | 0.117      | 0.002  | 0.91 | 715                | 13        | 759         | 18        | 5.8   |
| #25 <sup>*</sup>                                | 23                    | 189     | 105      | 0.56 | 0.17        | 0.0634      | 0.0002 | 1.031      | 0.032  | 0.118      | 0.004  | 1.00 | 718                | 21        | 722         | 6         | 0.5   |
| #26 <sup>*</sup>                                | 14                    | 115     | 59       | 0.51 | 0.15        | 0.0644      | 0.0005 | 1.076      | 0.030  | 0.121      | 0.003  | 0.96 | 737                | 19        | 756         | 16        | 2.4   |
| <b>Syenitic gneiss IC622 (Kidal)</b>            |                       |         |          |      |             |             |        |            |        |            |        |      |                    |           |             |           |       |
| #1 <sup>*</sup>                                 | 116                   | 305     | 181      | 0.59 | 0.17        | 0.1208      | 0.0004 | 5.628      | 0.070  | 0.338      | 0.004  | 0.97 | 1876               | 20        | 1969        | 5         | 4.7   |
| #2 <sup>*</sup>                                 | 46                    | 79      | 201      | 2.55 | 0.73        | 0.1201      | 0.0005 | 5.965      | 0.170  | 0.360      | 0.010  | 0.99 | 1983               | 48        | 1958        | 8         | -1.3  |
| #3 <sup>*</sup>                                 | 48                    | 125     | 37       | 0.30 | 0.12        | 0.1210      | 0.0012 | 6.081      | 0.282  | 0.365      | 0.016  | 0.97 | 2004               | 77        | 1971        | 18        | -1.7  |
| #4 <sup>*</sup>                                 | 178                   | 467     | 260      | 0.56 | 0.25        | 0.1218      | 0.0016 | 5.353      | 0.198  | 0.319      | 0.011  | 0.93 | 1784               | 53        | 1983        | 24        | 10.0  |
| #5 <sup>*</sup>                                 | 50                    | 89      | 99       | 1.11 | 0.32        | 0.1510      | 0.0005 | 9.100      | 0.115  | 0.437      | 0.005  | 0.96 | 2338               | 24        | 2357        | 6         | 0.8   |
| #7 <sup>*</sup>                                 | 67                    | 117     | 95       | 0.81 | 0.25        | 0.1525      | 0.0012 | 9.624      | 0.356  | 0.458      | 0.017  | 0.98 | 2429               | 73        | 2374        | 13        | -2.3  |
| #8 <sup>*</sup>                                 | 39                    | 89      | 56       | 0.63 | 0.17        | 0.1311      | 0.0031 | 7.125      | 0.191  | 0.394      | 0.005  | 0.46 | 2141               | 22        | 2113        | 42        | -1.3  |
| #9 <sup>*</sup>                                 | 48                    | 82      | 83       | 1.00 | 0.24        | 0.1451      | 0.0013 | 9.269      | 0.465  | 0.463      | 0.023  | 0.98 | 2454               | 100       | 2289        | 15        | -7.2  |
| #10 <sup>*</sup>                                | 43                    | 81      | 64       | 0.79 | 0.20        | 0.1467      | 0.0025 | 8.905      | 0.285  | 0.440      | 0.012  | 0.85 | 2351               | 53        | 2308        | 29        | -1.9  |
| #11 <sup>*</sup>                                | 155                   | 266     | 279      | 1.05 | 0.28        | 0.1567      | 0.0018 | 10.114     | 0.408  | 0.468      | 0.018  | 0.96 | 2475               | 79        | 2421        | 20        | -2.2  |
| #12 <sup>*</sup>                                | 45                    | 73      | 67       | 0.93 | 0.27        | 0.1621      | 0.0009 | 11.157     | 0.272  | 0.499      | 0.012  | 0.97 | 2611               | 51        | 2477        | 10        | -5.4  |
| #13 <sup>*</sup>                                | 70                    | 125     | 100      | 0.80 | 0.23        | 0.1558      | 0.0027 | 9.608      | 0.488  | 0.447      | 0.021  | 0.94 | 2384               | 94        | 2410        | 29        | 1.1   |
| #14 <sup>*</sup>                                | 68                    | 147     | 118      | 0.80 | 0.22        | 0.1451      | 0.0011 | 7.780      | 0.166  | 0.389      | 0.008  | 0.93 | 2117               | 36        | 2289        | 13        | 7.5   |
| #15 <sup>*</sup>                                | 141                   | 253     | 220      | 0.87 | 0.24        | 0.1554      | 0.0012 | 9.831      | 0.216  | 0.459      | 0.009  | 0.94 | 2435               | 42        | 2406        | 13        | -1.2  |
| #16 <sup>*</sup>                                | 37                    | 64      | 75       | 1.18 | 0.33        | 0.1421      | 0.0006 | 8.950      | 0.171  | 0.457      | 0.009  | 0.97 | 2426               | 38        | 2253        | 7         | -7.7  |
| #17 <sup>*</sup>                                | 48                    | 83      | 89       | 1.08 | 0.33        | 0.1642      | 0.0007 | 10.428     | 0.304  | 0.461      | 0.013  | 0.99 | 2442               | 58        | 2500        | 7         | 2.3   |
| #18 <sup>*</sup>                                | 51                    | 92      | 76       | 0.83 | 0.24        | 0.1625      | 0.0013 | 10.708     | 0.419  | 0.478      | 0.018  | 0.98 | 2519               | 79        | 2481        | 14        | -1.5  |
| #19 <sup>*</sup>                                | 79                    | 137     | 108      | 0.79 | 0.23        | 0.1593      | 0.0007 | 10.558     | 0.328  | 0.481      | 0.015  | 0.99 | 2530               | 64        | 2449        | 7         | -3.3  |
| #20 <sup>*</sup>                                | 52                    | 100     | 83       | 0.83 | 0.24        | 0.1527      | 0.0009 | 9.051      | 0.128  | 0.430      | 0.006  | 0.91 | 2306               | 25        | 2376        | 10        | 3.0   |
| #21 <sup>*</sup>                                | 32                    | 55      | 63       | 1.13 | 0.27        | 0.1602      | 0.0005 | 10.716     | 0.389  | 0.485      | 0.018  | 1.00 | 2550               | 76        | 2458        | 5         | -3.7  |
| #22 <sup>*</sup>                                | 76                    | 144     | 119      | 0.83 | 0.24        | 0.1561      | 0.0006 | 9.449      | 0.549  | 0.439      | 0.025  | 1.00 | 2346               | 113       | 2414        | 7         | 2.8   |
| #23 <sup>*</sup>                                | 49                    | 86      | 83       | 0.96 | 0.27        | 0.1532      | 0.0014 | 9.767      | 0.225  | 0.462      | 0.010  | 0.92 | 2450               | 43        | 2382        | 15        | -2.9  |
| #24 <sup>*</sup>                                | 54                    | 94      | 79       | 0.83 | 0.24        | 0.1587      | 0.0006 | 10.265     | 0.221  | 0.469      | 0.010  | 0.98 | 2480               | 43        | 2441        | 6         | -1.6  |
| #25 <sup>*</sup>                                | 34                    | 57      | 46       | 0.80 | 0.23        | 0.1584      | 0.0007 | 10.137     | 0.586  | 0.464      | 0.027  | 1.00 | 2457               | 117       | 2439        | 8         | -0.7  |
| #26 <sup>*</sup>                                | 75                    | 128     | 103      | 0.81 | 0.23        | 0.1615      | 0.0015 | 10.973     | 0.471  | 0.493      | 0.021  | 0.98 | 2582               | 88        | 2472        | 16        | -4.5  |

Table 1 (Continued)

| Sample                            | Pb <sup>+</sup> (ppm) | U (ppm) | Th (ppm) | Th/U | 208Pb/206Pb | 207Pb/206Pb | ± (1σ) | 207Pb/235U | ± (1σ) | 206Pb/238U | ± (1σ) | Rho  | Apparent ages (Ma) |           |             |           | Disc% |
|-----------------------------------|-----------------------|---------|----------|------|-------------|-------------|--------|------------|--------|------------|--------|------|--------------------|-----------|-------------|-----------|-------|
|                                   |                       |         |          |      |             |             |        |            |        |            |        |      | 206Pb/238U         | ± (1(1σ)) | 207Pb/206Pb | ± (1(1σ)) |       |
| <b>Tonalite N188 (Kidal)</b>      |                       |         |          |      |             |             |        |            |        |            |        |      |                    |           |             |           |       |
| #1 <sup>*</sup>                   | 22                    | 203     | 121      | 0.60 | 0.15        | 0.0601      | 0.0007 | 0.843      | 0.016  | 0.102      | 0.002  | 0.81 | 624                | 9         | 608         | 24        | -2.6  |
| #2 <sup>*</sup>                   | 23                    | 227     | 214      | 0.94 | 0.18        | 0.0591      | 0.0017 | 0.777      | 0.048  | 0.095      | 0.005  | 0.88 | 587                | 31        | 572         | 64        | -2.7  |
| #3 <sup>*</sup>                   | 34                    | 357     | 197      | 0.55 | 0.15        | 0.0591      | 0.0003 | 0.792      | 0.044  | 0.097      | 0.005  | 1.00 | 597                | 31        | 572         | 10        | -4.3  |
| #4 <sup>*</sup>                   | 18                    | 157     | 145      | 0.92 | 0.26        | 0.0615      | 0.0013 | 0.843      | 0.049  | 0.099      | 0.005  | 0.93 | 611                | 31        | 658         | 47        | 7.2   |
| #5 <sup>*</sup>                   | 64                    | 634     | 257      | 0.41 | 0.11        | 0.0605      | 0.0007 | 0.798      | 0.060  | 0.096      | 0.007  | 0.99 | 589                | 42        | 621         | 24        | 5.1   |
| #6 <sup>*</sup>                   | 20                    | 187     | 160      | 0.85 | 0.21        | 0.0623      | 0.0021 | 0.803      | 0.060  | 0.093      | 0.006  | 0.89 | 576                | 37        | 686         | 72        | 16.0  |
| #7 <sup>*</sup>                   | 30                    | 329     | 188      | 0.57 | 0.11        | 0.0608      | 0.0007 | 0.774      | 0.068  | 0.092      | 0.008  | 0.99 | 570                | 47        | 631         | 26        | 9.6   |
| #8 <sup>*</sup>                   | 31                    | 331     | 231      | 0.70 | 0.19        | 0.0594      | 0.0012 | 0.792      | 0.091  | 0.097      | 0.011  | 0.98 | 595                | 64        | 582         | 46        | -2.1  |
| #9 <sup>*</sup>                   | 24                    | 222     | 147      | 0.66 | 0.19        | 0.0593      | 0.0005 | 0.857      | 0.052  | 0.105      | 0.006  | 0.99 | 642                | 36        | 579         | 19        | -10.9 |
| #10 <sup>*</sup>                  | 28                    | 289     | 149      | 0.51 | 0.14        | 0.0620      | 0.0004 | 0.811      | 0.038  | 0.095      | 0.004  | 0.99 | 584                | 26        | 675         | 16        | 13.6  |
| #11 <sup>*</sup>                  | 26                    | 244     | 200      | 0.82 | 0.22        | 0.0638      | 0.0010 | 0.868      | 0.048  | 0.099      | 0.005  | 0.96 | 607                | 31        | 734         | 32        | 17.3  |
| #12 <sup>*</sup>                  | 17                    | 151     | 97       | 0.64 | 0.17        | 0.0634      | 0.0008 | 0.909      | 0.042  | 0.104      | 0.005  | 0.96 | 638                | 27        | 721         | 26        | 11.5  |
| #13 <sup>*</sup>                  | 8                     | 73      | 36       | 0.50 | 0.15        | 0.0627      | 0.0023 | 0.910      | 0.045  | 0.105      | 0.003  | 0.65 | 646                | 19        | 698         | 80        | 7.5   |
| #14 <sup>*</sup>                  | 21                    | 205     | 115      | 0.56 | 0.15        | 0.0607      | 0.0008 | 0.822      | 0.026  | 0.098      | 0.003  | 0.92 | 604                | 16        | 629         | 27        | 4.1   |
| #15 <sup>*</sup>                  | 37                    | 359     | 308      | 0.86 | 0.22        | 0.0609      | 0.0002 | 0.783      | 0.035  | 0.093      | 0.004  | 1.00 | 575                | 24        | 635         | 8         | 9.4   |
| #16 <sup>*</sup>                  | 33                    | 327     | 227      | 0.69 | 0.19        | 0.0599      | 0.0004 | 0.807      | 0.033  | 0.098      | 0.004  | 0.98 | 601                | 23        | 599         | 15        | -0.4  |
| #17 <sup>*</sup>                  | 21                    | 213     | 174      | 0.82 | 0.20        | 0.0615      | 0.0019 | 0.795      | 0.059  | 0.094      | 0.006  | 0.91 | 578                | 37        | 656         | 67        | 11.9  |
| #18 <sup>*</sup>                  | 22                    | 208     | 123      | 0.59 | 0.17        | 0.0598      | 0.0005 | 0.803      | 0.032  | 0.097      | 0.004  | 0.98 | 599                | 22        | 598         | 18        | -0.1  |
| #19 <sup>*</sup>                  | 26                    | 243     | 165      | 0.68 | 0.19        | 0.0616      | 0.0005 | 0.846      | 0.036  | 0.100      | 0.004  | 0.98 | 612                | 24        | 660         | 17        | 7.2   |
| #20 <sup>*</sup>                  | 27                    | 241     | 213      | 0.88 | 0.23        | 0.0615      | 0.0008 | 0.846      | 0.053  | 0.100      | 0.006  | 0.98 | 613                | 36        | 656         | 27        | 6.6   |
| #21 <sup>*</sup>                  | 23                    | 239     | 126      | 0.53 | 0.14        | 0.0613      | 0.0020 | 0.812      | 0.054  | 0.096      | 0.006  | 0.88 | 592                | 33        | 650         | 68        | 9.0   |
| #22 <sup>*</sup>                  | 8                     | 69      | 64       | 0.93 | 0.21        | 0.0631      | 0.0006 | 0.844      | 0.031  | 0.097      | 0.003  | 0.97 | 597                | 20        | 710         | 19        | 15.9  |
| #23                               | 36                    | 326     | 177      | 0.54 | 0.14        | 0.0613      | 0.0006 | 0.883      | 0.009  | 0.104      | 0.000  | 0.25 | 640                | 2         | 651         | 22        | 1.7   |
| #24 <sup>*</sup>                  | 24                    | 236     | 162      | 0.69 | 0.17        | 0.0617      | 0.0003 | 0.828      | 0.008  | 0.097      | 0.001  | 0.82 | 598                | 4         | 664         | 12        | 9.9   |
| #25 <sup>*</sup>                  | 25                    | 229     | 158      | 0.69 | 0.18        | 0.0611      | 0.0011 | 0.839      | 0.018  | 0.100      | 0.001  | 0.57 | 612                | 7         | 642         | 38        | 4.6   |
| #26 <sup>*</sup>                  | 21                    | 194     | 96       | 0.50 | 0.15        | 0.0605      | 0.0018 | 0.845      | 0.041  | 0.101      | 0.004  | 0.79 | 622                | 23        | 622         | 65        | 0.0   |
| #27 <sup>*</sup>                  | 21                    | 204     | 103      | 0.51 | 0.16        | 0.0633      | 0.0013 | 0.852      | 0.039  | 0.098      | 0.004  | 0.90 | 600                | 24        | 718         | 43        | 16.4  |
| #28 <sup>*</sup>                  | 22                    | 209     | 133      | 0.64 | 0.19        | 0.0604      | 0.0002 | 0.809      | 0.012  | 0.097      | 0.001  | 0.98 | 597                | 9         | 620         | 7         | 3.6   |
| #29                               | 15                    | 123     | 78       | 0.63 | 0.18        | 0.0630      | 0.0004 | 0.995      | 0.018  | 0.115      | 0.002  | 0.94 | 699                | 11        | 707         | 13        | 1.1   |
| #30                               | 84                    | 229     | 72       | 0.32 | 0.11        | 0.1291      | 0.0008 | 6.126      | 0.097  | 0.344      | 0.005  | 0.91 | 1906               | 24        | 2086        | 11        | 8.6   |
| #31                               | 26                    | 217     | 130      | 0.60 | 0.18        | 0.0611      | 0.0009 | 0.963      | 0.030  | 0.114      | 0.003  | 0.89 | 698                | 19        | 644         | 31        | -8.4  |
| #32                               | 68                    | 365     | 188      | 0.51 | 0.17        | 0.1102      | 0.0034 | 2.530      | 0.163  | 0.167      | 0.009  | 0.88 | 993                | 52        | 1802        | 55        | 44.9  |
| <b>Monzogranite 03-88 (Kidal)</b> |                       |         |          |      |             |             |        |            |        |            |        |      |                    |           |             |           |       |
| #1 <sup>*</sup>                   | 10                    | 90      | 48       | 0.54 | –           | 0.0601      | 0.0019 | 0.753      | 0.037  | 0.091      | 0.003  | 0.78 | 561                | 21        | 607         | 66        | 7.6   |
| #2 <sup>*</sup>                   | 12                    | 115     | 57       | 0.50 | –           | 0.0601      | 0.0015 | 0.770      | 0.034  | 0.093      | 0.003  | 0.83 | 573                | 20        | 606         | 52        | 5.5   |
| #3 <sup>*</sup>                   | 8                     | 83      | 55       | 0.66 | –           | 0.0608      | 0.0011 | 0.788      | 0.044  | 0.094      | 0.005  | 0.94 | 578                | 29        | 634         | 40        | 8.7   |
| #4 <sup>*</sup>                   | 18                    | 164     | 171      | 1.04 | –           | 0.0604      | 0.0015 | 0.784      | 0.055  | 0.094      | 0.006  | 0.94 | 580                | 37        | 617         | 52        | 6.0   |
| #5 <sup>*</sup>                   | 12                    | 111     | 105      | 0.95 | –           | 0.0602      | 0.0013 | 0.782      | 0.042  | 0.094      | 0.005  | 0.92 | 580                | 28        | 610         | 45        | 4.9   |
| #6 <sup>*</sup>                   | 9                     | 84      | 74       | 0.88 | –           | 0.0603      | 0.0016 | 0.787      | 0.038  | 0.095      | 0.004  | 0.83 | 583                | 22        | 615         | 57        | 5.3   |
| #7 <sup>*</sup>                   | 12                    | 99      | 97       | 0.98 | –           | 0.0587      | 0.0013 | 0.769      | 0.036  | 0.095      | 0.004  | 0.88 | 585                | 23        | 557         | 47        | -4.9  |
| #8 <sup>*</sup>                   | 11                    | 103     | 77       | 0.75 | –           | 0.0585      | 0.0013 | 0.768      | 0.028  | 0.095      | 0.003  | 0.81 | 586                | 16        | 550         | 46        | -6.5  |
| #9 <sup>*</sup>                   | 15                    | 160     | 50       | 0.31 | –           | 0.0601      | 0.0009 | 0.789      | 0.027  | 0.095      | 0.003  | 0.90 | 586                | 17        | 607         | 32        | 3.5   |
| #10 <sup>*</sup>                  | 11                    | 107     | 51       | 0.48 | –           | 0.0588      | 0.0016 | 0.775      | 0.039  | 0.096      | 0.004  | 0.83 | 589                | 23        | 560         | 60        | -5.2  |
| #11 <sup>*</sup>                  | 11                    | 95      | 87       | 0.92 | –           | 0.0601      | 0.0013 | 0.799      | 0.030  | 0.096      | 0.003  | 0.81 | 594                | 17        | 606         | 47        | 2.1   |
| #12 <sup>*</sup>                  | 9                     | 81      | 59       | 0.73 | –           | 0.0601      | 0.0018 | 0.801      | 0.027  | 0.097      | 0.002  | 0.50 | 595                | 10        | 609         | 63        | 2.3   |
| #13 <sup>*</sup>                  | 9                     | 76      | 74       | 0.97 | –           | 0.0587      | 0.0012 | 0.787      | 0.017  | 0.097      | 0.001  | 0.26 | 598                | 3         | 557         | 45        | -7.4  |
| #14 <sup>*</sup>                  | 9                     | 79      | 60       | 0.76 | –           | 0.0613      | 0.0020 | 0.821      | 0.027  | 0.097      | 0.000  | 0.14 | 598                | 3         | 648         | 68        | 7.7   |
| #15 <sup>*</sup>                  | 10                    | 91      | 90       | 0.99 | –           | 0.0578      | 0.0008 | 0.776      | 0.011  | 0.097      | 0.001  | 0.36 | 599                | 3         | 521         | 29        | -15.1 |
| #16 <sup>*</sup>                  | 12                    | 104     | 87       | 0.84 | –           | 0.0609      | 0.0021 | 0.827      | 0.029  | 0.098      | 0.001  | 0.19 | 605                | 4         | 637         | 72        | 5.0   |
| #17 <sup>*</sup>                  | 8                     | 66      | 53       | 0.80 | –           | 0.0601      | 0.0014 | 0.817      | 0.032  | 0.099      | 0.003  | 0.82 | 607                | 18        | 607         | 48        | 0.0   |
| #18 <sup>*</sup>                  | 9                     | 79      | 76       | 0.97 | –           | 0.0598      | 0.0013 | 0.831      | 0.031  | 0.101      | 0.003  | 0.82 | 619                | 18        | 597         | 46        | -3.7  |
| #19                               | 8                     | 69      | 44       | 0.64 | –           | 0.0677      | 0.0015 | 1.027      | 0.041  | 0.110      | 0.004  | 0.84 | 672                | 21        | 860         | 44        | 21.8  |
| #20                               | 11                    | 90      | 79       | 0.87 | –           | 0.0615      | 0.0010 | 0.939      | 0.038  | 0.111      | 0.004  | 0.92 | 678                | 24        | 656         | 34        | -3.3  |

Table 1 (Continued)

| Sample                              | Pb <sup>+</sup> (ppm) | U (ppm) | Th (ppm) | Th/U | 208Pb/206Pb | 207Pb/206Pb | ± (1σ) | 207Pb/235U | ± (1σ) | 206Pb/238U | ± (1σ) | Rho  | Apparent ages (Ma) |           |             |           | Disc% |
|-------------------------------------|-----------------------|---------|----------|------|-------------|-------------|--------|------------|--------|------------|--------|------|--------------------|-----------|-------------|-----------|-------|
|                                     |                       |         |          |      |             |             |        |            |        |            |        |      | 206Pb/238U         | ± (1(1σ)) | 207Pb/206Pb | ± (1(1σ)) |       |
| <b>Metadacite 03-08 (Kidal)</b>     |                       |         |          |      |             |             |        |            |        |            |        |      |                    |           |             |           |       |
| #1-1                                | 4                     | 40      | 28       | 0.71 | –           | 0.0608      | 0.0013 | 0.695      | 0.031  | 0.083      | 0.003  | 0.88 | 513                | 19        | 633         | 47        | 19.0  |
| #1-2*                               | 10                    | 102     | 59       | 0.58 | –           | 0.0615      | 0.0002 | 0.794      | 0.032  | 0.094      | 0.004  | 1.00 | 577                | 22        | 656         | 8         | 12.1  |
| #2*                                 | 13                    | 117     | 118      | 1.01 | –           | 0.0623      | 0.0007 | 0.840      | 0.040  | 0.098      | 0.005  | 0.97 | 601                | 27        | 684         | 23        | 12.1  |
| #3*                                 | 11                    | 100     | 114      | 1.14 | –           | 0.0607      | 0.0004 | 0.826      | 0.034  | 0.099      | 0.004  | 0.99 | 607                | 24        | 629         | 14        | 3.5   |
| #4*                                 | 4                     | 29      | 25       | 0.84 | –           | 0.0608      | 0.0004 | 0.835      | 0.030  | 0.099      | 0.004  | 0.98 | 611                | 21        | 634         | 14        | 3.5   |
| #5*                                 | 12                    | 104     | 94       | 0.91 | –           | 0.0615      | 0.0018 | 0.848      | 0.029  | 0.100      | 0.002  | 0.48 | 614                | 10        | 658         | 64        | 6.7   |
| #6*                                 | 6                     | 53      | 35       | 0.67 | –           | 0.0603      | 0.0022 | 0.835      | 0.031  | 0.100      | 0.001  | 0.22 | 617                | 5         | 615         | 77        | -0.2  |
| #7*                                 | 5                     | 43      | 20       | 0.46 | –           | 0.0597      | 0.0016 | 0.834      | 0.048  | 0.101      | 0.005  | 0.88 | 622                | 30        | 592         | 59        | -5.2  |
| #8*                                 | 3                     | 21      | 10       | 0.46 | –           | 0.0611      | 0.0016 | 0.859      | 0.026  | 0.102      | 0.002  | 0.51 | 626                | 9         | 644         | 57        | 2.8   |
| #9*                                 | 6                     | 56      | 22       | 0.39 | –           | 0.0605      | 0.0013 | 0.852      | 0.041  | 0.102      | 0.004  | 0.90 | 627                | 26        | 622         | 45        | -0.8  |
| #10*                                | 14                    | 118     | 83       | 0.70 | –           | 0.0718      | 0.0167 | 1.012      | 0.248  | 0.102      | 0.008  | 0.31 | 628                | 46        | 980         | 474       | 36.0  |
| #11*                                | 11                    | 103     | 92       | 0.89 | –           | 0.0607      | 0.0019 | 0.859      | 0.037  | 0.103      | 0.003  | 0.70 | 630                | 18        | 629         | 66        | -0.1  |
| #12*                                | 5                     | 42      | 13       | 0.31 | –           | 0.0612      | 0.0019 | 0.866      | 0.039  | 0.103      | 0.003  | 0.71 | 630                | 19        | 647         | 67        | 2.6   |
| #13*                                | 19                    | 180     | 94       | 0.52 | –           | 0.0614      | 0.0006 | 0.872      | 0.027  | 0.103      | 0.003  | 0.95 | 631                | 18        | 655         | 21        | 3.6   |
| #14*                                | 7                     | 65      | 37       | 0.56 | –           | 0.0610      | 0.0008 | 0.867      | 0.042  | 0.103      | 0.005  | 0.96 | 633                | 28        | 638         | 27        | 0.8   |
| #15*                                | 5                     | 39      | 17       | 0.44 | –           | 0.0615      | 0.0020 | 0.881      | 0.073  | 0.104      | 0.008  | 0.92 | 637                | 46        | 656         | 68        | 2.9   |
| #16*                                | 10                    | 86      | 75       | 0.87 | –           | 0.0615      | 0.0003 | 0.886      | 0.014  | 0.104      | 0.002  | 0.94 | 640                | 9         | 657         | 11        | 2.6   |
| #17*                                | 8                     | 65      | 64       | 1.00 | –           | 0.0608      | 0.0005 | 0.879      | 0.022  | 0.105      | 0.003  | 0.95 | 643                | 15        | 631         | 16        | -2.0  |
| #18                                 | 8                     | 71      | 54       | 0.77 | –           | 0.0703      | 0.0012 | 1.050      | 0.026  | 0.108      | 0.002  | 0.72 | 663                | 11        | 936         | 36        | 29.1  |
| #19                                 | 7                     | 62      | 17       | 0.28 | –           | 0.0636      | 0.0013 | 0.973      | 0.023  | 0.111      | 0.001  | 0.54 | 678                | 8         | 728         | 43        | 6.9   |
| #20                                 | 73                    | 288     | 87       | 0.30 | –           | 0.1122      | 0.0022 | 3.791      | 0.123  | 0.245      | 0.006  | 0.80 | 1413               | 33        | 1836        | 35        | 23.0  |
| #21                                 | 39                    | 106     | 166      | 1.56 | –           | 0.1077      | 0.0012 | 4.004      | 0.191  | 0.270      | 0.012  | 0.97 | 1539               | 63        | 1762        | 21        | 12.7  |
| #22                                 | 67                    | 91      | 166      | 1.82 | –           | 0.1964      | 0.0011 | 14.457     | 0.359  | 0.534      | 0.013  | 0.97 | 2757               | 54        | 2797        | 9         | 1.4   |
| <b>Orthogneiss 04-35 (Kidal)</b>    |                       |         |          |      |             |             |        |            |        |            |        |      |                    |           |             |           |       |
| #1                                  | 230                   | 969     | 170      | 0.17 | 0.08        | 0.1174      | 0.0005 | 3.690      | 0.188  | 0.228      | 0.012  | 1.00 | 1324               | 61        | 1917        | 7         | 30.9  |
| #2                                  | 185                   | 481     | 502      | 1.04 | 0.28        | 0.1177      | 0.0011 | 5.155      | 0.073  | 0.318      | 0.003  | 0.75 | 1778               | 16        | 1922        | 17        | 7.5   |
| #3                                  | 117                   | 323     | 256      | 0.79 | 0.22        | 0.1197      | 0.0007 | 5.116      | 0.167  | 0.310      | 0.010  | 0.98 | 1741               | 49        | 1951        | 11        | 10.8  |
| #4                                  | 117                   | 377     | 269      | 0.71 | 0.21        | 0.1203      | 0.0003 | 4.647      | 0.223  | 0.280      | 0.013  | 1.00 | 1592               | 67        | 1961        | 5         | 18.8  |
| #5*                                 | 99                    | 268     | 151      | 0.56 | 0.16        | 0.1209      | 0.0007 | 5.850      | 0.209  | 0.351      | 0.012  | 0.99 | 1939               | 59        | 1970        | 11        | 1.6   |
| #6*                                 | 100                   | 254     | 156      | 0.61 | 0.16        | 0.1215      | 0.0006 | 6.037      | 0.100  | 0.360      | 0.006  | 0.96 | 1984               | 27        | 1979        | 9         | -0.2  |
| #7*                                 | 118                   | 281     | 271      | 0.97 | 0.24        | 0.1220      | 0.0004 | 5.985      | 0.106  | 0.356      | 0.006  | 0.98 | 1962               | 29        | 1985        | 7         | 1.2   |
| #8*                                 | 169                   | 366     | 397      | 1.08 | 0.29        | 0.1221      | 0.0007 | 6.009      | 0.337  | 0.357      | 0.020  | 0.99 | 1968               | 94        | 1987        | 10        | 0.9   |
| #9*                                 | 124                   | 303     | 272      | 0.90 | 0.23        | 0.1222      | 0.0007 | 5.969      | 0.064  | 0.354      | 0.003  | 0.82 | 1954               | 15        | 1989        | 11        | 1.8   |
| #10                                 | 132                   | 376     | 230      | 0.61 | 0.16        | 0.1307      | 0.0006 | 5.678      | 0.199  | 0.315      | 0.011  | 0.99 | 1765               | 53        | 2108        | 8         | 16.3  |
| #11                                 | 271                   | 982     | 64       | 0.06 | 0.02        | 0.1320      | 0.0029 | 5.047      | 0.265  | 0.277      | 0.013  | 0.91 | 1578               | 67        | 2124        | 38        | 25.7  |
| #12                                 | 213                   | 636     | 97       | 0.15 | 0.04        | 0.1354      | 0.0021 | 6.131      | 0.143  | 0.328      | 0.006  | 0.76 | 1830               | 28        | 2169        | 26        | 15.6  |
| #13                                 | 289                   | 787     | 126      | 0.16 | 0.05        | 0.1422      | 0.0014 | 7.089      | 0.117  | 0.361      | 0.005  | 0.79 | 1989               | 22        | 2255        | 18        | 11.8  |
| #14                                 | 293                   | 1011    | 102      | 0.10 | 0.04        | 0.1435      | 0.0019 | 5.704      | 0.148  | 0.288      | 0.006  | 0.86 | 1633               | 32        | 2270        | 23        | 28.1  |
| <b>Garnetite IC218A (In Bezzeg)</b> |                       |         |          |      |             |             |        |            |        |            |        |      |                    |           |             |           |       |
| #1                                  | 42                    | 98      | 53       | 0.54 | 0.18        | 0.1376      | 0.0004 | 6.800      | 0.076  | 0.358      | 0.004  | 0.97 | 1975               | 18        | 2197        | 5         | 10.1  |
| #2*                                 | 53                    | 107     | 103      | 0.96 | 0.31        | 0.1225      | 0.0010 | 6.128      | 0.326  | 0.363      | 0.019  | 0.99 | 1995               | 89        | 1993        | 15        | -0.1  |
| #3*                                 | 56                    | 124     | 73       | 0.58 | 0.19        | 0.1222      | 0.0018 | 6.096      | 0.246  | 0.362      | 0.014  | 0.93 | 1990               | 64        | 1989        | 39        | -0.1  |
| #4                                  | 69                    | 120     | 116      | 0.97 | 0.27        | 0.1531      | 0.0009 | 9.176      | 0.231  | 0.435      | 0.011  | 0.97 | 2327               | 48        | 2381        | 10        | 2.3   |
| #5*                                 | 59                    | 120     | 106      | 0.89 | 0.24        | 0.1218      | 0.0010 | 5.947      | 0.078  | 0.354      | 0.004  | 0.78 | 1954               | 17        | 1983        | 13        | 1.5   |
| #7                                  | 74                    | 128     | 140      | 1.09 | 0.27        | 0.1626      | 0.0004 | 10.638     | 0.244  | 0.474      | 0.011  | 0.99 | 2503               | 47        | 2483        | 9         | -0.8  |
| #8*                                 | 42                    | 88      | 97       | 1.10 | 0.29        | 0.1230      | 0.0017 | 6.390      | 0.250  | 0.377      | 0.014  | 0.94 | 2062               | 64        | 2000        | 24        | -3.1  |
| #9*                                 | 41                    | 90      | 96       | 1.07 | 0.29        | 0.1226      | 0.0016 | 6.249      | 0.131  | 0.370      | 0.006  | 0.78 | 2028               | 29        | 1994        | 23        | -1.7  |
| #10*                                | 59                    | 156     | 61       | 0.39 | 0.11        | 0.1221      | 0.0009 | 5.961      | 0.110  | 0.354      | 0.006  | 0.91 | 1954               | 28        | 1987        | 14        | 1.7   |
| #11*                                | 74                    | 177     | 42       | 0.24 | 0.11        | 0.1221      | 0.0005 | 5.940      | 0.269  | 0.353      | 0.016  | 1.00 | 1948               | 76        | 1987        | 21        | 1.9   |
| #12*                                | 203                   | 476     | 33       | 0.07 | 0.03        | 0.1220      | 0.0002 | 6.032      | 0.200  | 0.359      | 0.012  | 1.00 | 1976               | 56        | 1985        | 7         | 0.5   |
| #13                                 | 58                    | 101     | 107      | 1.06 | 0.27        | 0.1551      | 0.0017 | 9.252      | 0.190  | 0.433      | 0.007  | 0.84 | 2318               | 33        | 2403        | 19        | 3.5   |
| #14                                 | 49                    | 94      | 86       | 0.91 | 0.25        | 0.1537      | 0.0009 | 8.598      | 0.125  | 0.406      | 0.005  | 0.91 | 2195               | 25        | 2387        | 10        | 8.0   |

Table 1 (Continued)

| Sample                                | Pb <sup>+</sup> (ppm) | U (ppm) | Th (ppm) | Th/U  | 208Pb/206Pb | 207Pb/206Pb | ± (1σ) | 207Pb/235U | ± (1σ) | 206Pb/238U | ± (1σ) | Rho  | Apparent ages (Ma) |           |             |           | Disc% |
|---------------------------------------|-----------------------|---------|----------|-------|-------------|-------------|--------|------------|--------|------------|--------|------|--------------------|-----------|-------------|-----------|-------|
|                                       |                       |         |          |       |             |             |        |            |        |            |        |      | 206Pb/238U         | ± (1(1σ)) | 207Pb/206Pb | ± (1(1σ)) |       |
| #15 <sup>*</sup>                      | 175                   | 495     | 132      | 0.27  | 0.10        | 0.1220      | 0.0008 | 5.986      | 0.229  | 0.356      | 0.013  | 0.99 | 1962               | 64        | 1986        | 11        | 1.2   |
| #16 <sup>*</sup>                      | 55                    | 128     | 96       | 0.75  | 0.16        | 0.1302      | 0.0008 | 6.609      | 0.048  | 0.368      | 0.001  | 0.47 | 2021               | 6         | 2100        | 11        | 3.8   |
| #17 <sup>*</sup>                      | 30                    | 55      | 65       | 1.18  | 0.30        | 0.1611      | 0.0016 | 9.334      | 0.152  | 0.420      | 0.005  | 0.80 | 2261               | 25        | 2468        | 16        | 8.4   |
| #18 <sup>*</sup>                      | 221                   | 573     | 64       | 0.11  | 0.02        | 0.1218      | 0.0004 | 5.983      | 0.225  | 0.356      | 0.013  | 1.00 | 1965               | 63        | 1983        | 6         | 0.9   |
| #19 <sup>*</sup>                      | 44                    | 74      | 67       | 0.91  | 0.25        | 0.1595      | 0.0012 | 10.231     | 0.101  | 0.465      | 0.003  | 0.65 | 2462               | 13        | 2451        | 13        | -0.5  |
| #20 <sup>*</sup>                      | 48                    | 101     | 86       | 0.85  | 0.28        | 0.1230      | 0.0010 | 6.327      | 0.116  | 0.373      | 0.006  | 0.89 | 2044               | 29        | 2000        | 15        | -2.2  |
| #21 <sup>*</sup>                      | 216                   | 588     | 35       | 0.06  | 0.02        | 0.1215      | 0.0006 | 5.954      | 0.180  | 0.355      | 0.011  | 0.99 | 1960               | 50        | 1979        | 8         | 0.9   |
| #22 <sup>*</sup>                      | 61                    | 106     | 105      | 0.99  | 0.27        | 0.1610      | 0.0011 | 10.099     | 0.116  | 0.455      | 0.004  | 0.81 | 2417               | 19        | 2466        | 11        | 2.0   |
| #23 <sup>*</sup>                      | 150                   | 419     | 29       | 0.07  | 0.02        | 0.1226      | 0.0004 | 6.138      | 0.194  | 0.363      | 0.011  | 1.00 | 1997               | 54        | 1994        | 5         | -0.2  |
| #24 <sup>*</sup>                      | 37                    | 81      | 95       | 1.17  | 0.27        | 0.1232      | 0.0009 | 6.410      | 0.094  | 0.377      | 0.005  | 0.88 | 2063               | 23        | 2004        | 13        | -3.0  |
| <b>Allanite 04-40 (IGU)</b>           |                       |         |          |       |             |             |        |            |        |            |        |      |                    |           |             |           |       |
| #1 <sup>*</sup>                       | 169                   | 93      | 1191     | 12.75 | 3.86        | 0.1219      | 0.0007 | 6.130      | 0.061  | 0.365      | 0.003  | 0.83 | 2005               | 14        | 1984        | 10        | -1.0  |
| #2 <sup>*</sup>                       | 175                   | 98      | 1239     | 12.66 | 3.75        | 0.1225      | 0.0007 | 6.209      | 0.063  | 0.368      | 0.003  | 0.82 | 2018               | 14        | 1993        | 10        | -1.3  |
| #3 <sup>*</sup>                       | 177                   | 100     | 1261     | 12.62 | 3.81        | 0.1219      | 0.0005 | 6.065      | 0.050  | 0.361      | 0.003  | 0.85 | 1987               | 12        | 1984        | 8         | -0.2  |
| #4 <sup>*</sup>                       | 164                   | 94      | 1241     | 13.25 | 4.01        | 0.1212      | 0.0006 | 5.782      | 0.077  | 0.346      | 0.004  | 0.93 | 1915               | 21        | 1974        | 9         | 3.0   |
| #5 <sup>*</sup>                       | 195                   | 88      | 1432     | 16.19 | 4.69        | 0.1225      | 0.0006 | 6.343      | 0.054  | 0.375      | 0.003  | 0.80 | 2055               | 12        | 1994        | 9         | -3.1  |
| #6 <sup>*</sup>                       | 167                   | 83      | 1225     | 14.80 | 4.50        | 0.1213      | 0.0007 | 6.160      | 0.049  | 0.368      | 0.002  | 0.73 | 2021               | 10        | 1976        | 10        | -2.3  |
| #7 <sup>*</sup>                       | 174                   | 92      | 1243     | 13.56 | 4.13        | 0.1228      | 0.0006 | 6.221      | 0.042  | 0.367      | 0.002  | 0.63 | 2017               | 7         | 1998        | 9         | -0.9  |
| #8 <sup>*</sup>                       | 178                   | 79      | 1298     | 16.45 | 5.04        | 0.1220      | 0.0008 | 6.142      | 0.080  | 0.365      | 0.004  | 0.88 | 2006               | 20        | 1986        | 11        | -1.0  |
| #9 <sup>*</sup>                       | 155                   | 91      | 1172     | 12.95 | 4.14        | 0.1290      | 0.0006 | 5.906      | 0.064  | 0.332      | 0.003  | 0.91 | 1848               | 16        | 2085        | 8         | 11.3  |
| <b>Orthogneiss 04-14 (Tin essako)</b> |                       |         |          |       |             |             |        |            |        |            |        |      |                    |           |             |           |       |
| #1 <sup>*</sup>                       | 59                    | 148     | 57       | 0.39  | 0.15        | 0.1241      | 0.0008 | 6.300      | 0.093  | 0.368      | 0.005  | 0.90 | 2020               | 23        | 2017        | 12        | -0.2  |
| #1-2 <sup>*</sup>                     | 54                    | 141     | 27       | 0.19  | 0.06        | 0.1243      | 0.0004 | 6.202      | 0.112  | 0.362      | 0.006  | 0.99 | 1991               | 31        | 2019        | 5         | 1.4   |
| #2 <sup>*</sup>                       | 65                    | 177     | 26       | 0.15  | 0.05        | 0.1247      | 0.0016 | 6.157      | 0.106  | 0.358      | 0.004  | 0.66 | 1973               | 19        | 2024        | 23        | 2.5   |
| #3 <sup>*</sup>                       | 69                    | 184     | 57       | 0.31  | 0.09        | 0.1243      | 0.0013 | 6.082      | 0.108  | 0.355      | 0.005  | 0.82 | 1958               | 25        | 2019        | 18        | 3.0   |
| #4 <sup>*</sup>                       | 135                   | 343     | 118      | 0.34  | 0.09        | 0.1242      | 0.0005 | 6.443      | 0.194  | 0.376      | 0.011  | 0.99 | 2058               | 52        | 2018        | 7         | -2.0  |
| #5 <sup>*</sup>                       | 56                    | 148     | 62       | 0.42  | 0.12        | 0.1251      | 0.0006 | 6.340      | 0.193  | 0.368      | 0.011  | 0.99 | 2018               | 52        | 2030        | 8         | 0.5   |
| #6 <sup>*</sup>                       | 80                    | 217     | 55       | 0.25  | 0.07        | 0.1248      | 0.0004 | 6.340      | 0.137  | 0.369      | 0.008  | 0.99 | 2023               | 37        | 2025        | 6         | 0.1   |
| #7 <sup>*</sup>                       | 85                    | 229     | 36       | 0.16  | 0.05        | 0.1247      | 0.0005 | 6.536      | 0.235  | 0.380      | 0.014  | 0.99 | 2076               | 63        | 2025        | 7         | -2.5  |
| #8 <sup>*</sup>                       | 122                   | 329     | 138      | 0.42  | 0.09        | 0.1240      | 0.0003 | 5.907      | 0.035  | 0.346      | 0.002  | 0.90 | 1914               | 9         | 2014        | 5         | 5.0   |
| #9 <sup>*</sup>                       | 60                    | 149     | 68       | 0.46  | 0.19        | 0.1276      | 0.0006 | 6.414      | 0.210  | 0.364      | 0.012  | 0.99 | 2003               | 56        | 2066        | 9         | 3.0   |
| #10 <sup>*</sup>                      | 87                    | 196     | 128      | 0.65  | 0.16        | 0.1286      | 0.0006 | 6.815      | 0.241  | 0.384      | 0.013  | 0.99 | 2096               | 62        | 2079        | 9         | -0.8  |
| #11 <sup>*</sup>                      | 73                    | 209     | 40       | 0.19  | 0.07        | 0.1231      | 0.0006 | 5.788      | 0.167  | 0.341      | 0.010  | 0.99 | 1892               | 47        | 2001        | 8         | 5.4   |
| #12 <sup>*</sup>                      | 68                    | 201     | 39       | 0.20  | 0.05        | 0.1243      | 0.0018 | 5.648      | 0.167  | 0.329      | 0.008  | 0.87 | 1836               | 41        | 2019        | 26        | 9.1   |
| #13 <sup>*</sup>                      | 78                    | 233     | 88       | 0.38  | 0.11        | 0.1273      | 0.0004 | 5.511      | 0.147  | 0.314      | 0.008  | 0.99 | 1760               | 41        | 2061        | 6         | 14.6  |
| #14 <sup>*</sup>                      | 76                    | 215     | 44       | 0.21  | 0.04        | 0.1243      | 0.0011 | 5.760      | 0.108  | 0.336      | 0.006  | 0.88 | 1868               | 27        | 2019        | 16        | 7.5   |
| <b>Metadiorite 03-12 (Tamaradant)</b> |                       |         |          |       |             |             |        |            |        |            |        |      |                    |           |             |           |       |
| #1 <sup>*</sup>                       | 14                    | 130     | 110      | 0.85  | -           | 0.0590      | 0.0010 | 0.848      | 0.052  | 0.104      | 0.006  | 0.96 | 639                | 36        | 567         | 37        | -12.8 |
| #2 <sup>*</sup>                       | 13                    | 122     | 112      | 0.92  | -           | 0.0595      | 0.0024 | 0.819      | 0.039  | 0.100      | 0.003  | 0.52 | 613                | 15        | 586         | 86        | -4.6  |
| #3 <sup>*</sup>                       | 12                    | 105     | 85       | 0.81  | -           | 0.0617      | 0.0027 | 0.893      | 0.048  | 0.105      | 0.003  | 0.58 | 643                | 19        | 663         | 92        | 3.0   |
| #4 <sup>*</sup>                       | 12                    | 114     | 72       | 0.63  | -           | 0.0607      | 0.0010 | 0.837      | 0.024  | 0.100      | 0.002  | 0.83 | 614                | 14        | 629         | 34        | 2.4   |
| #5 <sup>*</sup>                       | 11                    | 98      | 72       | 0.73  | -           | 0.0617      | 0.0009 | 0.874      | 0.020  | 0.103      | 0.002  | 0.78 | 630                | 11        | 663         | 30        | 5.0   |
| #6 <sup>*</sup>                       | 15                    | 136     | 101      | 0.75  | -           | 0.0623      | 0.0027 | 0.895      | 0.042  | 0.104      | 0.002  | 0.40 | 639                | 12        | 685         | 89        | 6.7   |
| #7 <sup>*</sup>                       | 13                    | 124     | 76       | 0.61  | -           | 0.0614      | 0.0021 | 0.874      | 0.035  | 0.103      | 0.002  | 0.51 | 633                | 12        | 655         | 72        | 3.4   |
| #8 <sup>*</sup>                       | 22                    | 201     | 164      | 0.82  | -           | 0.0616      | 0.0016 | 0.854      | 0.035  | 0.100      | 0.003  | 0.79 | 617                | 19        | 661         | 53        | 6.7   |
| #9 <sup>*</sup>                       | 16                    | 161     | 136      | 0.85  | -           | 0.0612      | 0.0018 | 0.821      | 0.071  | 0.097      | 0.008  | 0.94 | 598                | 46        | 647         | 61        | 7.6   |
| #10 <sup>*</sup>                      | 31                    | 314     | 188      | 0.60  | -           | 0.0618      | 0.0015 | 0.829      | 0.054  | 0.097      | 0.006  | 0.92 | 599                | 35        | 665         | 52        | 10.0  |
| #11 <sup>*</sup>                      | 30                    | 299     | 209      | 0.70  | -           | 0.0625      | 0.0011 | 0.879      | 0.030  | 0.102      | 0.003  | 0.86 | 627                | 17        | 690         | 37        | 9.2   |
| #12 <sup>*</sup>                      | 14                    | 132     | 81       | 0.62  | -           | 0.0609      | 0.0015 | 0.885      | 0.025  | 0.105      | 0.001  | 0.45 | 646                | 8         | 636         | 53        | -1.5  |
| #13 <sup>*</sup>                      | 11                    | 108     | 58       | 0.53  | -           | 0.0604      | 0.0027 | 0.858      | 0.039  | 0.103      | 0.001  | 0.24 | 632                | 7         | 617         | 93        | -2.4  |
| #14 <sup>*</sup>                      | 11                    | 102     | 60       | 0.59  | -           | 0.0626      | 0.0018 | 0.885      | 0.031  | 0.103      | 0.002  | 0.60 | 629                | 13        | 694         | 59        | 9.3   |
| #15 <sup>*</sup>                      | 10                    | 89      | 58       | 0.65  | -           | 0.0608      | 0.0025 | 0.847      | 0.052  | 0.101      | 0.005  | 0.75 | 621                | 27        | 633         | 86        | 1.9   |

Table 1 (Continued)

| Sample | Pb* (ppm) | U (ppm) | Th (ppm) | Th/U | 208Pb/206Pb | 207Pb/206Pb | $\pm (1\sigma)$ | 207Pb/235U | $\pm (1\sigma)$ | 206Pb/238U | $\pm (1\sigma)$ | Rho  | Apparent ages (Ma) | $\pm (1(1\sigma))$ | Disc% |     |       |
|--------|-----------|---------|----------|------|-------------|-------------|-----------------|------------|-----------------|------------|-----------------|------|--------------------|--------------------|-------|-----|-------|
| #16*   | 10        | 93      | 53       | 0.57 | -           | 0.0618      | 0.0026          | 0.821      | 0.041           | 0.096      | 0.003           | 0.52 | 593                | 15                 | 667   | 89  | 11.1  |
| #17    | 11        | 96      | 47       | 0.49 | -           | 0.0608      | 0.0021          | 0.886      | 0.036           | 0.106      | 0.002           | 0.56 | 648                | 14                 | 631   | 71  | -2.8  |
| #18*   | 10        | 94      | 53       | 0.56 | -           | 0.0618      | 0.0026          | 0.850      | 0.042           | 0.100      | 0.003           | 0.55 | 613                | 16                 | 666   | 87  | 8.0   |
| #19*   | 12        | 105     | 70       | 0.66 | -           | 0.0608      | 0.0017          | 0.838      | 0.040           | 0.100      | 0.004           | 0.82 | 614                | 23                 | 632   | 58  | 2.8   |
| #20*   | 13        | 117     | 82       | 0.70 | -           | 0.0617      | 0.0020          | 0.895      | 0.039           | 0.105      | 0.003           | 0.66 | 645                | 18                 | 664   | 69  | 3.0   |
| #21*   | 13        | 118     | 105      | 0.89 | -           | 0.0607      | 0.0021          | 0.871      | 0.035           | 0.104      | 0.002           | 0.50 | 638                | 12                 | 629   | 74  | -1.4  |
| #22*   | 11        | 100     | 69       | 0.69 | -           | 0.0582      | 0.0038          | 0.798      | 0.054           | 0.100      | 0.002           | 0.29 | 612                | 11                 | 536   | 135 | -14.2 |
| #23    | 13        | 104     | 66       | 0.64 | -           | 0.0657      | 0.0031          | 1.140      | 0.055           | 0.126      | 0.001           | 0.23 | 764                | 8                  | 798   | 96  | 4.2   |
| #24    | 14        | 128     | 79       | 0.62 | -           | 0.0629      | 0.0021          | 0.951      | 0.036           | 0.110      | 0.002           | 0.51 | 671                | 12                 | 706   | 68  | 4.9   |
| #25    | 9         | 71      | 53       | 0.75 | -           | 0.0638      | 0.0023          | 0.976      | 0.046           | 0.111      | 0.003           | 0.62 | 678                | 19                 | 735   | 76  | 7.6   |
| #26    | 61        | 173     | 61       | 0.35 | -           | 0.1282      | 0.0012          | 5.888      | 0.171           | 0.333      | 0.009           | 0.94 | 1854               | 44                 | 2073  | 17  | 10.6  |
| #27    | 11        | 89      | 53       | 0.60 | -           | 0.0628      | 0.0018          | 0.978      | 0.034           | 0.113      | 0.002           | 0.59 | 690                | 13                 | 701   | 58  | 1.6   |

\* Analyses taken into account for age calculation.

Disc. (%) is percentage discordance assuming zero-age Pb losses.

(MSWD = 1.3) that we relate to crystallization of the sub-alkali granite. Two analyses (#5 and #16) were performed on cores surrounded by oscillatory zoned domains and they define ages of  $766 \pm 34$  Ma and  $774 \pm 30$  Ma ( $2\sigma$ ) that are attributed to an inherited component.

#### 4.2. Kidal terrane

##### 4.2.1. Syenitic gneiss IC622

Zircons extracted from the syenitic gneiss IC622 are euhedral to subhedral with oscillatory zoning (Fig. 5d) and often display zoned or unzoned inherited cores in their central part. Four analyses of completely zoned grains and zoned rims around cores (Table 1 and Fig. 5d) have consistent ages and yield a weighted mean  $^{207}\text{Pb}/^{206}\text{Pb}$  age of  $1966 \pm 9$  Ma (MSWD = 0.7), which is adopted as our best estimate of the age of crystallization of zircon from the syenitic magma. The remaining analyses of unzoned zircons and cores are significantly older than 1966 Ma and demonstrate that the zircon population contains a significant inherited component. On a Concordia plot (Fig. 6d) most data points fall close to concordia at c. 2113 Ma ( $n=1$ ) and between 2308 and 2472 Ma. The scattered position of the data points can be explained if the inherited zircons derived from source rocks with a range of ages mainly ranging from Late Archean to Early Paleoproterozoic. Due to analytical errors, a single source, close to 2.5 Ga can also be envisioned but requires various degrees of Pb losses from the cores at 1966 Ma. A least-square calculation of the upper intercept age is not realistic as some data points fall below a chord connecting the 1966 Ma lower intercept and an hypothetical c. 2.5 Ga upper intercept, indicating that these points have undergone mild, relatively recent, Pb losses.

##### 4.2.2. Tonalite N188

Zircons are translucent colorless with euhedral to subhedral shapes and display oscillatory zoning reflecting a magmatic crystallization (Fig. 5e). Inherited cores, either zoned or unzoned, have been also detected. Completely zoned zircons are concordant within error margins (Fig. 6e) and provide a  $^{206}\text{Pb}/^{238}\text{U}$  weighted mean age of  $604 \pm 5$  Ma (MSWD = 0.8;  $n=27/28$ ). This age is taken as our best estimate for crystallization of the zircons from the tonalitic magma. Core analyses yield significantly older ages (see Table 1), which are either Neoproterozoic (c. 700 Ma for analyses #29 and #31) or older (analyses #30 and #32). The oldest core (#30) has a minimum age of  $2086 \pm 22$  Ma ( $2\sigma$ ) or a more realistic projected age (through 604 Ma) of 2131 Ma, which is comparable to the youngest inherited component in the syenitic gneiss IC622 (2113 Ma). However, conversely to that sample, no early Paleoproterozoic component was identified.

##### 4.2.3. Monzogranite 03-88

Twenty zircon grains with euhedral shapes and oscillatory zoning attributed to a sequential growth in the magma have been analyzed and all grains but two plot concordantly at c. 600 Ma (Fig. 6f). The weighted mean age of these analyses is  $599 \pm 4$  Ma (MSWD = 1.4), which is attributed to the magmatic crystallization of the zircons in the monzogranite. On the two remaining analyses only one is concordant at  $678 \pm 48$  Ma ( $2\sigma$ ) and reflects the age of an inherited component.

##### 4.2.4. Tafeliant metadacite 03-08

Zircon grains from the metadacite are translucent colorless with euhedral to subhedral shapes and oscillatory zoning (Fig. 5f). Some have cores of zoned or unzoned zircon surrounded unconformably by oscillatory zoned zircon. Sixteen analyses of zoned grains are concordant (Fig. 6g) within errors and provide a  $^{206}\text{Pb}/^{238}\text{U}$  weighted mean age of  $623 \pm 6$  Ma (MSWD = 1.0). This is interpreted as the age of magmatic crystallization of zircon in the metadacite.

**Table 2**

Major (wt%), trace element (in ppm) and Sr–Nd isotopes for whole-rocks from the Tafeliant, Kidal and Tamaradant domains. The isotopic compositions have been calculated at 660 Ma, 1000 Ma and/or 1800 Ma (see text for details). Nd model ages have been calculated only for samples with  $^{147}\text{Sm}/^{144}\text{Nd} < 0.165$  in agreement with Stern (2002).

| Sample Name  | Tafeliant  |             | Kidal (West of IGU) |            |            |            | Kidal (North and East of IGU) |             | Tamaradant |            |
|--|------------|-------------|---------------------|------------|------------|------------|-------------------------------|-------------|------------|------------|
|  | 03-4A      | 03-4B       | 03-11B              | 04-43      | 04-45      | 03-30      | 04-27A                        | 04-31       | 04-10      | 04-11      |
| <b>Major elements (wt%)</b>                        |            |             |                     |            |            |            |                               |             |            |            |
| SiO <sub>2</sub>                                   | 51.87      | 46.12       | 49.02               | 43.38      | 43.77      | 48.83      | 41.57                         | 47.53       | 53.37      | 49.36      |
| Al <sub>2</sub> O <sub>3</sub>                     | 16.19      | 17.24       | 13.18               | 15.34      | 7.928      | 13.79      | 14.26                         | 16.52       | 28.27      | 22.07      |
| Fe <sub>2</sub> O <sub>3</sub>                     | 11.28      | 11.73       | 13.61               | 16.1       | 11.67      | 12.09      | 19.82                         | 17.59       | 0.51       | 6.4        |
| MnO  | 0.18       | 0.17        | 0.23                | 0.27       | 0.16       | 0.18       | 0.29                          | 0.39        | 0.01       | 0.09       |
| MgO  | 3.48       | 6.23        | 7.24                | 9.2        | 20.63      | 7.76       | 8.54                          | 9.16        | 0.25       | 5.42       |
| CaO  | 11.24      | 11.87       | 11.16               | 12.55      | 9.22       | 10.82      | 11.61                         | 6.72        | 11.02      | 12.97      |
| Na <sub>2</sub> O                                  | 1.2        | 2.35        | 2.15                | 1.14       | 0.67       | 2.42       | 1.04                          | 0.38        | 5.43       | 2.67       |
| K <sub>2</sub> O                                   | 0.12       | 0.11        | 0.38                | 0.13       | 0.13       | 0.31       | –                             | 0.07        | 0.06       | 0.14       |
| TiO <sub>2</sub>                                   | 2.39       | 1.76        | 1.09                | 1.46       | 0.72       | 1.29       | 3.08                          | 1.14        | 0.15       | 0.47       |
| P <sub>2</sub> O <sub>5</sub>                      | 0.32       | 0.21        | 0.09                | 0.13       | 0.05       | 0.09       | 0.55                          | 0.1         | –          | –          |
| LOI  | 0.58       | 1.03        | 1.24                | –          | 3.69       | 1.34       | –                             | –           | 0.79       | 0.82       |
| Sum  | 98.85      | 98.83       | 99.38               | 99.63      | 98.64      | 98.92      | 99.8                          | 99.1        | 99.87      | 100.42     |
| <b>Trace elements (ppm)</b>                        |            |             |                     |            |            |            |                               |             |            |            |
| Rb   | 1.03       | 1.42        | 14.55               | 4.14       | 1.72       | 8.97       | 0.42                          | 1.96        | 0.25       | 0.85       |
| Sr   | 251.69     | 494.48      | 132.29              | 83.32      | 69.27      | 214.63     | 51.92                         | 13.76       | 267.58     | 226.36     |
| Y  | 37.69      | 26.99       | 24.8                | 22.88      | 11.98      | 19.76      | 56.6                          | 57.5        | 1.26       | 8.45       |
| Zr   | 144.64     | 39.84       | 21.69               | 14.49      | 23.16      | 14.69      | 56.64                         | 53.17       | 1.66       | 11.58      |
| Nb   | 10.12      | 7.68        | 1.86                | 3.38       | 1.52       | 3.99       | 24.81                         | 13.17       | 0.46       | 1.04       |
| Cs   | 0.02       | 0.05        | 0.28                | 0.19       | 0.02       | 1.14       | 0.01                          | 0.05        | 0.01       | 0.01       |
| Ba   | 224.47     | 80.06       | 335.75              | 34.19      | 43.27      | 77.86      | 53.01                         | 18.77       | 204.83     | 64.62      |
| La   | 14.52      | 9.81        | 4.88                | 3.44       | 1.68       | 4.52       | 17.82                         | 8.4         | 1.95       | 3.39       |
| Ce   | 35.53      | 24.48       | 11.96               | 10.2       | 4.97       | 12.06      | 48.8                          | 23.3        | 3.66       | 7.68       |
| Pr   | 4.86       | 3.36        | 1.68                | 1.59       | 0.79       | 1.76       | 6.78                          | 3.49        | 0.42       | 1.02       |
| Nd   | 23.5       | 16.42       | 8.55                | 8.79       | 4.46       | 9.31       | 32.34                         | 18.98       | 1.72       | 4.98       |
| Sm   | 5.99       | 4.21        | 2.56                | 2.67       | 1.5        | 2.78       | 7.96                          | 8.37        | 0.32       | 1.23       |
| Eu   | 2.06       | 1.53        | 0.93                | 1.09       | 0.62       | 1.08       | 2.5                           | 1.96        | 0.55       | 0.8        |
| Gd   | 7.04       | 4.89        | 3.5                 | 3.63       | 2.14       | 3.64       | 9.49                          | 11.05       | 0.35       | 1.5        |
| Tb   | 1.1        | 0.77        | 0.61                | 0.64       | 0.36       | 0.58       | 1.54                          | 1.88        | 0.04       | 0.24       |
| Dy   | 7.14       | 5.01        | 4.41                | 4.36       | 2.35       | 3.84       | 10.08                         | 11.3        | 0.26       | 1.58       |
| Ho   | 1.4        | 0.99        | 0.93                | 0.88       | 0.46       | 0.76       | 2.06                          | 2.1         | 0.054      | 0.31       |
| Er   | 3.8        | 2.58        | 2.54                | 2.52       | 1.22       | 2.03       | 5.48                          | 5.53        | 0.14       | 0.89       |
| Tm   | 0.53       | 0.37        | 0.38                | 0.37       | 0.17       | 0.28       | 0.81                          | 0.8         | 0.021      | 0.12       |
| Yb   | 3.28       | 2.18        | 2.39                | 2.16       | 1.06       | 1.75       | 5.06                          | 4.28        | 0.119      | 0.77       |
| Lu   | 0.53       | 0.35        | 0.39                | 0.37       | 0.17       | 0.28       | 0.83                          | 0.71        | 0.018      | 0.13       |
| Hf   | 3.75       | 1.19        | 0.65                | 0.65       | 0.68       | 0.74       | 2.00                          | 1.28        | 0.053      | 0.38       |
| Ta   | 0.68       | 0.51        | 0.099               | 0.21       | 0.098      | 0.27       | 1.62                          | 1.12        | 0.025      | 0.09       |
| Pb   | 2.41       | 2.11        | 1.88                | 1.003      | 1.76       | 0.52       | 0.41                          | 0.93        | 1.65       | 1.2        |
| Th   | 1.73       | 1.12        | 0.84                | 0.027      | 0.13       | 0.35       | 0.45                          | 1.32        | 0.062      | 0.23       |
| U  | 0.45       | 0.31        | 0.23                | 0.012      | 0.053      | 0.11       | 0.42                          | 0.4         | 0.033      | 0.06       |
| Nb/Ta  | 14.8       | 15.0        | 18.8                | 16.5       | 15.4       | 14.7       | 15.3                          | 11.8        | 18.3       | 11.5       |
| (La/Yb) <sub>N</sub>                               | 3.01       | 3.06        | 1.39                | 1.08       | 1.08       | 1.75       | 2.39                          | 1.33        | 11.13      | 2.99       |
| (La/Sm) <sub>N</sub>                               | 1.57       | 1.51        | 1.23                | 0.83       | 0.72       | 1.05       | 1.45                          | 0.65        | 3.97       | 1.77       |
| $^{143}\text{Nd}/^{144}\text{Nd}$                  | 0.512721±5 | 0.5127297±6 | 0.512722±4          | 0.512837±4 | 0.512998±3 | 0.512866±4 | 0.512195±5                    | 0.512986±7  | 0.511815±6 | 0.512307±4 |
| $^{147}\text{Sm}/^{144}\text{Nd}$                  | 0.154      | 0.155       | 0.181               | 0.183      | 0.204      | 0.181      | 0.149                         | 0.267       | 0.111      | 0.15       |
| ( $\varepsilon\text{Nd}$ ) <sub>660 Ma</sub>       | 5.2        | 5.3         | –                   | –          | –          | –          | –                             | –           | -8.9       | -2.5       |
| ( $\varepsilon\text{Nd}$ ) <sub>1000 Ma</sub>      | –          | –           | 3.6                 | 5.6        | 6.1        | 6.5        | -2.5                          | -2.1        | -5.1       | -0.5       |
| ( $\varepsilon\text{Nd}$ ) <sub>1800 Ma</sub>      | –          | –           | –                   | –          | –          | –          | 2.5                           | -9.3        | –          | –          |
| TDM (Ma)   | 943        | 935         | –                   | –          | –          | –          | 1986                          | –           | 1832       | 1774       |
| $^{87}\text{Sr}/^{86}\text{Sr}$                    | 0.703595±5 | 0.703202±8  | 0.709767±4          | 0.705399±6 | 0.704504±5 | 0.705178±7 | 0.720310±7                    | 0.744612±11 | 0.703693±4 | 0.703638±3 |
| $^{87}\text{Rb}/^{86}\text{Sr}$                    | 0.012      | 0.008       | 0.318               | 0.144      | 0.072      | 0.121      | 0.024                         | 0.0413      | 0.003      | 0.011      |
| $^{87}\text{Sr}/^{86}\text{Sr}$ <sub>660 Ma</sub>  | 0.70348    | 0.70312     | –                   | –          | –          | –          | –                             | –           | 0.70367    | 0.70354    |
| $^{87}\text{Sr}/^{86}\text{Sr}$ <sub>1000 Ma</sub> | –          | –           | 0.70522             | 0.70334    | 0.70348    | 0.70345    | 0.71997                       | 0.73871     | 0.70365    | 0.70348    |
| $^{87}\text{Sr}/^{86}\text{Sr}$ <sub>1800 Ma</sub> | –          | –           | –                   | –          | –          | –          | 0.71969                       | 0.73392     | –          | –          |

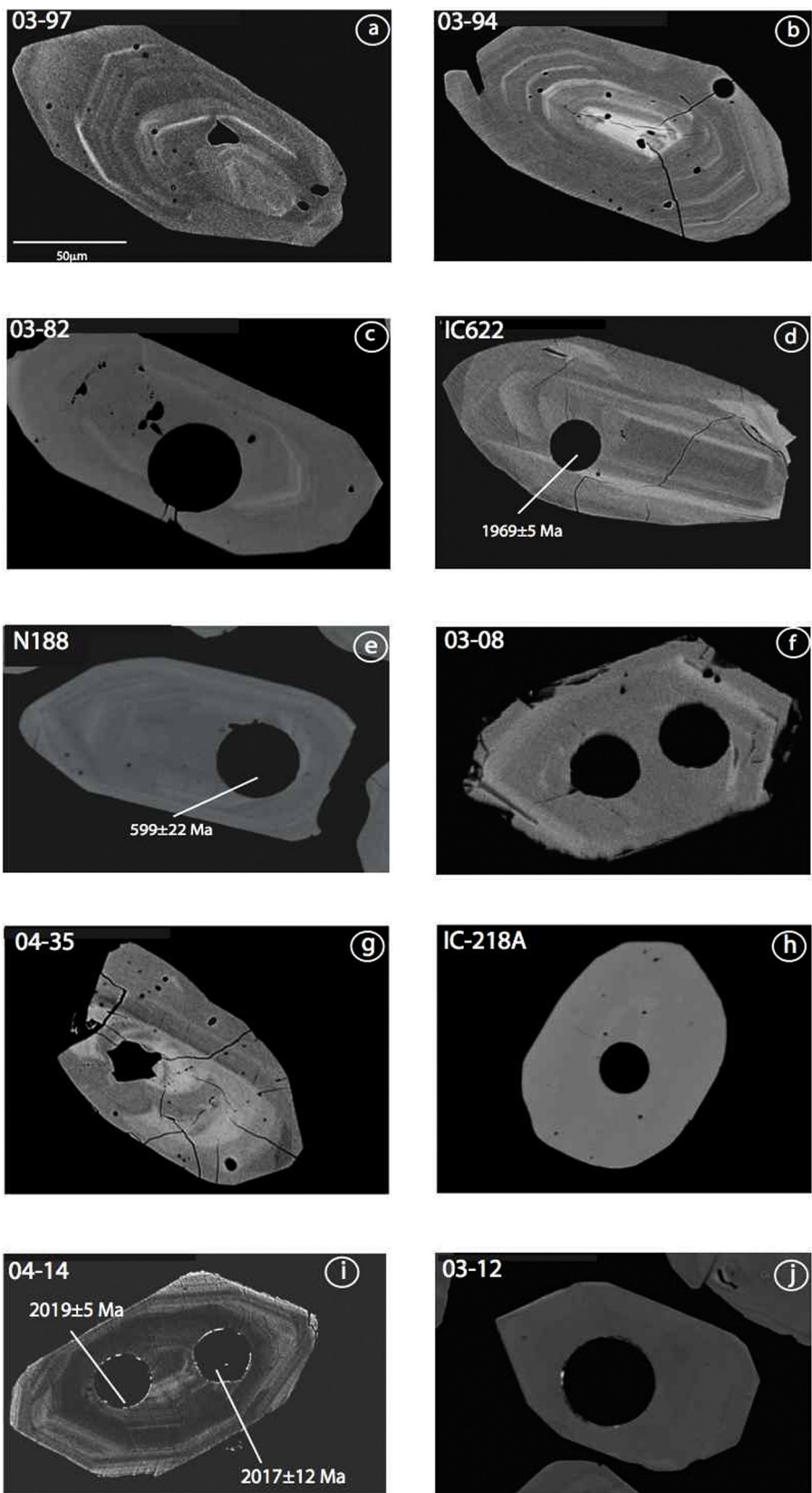


**Fig. 5.** Back-scattered electron (BSE) images of zircon grains from the studied rocks. Spot size is 26  $\mu\text{m}$ . Ages are  $\pm 1\sigma$ .

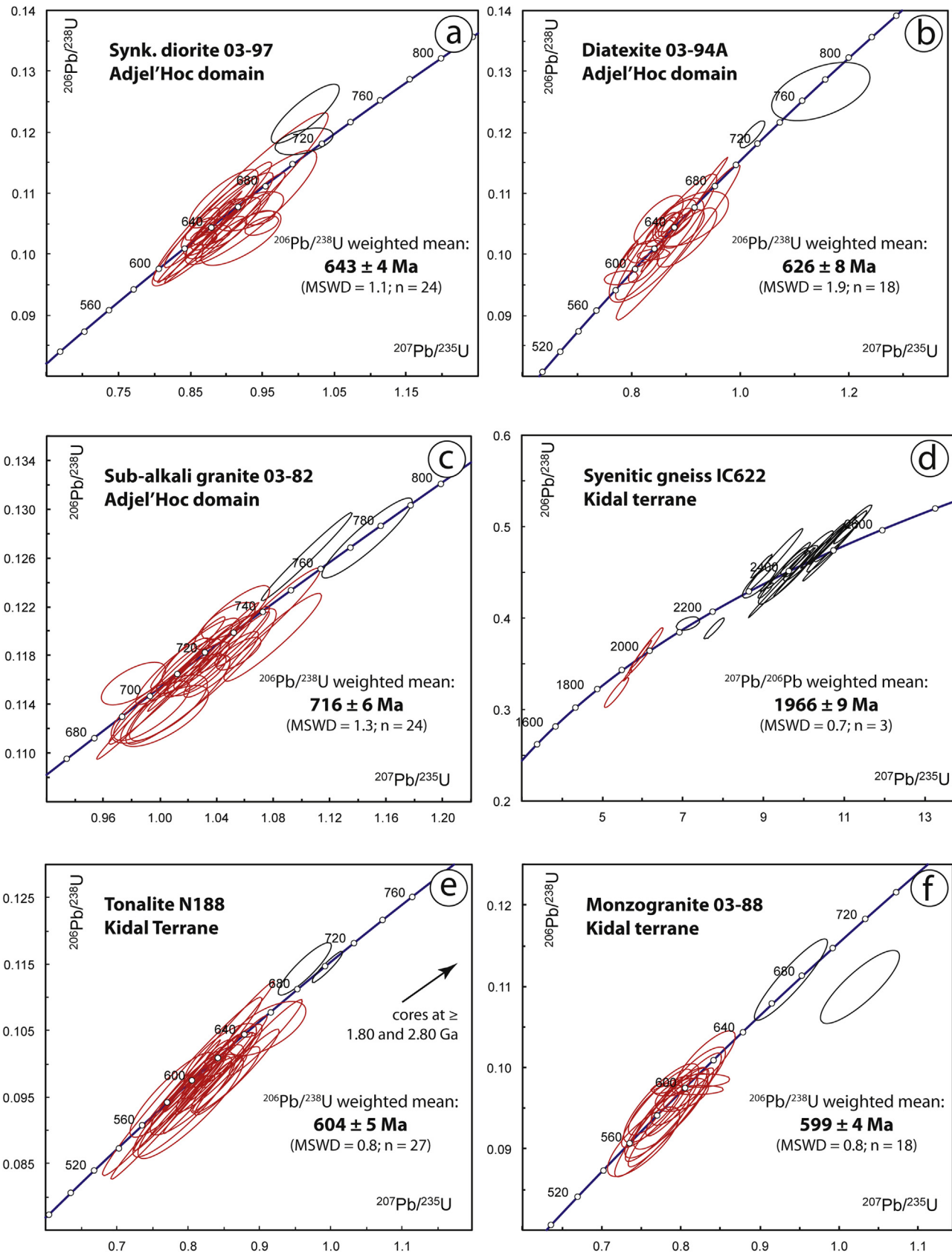


Fig. 6. U-Pb Concordia diagrams for rocks of the Adrar des Iforas. Ellipses are  $1\sigma$  error.

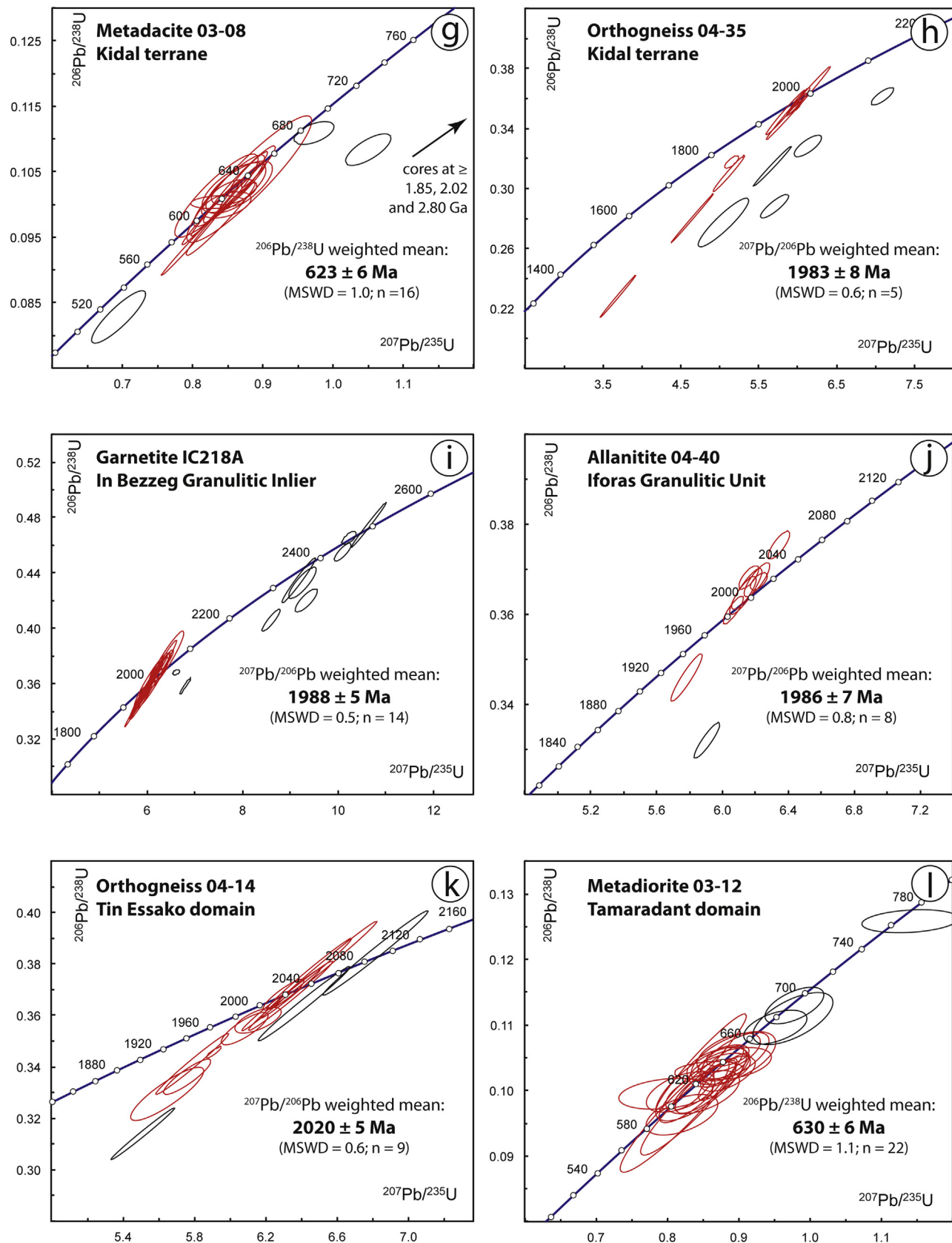


Fig. 6. (Continued)

Two cores, #19 and #22, are concordant at  $678 \pm 16$  Ma ( $2\sigma$ ) and  $2797 \pm 18$  Ma ( $2\sigma$ ). Two other cores are discordant but yield apparent ages (projected through 622 Ma) of 1850 Ma (#21) and 2020 Ma (#20).

#### 4.2.5. Migmatitic orthogneiss 04-35

Zircons from the orthogneiss are elongated with subhedral to rounded shapes and oscillatory zoning. Cores have been observed in the central part of the grains, surrounded by zoned domains (Fig. 5g). The analyses of zoned domains ( $n=9$ ) are aligned along a discordia line (Fig. 6h) that yields intercepts of  $1982 \pm 8$  Ma and  $222 \pm 71$  Ma (MSWD = 1.8). The lower intercept, although the result of a long extrapolation, is different from 0 Ma, which suggests non-zero Pb losses. The upper intercept is in agreement with the  $^{207}\text{Pb}/^{206}\text{Pb}$  weighted mean age of the most concordant analyses (see Table 1), which is  $1983 \pm 8$  Ma (MSWD = 0.6;  $n=5$ ). The latter is adopted as our best estimate for crystallization of the magmatic zircon in the protolith of the orthogneiss. Other analyses are markedly displaced to the right of the discordia line, but none is concordant and thus they provide only minimum ages for the inherited component(s). The oldest ages are  $2270 \pm 46$  Ma and  $2255 \pm 36$  Ma ( $2\sigma$ ) (#13 and #14).

#### 4.3. Iforas Granulitic Unit and In Bezzeg Granulitic inlier

##### 4.3.1. Garnetite IC218A (In Bezzeg)

Analyzed zircon grains have rounded shapes, sometimes with a multifaceted appearance (Fig. 5h), which is similar to metamorphic zircons from high-grade rocks (Vavra et al., 1999). Reported in the Concordia diagram (Fig. 6i) the data points broadly define two groups of concordant to slightly discordant analyses. The youngest analyses ( $n=14$ ) plot concordantly at around 2 Ga. This population includes low Th/U grains (Th/U ranging from 0.06 to 0.11), but also grains with high Th/U ratios (from 0.24 to 1.10). The formers are consistent with zircons grown in the solid-state (e.g. Williams and Claesson, 1987) or recrystallized under metamorphic conditions (Pidgeon, 1992). The laters, on the contrary are typically observed for magmatic zircons. The range of Th/U ratios for this population can thus reflect either an incomplete recrystallization of protolith zircons or that metamorphic zircon growth was influenced by local chemical conditions related to the breakdown or syncrystallisation of phases fractionating Th and/or U (e.g. Dhuime et al., 2007; Stepanov et al., 2012). The high degree of concordance and tight grouping of this zircon population do not support incomplete recrystallization processes, and we favor the hypothesis that the analyzed zircons were grown under metamorphic conditions and registered local chemical heterogeneities. This batch of zircon provides a  $^{207}\text{Pb}/^{206}\text{Pb}$  weighted mean age of  $1988 \pm 5$  Ma (MSWD = 0.5) interpreted as dating high-grade metamorphism. Other analyses have ages broadly spanning from 2100 to 2483 Ma. One analysis is sub-concordant at  $2100 \pm 22$  Ma, whereas all others have ages ranging from  $2381 \pm 20$  Ma to  $2483 \pm 18$  Ma ( $2\sigma$ ). Given that the protolith is a sedimentary material, these ages are representative of source rocks delivering the detritus. It is striking to note that these source rocks have ages very similar to those of the inherited components in the syenitic gneiss IC622 (from 2308 to 2472 Ma for the main group). The deposition age of the original sedimentary material is bracketed by the age of metamorphism ( $1988 \pm 5$  Ma) and by that of the youngest concordant detrital grain #16 ( $2100 \pm 22$  Ma).

##### 4.3.2. Allanite 04-40

As mentioned in the paragraph 3 (§ Analytical method) we used the zircon standard G91500 to calibrate the U-Pb ratios of the analyzed allanite (e.g. Darling et al., 2012) (Fig. 4c). However, since matrix effects between different minerals can significantly affect

the calibration of the  $^{206}\text{Pb}/^{238}\text{U}$  ratio (e.g. Bruguier et al., 2001), we have reported the data points in a Concordia diagram (see Fig. 6j), but only the  $^{207}\text{Pb}/^{206}\text{Pb}$  ratios are considered and discussed in the following. Nine grains were analyzed and amongst them, eight provide consistent  $^{207}\text{Pb}/^{206}\text{Pb}$  apparent ages ranging from  $1974 \pm 18$  Ma to  $1998 \pm 18$  Ma ( $2\sigma$ ). One analysis yields an older age of  $2085 \pm 16$  Ma ( $2\sigma$ ) (#10), which may reflect the preservation of an early allanite population. The eight analyses with consistent apparent ages provide a  $^{207}\text{Pb}/^{206}\text{Pb}$  weighted mean of  $1986 \pm 7$  Ma, which is adopted as our best estimate for the metamorphic growth of allanite. Since allanite as a high closure temperature for Pb ( $\geq 700$  °C after Oberli et al., 2004), this age is related to high-grade metamorphism. In addition, this age is similar within errors to that provided by metamorphic zircons in the garnet-bearing quartzite from In Bezzeg.

#### 4.4. Tamaradant – Tin Essako – Tin Zawatene domains

##### 4.4.1. Tin Essako orthogneiss 04-14

Zircons from the Tin Essako orthogneiss have euhedral shapes and under SEM imaging display oscillatory zoned domains (Fig. 5i). Some cores have been observed. In the Concordia diagram, most analyses fall on a chord (MSWD = 0.4) with an upper intercept of  $2022 \pm 7$  Ma and a lower intersection slightly different from 0 Ma ( $282 \pm 230$  Ma) (Fig. 6k), suggesting the grains have undergone weak ancient disturbances. Our best estimate for the age of emplacement of the protolith of the orthogneiss is given by the  $^{207}\text{Pb}/^{206}\text{Pb}$  weighted mean of the most concordant analyses, which is  $2020 \pm 5$  Ma (MSWD = 0.6;  $n=9$ ). Three analyses display older apparent ages (#9, #10, #13) and are interpreted as inherited from the source region of the magmas or as material assimilated during ascent. Two of these analyses, #9 and #10, are concordant at  $2066 \pm 18$  Ma and  $2079 \pm 18$  Ma ( $2\sigma$ ).

##### 4.4.2. Tamaradant Metadiorite 03-12

Zircons from the metadiorite are euhedral to subhedral with oscillatory zoned domains (Fig. 5j). Eighteen analyses performed on completely zoned grains and four analyses of zoned rims around cores plot concordantly and define a  $^{206}\text{Pb}/^{238}\text{U}$  weighted mean of  $630 \pm 6$  Ma (MSWD = 1.1) which is attributed to intrusion and crystallization of the dioritic magma (Fig. 6l). Five analyses of zircon cores, zoned or unzoned, are significantly older demonstrating that the diorite zircon population has a significant inherited component. These cores can be broken into three age groups. The most important group is constituted by three analyses with ages ranging from  $671 \pm 24$  Ma to  $690 \pm 26$  Ma ( $2\sigma$ ). These analyses may constitute a single population with a pooled age of  $679 \pm 16$  Ma or on the contrary may derive from different, unrelated, rocks. The inherited component in the diorite also includes one analysis concordant at  $764 \pm 16$  Ma ( $2\sigma$ ) (#23) and a discordant analysis with a minimum apparent age of  $2073 \pm 34$  Ma, or a more realistic projected age (through 630 Ma) of 2134 Ma.

#### 4.5. Major, trace elements and Sr-Nd isotopes

Ten samples (see Fig. 2 for location) have been studied for trace, major elements and Sr-Nd isotopes (Table 2).

Major elements have been reported in the AFM diagram and in the total alkalies versus silica diagram (TAS, Le Bas et al., 1986) (Fig. 7a and b). Metabasalts are characterized by very low SiO<sub>2</sub> content ranging from 43.8 to 51.4%. All samples belong to the subalkaline/tholeiite series and evolve from picropelitic to basaltic andesite (Fig. 7a). One basalt from the Kidal area, 04-45, is characterized by a very high MgO content (>20%). All samples from the Kidal terrane show a tholeiitic affinity in the AFM diagram whereas

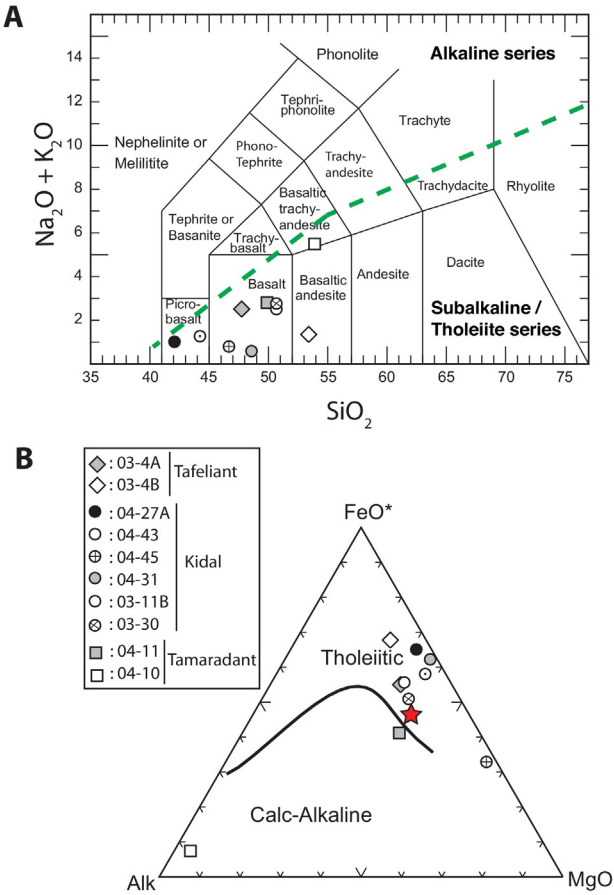


**Fig. 7.** (a) Total alkalies versus silica plot (TAS) for whole-rocks from the Adrar des Iforas, according to [Le Bas et al. \(1986\)](#); (b) AFM diagram after [Irvine and Baragar \(1971\)](#). Red star is MORB. (For interpretation of the references to color in this figure legend, the reader is referred to the web version of this article.)

the two samples from the Tamaradant area fall in the calc-alkaline field (Fig. 7b).

#### 4.5.1. Tafeliant area

The two metabasalts from the Tafeliant formation (03-04A and 03-04B) have a probable age bracketed between 696 Ma (the age of the oldest intrusive unconformably overlain by the sediments; [Caby and Andréopoulos-Renaud, 1985](#)) and 622 Ma (the age of the metadacite intruding the sedimentary formation, this study). They yield REE chondrite-normalized patterns characterized by high ( $\text{La}/\text{Yb}$ )<sub>N</sub> ratios (i.e. 3.0) typical of E-MORB (Table 2 and Fig. 8). They significantly differ from OIB by showing no systematic LILE (Cs-Rb) and HFSE (Nb-Ta) enrichment. On the contrary, the global MORB normalized patterns show a slight depletion in Nb-Ta combined with a slight (03-4A) or patent (03-4B) Zr-Hf negative anomaly (Fig. 8). Reported in the Nb/Yb versus Th/Yb diagram of [Pearce and Peate \(1995\)](#), they plot slightly outside the mantle array close to the E-MORB domain (Fig. 9). These characteristics suggest a subduction-related setting and more precisely a back-arc environment. Sr and Nd isotopic ratios have been corrected at 660 Ma. The two metabasalts have positive  $\varepsilon\text{Nd}_i$  (+5.2 and +5.3) combined with relatively low initial Sr isotopic ratios (0.70348 and 0.70312) suggesting an origin from a depleted mantle source. However, the Nd values are not typical of an unmodified DM mantle (i.e.  $\varepsilon\text{Nd}_i$  close to +9) suggesting mixing processes involving a continental contribution. Nd  $T_{\text{DM}}$  model ages of 935 and 943 Ma (Table 2) are similar for the two samples and are significantly older than their inferred age of emplacement.

#### 4.5.2. Kidal terrane

The four mafic samples collected west of the IGU belong to the Mesoproterozoic sequence and have been assigned an age of c. 1.0 Ga although no absolute age is available for this sequence (see § 2.1. Kidal domain). These samples (2 meta-basalts and 2 amphibolites) have roughly a similar flat pattern (see Fig. 8) with REE contents ranging from 7 to 20 times the chondritic value. Samples 04-43 and 04-45 show a slight LREE/MREE depletion ( $\text{La}/\text{Sm}_N < 0.85$ ) resembling N-MORB ([Arevalo and McDonough, 2010](#)), not observed in samples 03-11B and 03-30 ( $\text{La}/\text{Sm}_N > 1$ ). In the global MORB normalized diagram these samples display Zr-Hf negative anomalies, with no concomitant Nb-Ta negative anomaly except for sample 03-11B. The Nb/Ta ratios, ranging from 14.7 to 16.5, are close to the MORB source region (c.  $15.5 \pm 3.2$  after [Arevalo and McDonough, 2010](#)), except again sample 03-11B, which yields a significantly higher value of 18.8 (see Table 2).

Samples 04-27A and 04-31, collected north and northeast of the IGU, are related to the 1.8 Ga sequence. They show significantly more enriched REE patterns ( $30-75 \times \text{CHUR}$ ), characterized by high  $\text{La}/\text{Yb}_N$  ratios ( $> 1.3$ ). These two samples have contrasting LREE patterns. Indeed, sample 04-31 shows a significantly more depleted LREE pattern and a marked Eu negative anomaly suggesting plagioclase fractionation processes (Fig. 8).

Sr and Nd isotopic compositions of the studied samples clearly display two types of isotopic signatures.

- Samples west of the IGU are characterized by positive  $\varepsilon\text{Nd}_i$  values higher than +5.5 indicating a DM mantle origin, except sample 03-11B which yields a lower value of +3.6 suggesting mixing processes between a mantle component and a continental crust derived material (Table 2). The initial Sr isotopic signatures are slightly positive (from 0 to +27) in good agreement with the Nd results. Nevertheless, deviation from typical Sr mantle signature (i.e. -22) can reflect late hydrothermal alteration processes. The +27  $\varepsilon\text{Sr}$  value measured for sample 03-11B again argues for a more pronounced contribution of a continental component.

- Samples 04-27A and 04-31 show initial Sr and Nd values significantly different from the samples collected west of the IGU. They display  $\varepsilon\text{Sr}$  and  $\varepsilon\text{Nd}$  characterized by highly positive (+236 and +502) and negative (-2.5 and -2.1) values respectively (Table 2). Such high  $\varepsilon\text{Sr}$  values have been previously measured for the Iforas granulites, which provided  $^{87}\text{Sr}/^{86}\text{Sr}$  ratios up to 0.769 at 600 Ma ([Liégeois et al., 1987](#)). Sample 04-27A, yields a  $T_{\text{DM}}$  Nd model age of 1986 Ma, similar to the U-Pb crystallization age obtained for the neighboring orthogneiss 04-35 ( $1983 \pm 8$  Ma) or to the age of high grade metamorphism (1986–1988 Ma) at In Bezzeg (garnetite IC218A) and in the IGU (allanite 04-40) respectively.

#### 4.5.3. Tamaradant area

The studied samples (04-10 and 04-11) have been collected close to the boundary between the Tamaradant and the Tin Essako domains, west of the Adrar fault. The REE patterns of the samples are LREE enriched ( $\text{La}/\text{Yb}_N$  ratios of 11.1 and 3.0 for 04-10 and 04-11, respectively see Fig. 8) and characterized by a marked positive Eu anomaly indicating a cumulative component. In the global MORB normalized diagram, both samples exhibit pronounced positive Ba, Pb and Sr spikes in good agreement with the presence of plagioclase and supporting a cumulative origin. The patterns are characterized by Nb-Ta and Zr-Hf negative anomalies, a feature commonly attributed to a subduction-related environment. As no precise time constraints are available for these rocks, the  $\varepsilon\text{Sr}$  and  $\varepsilon\text{Nd}$  value have been recalculated at 1800 Ma, 1000 Ma and 660 Ma considering that these three periods correspond to the main events identified in the Adrar des Iforas (Table 2). These ratios, whatever the age correction, differ from a typical depleted mantle

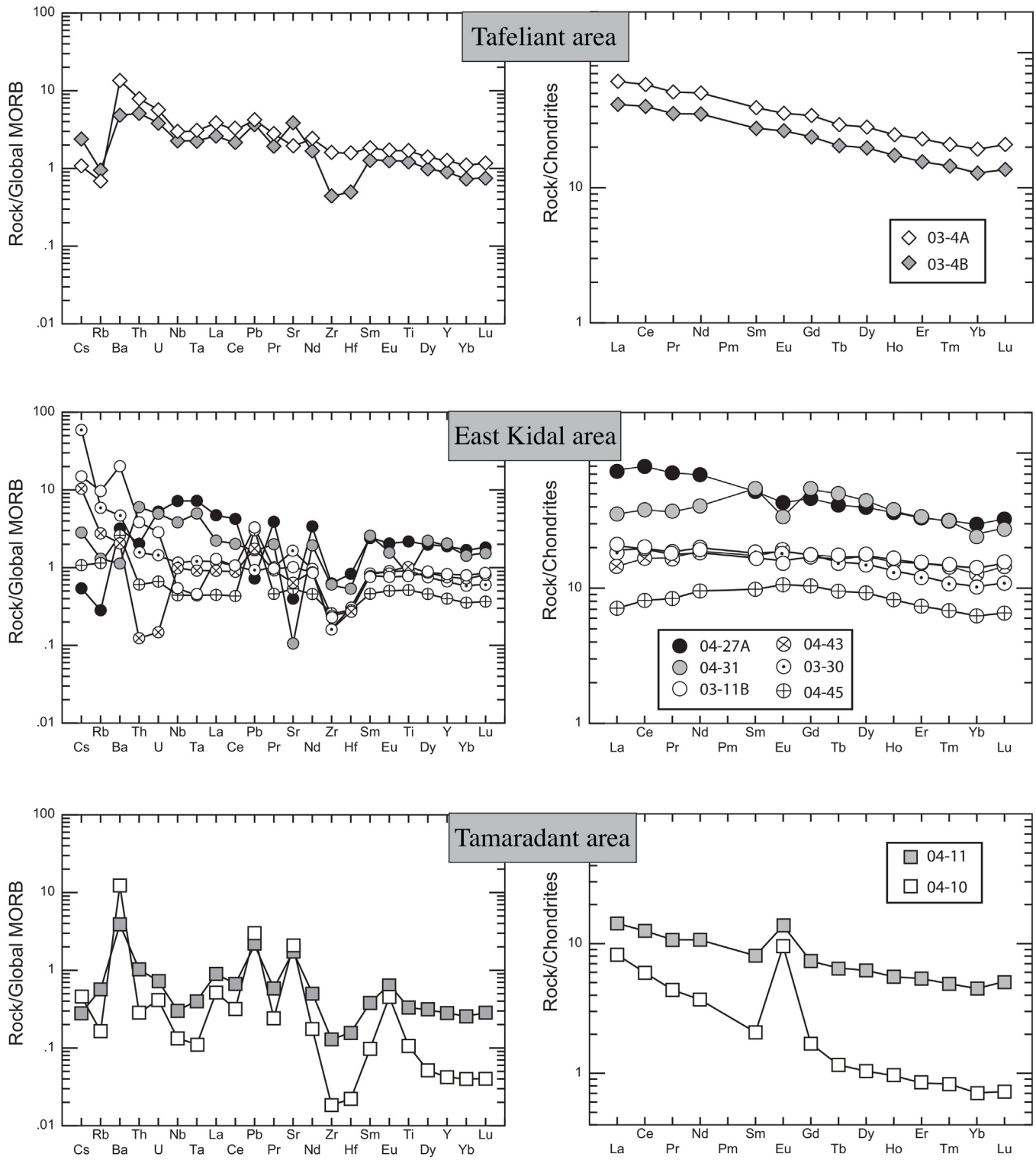


**Fig. 8.** (a-c) Trace-element analyses of metabasic samples from the various domains of the Adrar des Iforas normalized to Global MORB; (d-f) Rare earth element patterns normalized to chondrites. Normalizing values after [Arevalo and McDonough \(2010\)](#) and [McDonough and Sun \(1995\)](#) respectively.

reservoir and indicate involvement of a continental crust material. The  $Nd_{TDM}$  model ages of the two samples are 1832 and 1774 Ma. 1.8–1.7 Ga corresponds to a period of continental rifting recognized in the western part of the Tuareg Shield and in the studied area around Tin Elor ([Caby and Andreopoulos-Renaud, 1983](#)), which is difficult to reconcile with the subduction geochemical signatures of the two studied samples. The same holds true if these two samples

are related to the c. 1.0 Ga rifting period (development and deposition of a passive margin sequence), which is not compatible with a subduction related environment. We thereby consider that the  $Nd_{TDM}$  model ages of these samples have no geological meaning and result from mixing between an old Paleoproterozoic component and a juvenile Pan-African mantle related to a subduction environment.

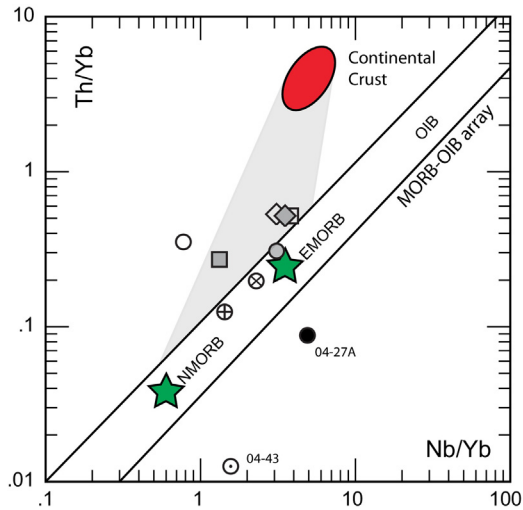


**Fig. 9.** Nb/Yb versus Th/Yb diagram from Pearce (2008). Stars are N-MORB and E-MORB. Continental crust is from Rudnick and Fountain (1995). The gray domain illustrates mixing between a mantle and a continental crust component (Pearce and Peate, 1995).

## 5. Discussion

### 5.1. Paleoproterozoic events and possible relationships between the different domains

The new geochronological data have identified Paleoproterozoic units in the three crustal domains investigated in this study. Basement rocks from the Kidal domain include, west of the IGU, a syenitic gneiss dated at  $1966 \pm 9$  Ma, and, in the Tin Elor area, northeast of the IGU, a migmatitic orthogneiss dated at  $1982 \pm 3$  Ma. East of the IGU, the Tin Essako orthogneiss is dated at  $2020 \pm 5$  Ma. Although these ages are distinct within error margins, they substantiate the occurrence of Paleoproterozoic rocks, with similar ages in the basement of the Central and Eastern Iforas domains, i.e. on both side of the IGU. The age range for rocks dated in this study (1960–2020 Ma) is typical of late- to post-Eburnean magmatism in the WAC (Abouchami et al., 1990; Boher et al., 1992). In the studied Paleoproterozoic intrusions, inherited components yield Eburnean (2.0–2.3 Ga) to Early Paleoproterozoic (2.3–2.5 Ga) ages. These include ages in the range 2070–2080 Ma (Orthogneiss 04-14), 2110 Ma (Syenitic gneiss IC622), >2270 Ma (Orthogneiss 04-35) and 2300–2480 Ma (Syenitic gneiss IC622). Only one inherited Archean grain ( $2798 \pm 18$  Ma) has been identified in the 622 Ma-old Tafeliant metadacite. These Paleoproterozoic inherited components reflect partial melting or assimilation of deep-seated basement source rocks or of (meta)sedimentary material. In the latter case these inherited components do not necessarily constitute part of the basement units but can reflect an extraneous addition related to a sedimentary transfer from eroded source rocks that can have been located outside of the considered domains. However, the euhedral shape and oscillatory zoning of some cores indicate a magmatic origin, and/or a short sedimentary transport. As mentioned before the range of ages observed is consistent with events known in the Paleoproterozoic WAC (Abouchami et al., 1990; Boher et al., 1992). Ages between 2.3 and 2.5 Ga however are not known in the Paleoproterozoic portion of the WAC, for which the oldest ages are around 2.3 Ga (Tshibududze et al., 2013). This confirms that the Adrar des Iforas constituted a distinct lithospheric block to the WAC characterized by a Late Archean/Early Proterozoic evolution.

The age of granulite-facies metamorphism in the In Bezzeg inlier is dated at  $1988 \pm 5$  Ma ( $2\sigma$ ) on metamorphic zircons, which is the same within error as the age reported for metamorphic allanite

in the IGU at  $1986 \pm 7$  Ma ( $2\sigma$ ). Interestingly these ages are significantly different from the age of high-grade metamorphism (c. 2120 Ma) as proposed by Lancelot et al. (1983) for the IGU. However these authors based their conclusions on the U-Pb zircon age of a leptynite ( $2120 \pm 7$  Ma) mylonitised during a late Pan-African event dated at  $566 \pm 8$  Ma. Another leptynite gave an upper intercept age of  $2434 \pm 6$  Ma, interpreted by these authors as unrelated to any geological event, in spite of a convincing alignment (see Fig. 6 of Lancelot et al., 1983). We argue that the ages presented by these authors ( $2120 \pm 7$  Ma and  $2434 \pm 6$  Ma) are related to the magmatic crystallization of the protolith of the leptynites in the basement of the IGU, rather than to the granulite facies metamorphism. Strikingly, the age of the detrital zircons in the garnetite from In Bezzeg (c. 2100 and 2380–2480 Ma) is consistent with that of the leptynites from the IGU (2120 and 2434 Ma). The similar age of metamorphism at around 1985–1990 Ma, as determined in this study, pleads for the proposal that the IGU and the In Bezzeg inlier once formed a single granulitic basement that was subsequently fragmented. Inherited components in the Kidal syenitic gneiss are c. 2100 and 2300–2470 Ma old and reflect the ages of deep-seated crustal rocks constituting the basement of the Kidal terrane sampled by the syenitic magma. The age range of these inherited components is identical to the ages of both the detrital zircons at In Bezzeg and of leptynites from the IGU. This indicates that basement rocks in the three units have undergone a synchronous Paleoproterozoic evolution and thereby constituted a single continental landmass at the end of the Paleoproterozoic. The granulitic outcrops of the IGU and In Bezzeg would then represent the deepest crustal levels of this terrane, whereas the Kidal domain exposes shallower levels.

In addition, the age of high-grade metamorphism at In Bezzeg and in the IGU (1985–1990 Ma, this study) is slightly younger or within errors of ages obtained for magmatic and metamorphic events in the IOGU. In this area the UHT granulite facies metamorphism has been dated by Peucat et al. (1996) between  $1983 \pm 15$  Ma and  $2002 \pm 14$  Ma ( $2\sigma$ ). This range of ages encompasses the emplacement of charnockites and granites at c. 2000 Ma (Haddoum et al., 1994), and the emplacement of carbonatites at  $1994 \pm 14$  Ma (Bernard-Griffiths et al., 1988). This similarity indicates that the granulite facies metamorphic event was coeval in the IOGU and IGU, or suggests a slight diachronism, with granulite facies metamorphism younging southward. This observation strengthens the view that the IGU and IOGU are two equivalent granulitic crustal segments (Boullier et al., 1978; Black et al., 1994). The main difference between both units is related to the occurrence of Archean components in the IOGU (Lancelot et al., 1976; Haddoum et al., 1994; Peucat et al., 1996) that have not been identified yet in the IGU. The latter however has not been the subject of numerous geochronological studies as is the case for IOGU, and the lack of Archean rocks may be related to the weak geochronological dataset available for this unit. A second difference is related to the influence of the magmatic and metamorphic Pan-African events that affected the granulitic units of the IGU, but which are not present in the IOGU, apart along the East In-Ouzzal Shear Zone (e.g. Ferkous and Monié, 2002). Using the  $^{40}\text{Ar}/^{39}\text{Ar}$  method, the cooling age of high-temperature biotite armored in garnet of IOGU granulites is  $1775 \pm 25$  Ma (Maluski et al., 1990). The same method has given an age of  $1830 \pm 5$  Ma on a phlogopite from a 2.0 Ga-old carbonatite, but the age was interpreted as a minimum value owing to a diffusion profile in the studied crystal (Ferkous and Monié, 2002). However, it is significant to notice that the synrift sub-alkaline intrusions dated at  $1837 \pm 17/19$  Ma in the northern part of the Tamaradant domain and  $1755 \pm 10$  Ma along the IOGU (Caby and Andreopoulos-Renaud, 1983) are comparable to cooling of IOGU granulites below  $300^\circ\text{C}$  (Maluski et al., 1990). This event at c. 1.8 Ga has been interpreted as reflecting a Statherian rifting event and indicates that unroofing and exhumation of granulites of

the IOGU/IGU crustal block occurred at that time. In this scenario, the c. 800 km long IOGU/IGU granulitic outcrops represent the deep crust exhumed during the Statherian rifting.

Samples 04-27A and 04-31 collected north and east of the IGU have geochemical signatures and Nd model ages that help deciphering the geotectonic setting of this period. However, before using these geochemical constraints, possible contamination, in the source of the magma, during their ascent through the crust or their final emplacement should be evaluated. In Fig. 9 these two samples plot either in the MORB-OIB array (04-31) or slightly below (04-27A). The location of sample 04-27A can be attributed to mineral fractionation where the high amount of garnet accounts for the high Yb content and preferentially decreases the Th/Yb of the bulk rock. The  $T_{DM}$  Nd model age of sample 04-27A is 1986 Ma which is very close to the age of basement rocks from the Kidal domain or from the age of high-grade granulitic metamorphism in the IGU and at In Bezzeg. The  $\varepsilon_{Nd}$  value calculated at 1.8 Ga is +2.5 for 04-27A, which indicates derivation mainly from a mantle reservoir but with a slight contribution of continental crust material. This is corroborated by the high  $^{87}\text{Sr}/^{86}\text{Sr}$  (0.71969 at 1.8 Ga) value of this sample. It is noteworthy that the Iforas granulites display similar isotopic signatures (>0.710 and up to 0.769 for  $^{87}\text{Sr}/^{86}\text{Sr}_i$ ; Liégeois et al., 1987), whereas the rocks from the Kidal assemblage have  $^{87}\text{Sr}/^{86}\text{Sr}_i$  lower than 0.710 (Liégeois et al., 1987). Similarly, sample 04-31 yields a very high  $^{87}\text{Sr}/^{86}\text{Sr}_i$  value (0.73392), combined with a negative  $\varepsilon_{Nd}$  value (-9.3). The two studied samples are thus attributed to a Paleoproterozoic lower crustal basement component.

## 5.2. Late Mesoproterozoic/Early Neoproterozoic events

Metabasalts collected west of the IGU, in the passive margin assemblages, plot in the MORB-OIB array of Fig. 9 (samples 03-30 and 04-45), below (04-43) or above (03-11B). The  $\varepsilon_{Nd}$  values of samples 03-30, 04-45 and 04-43 (ranging from 5.6 to 6.5) and low  $^{87}\text{Sr}/^{86}\text{Sr}_i$  (from 0.70334 to 0.70348 corrected at 1.0 Ga) reflect a DM origin without significant contribution of a continental crust material. Sample 03-11B shows Sr and Nd signatures slightly different (0.70522 and +3.6, respectively) interpreted as a crustal contamination in good agreement with its location, away from the MORB-OIB array in Fig. 9. It is postulated here that this late Mesoproterozoic/early Neoproterozoic event represents a renewed intracontinental rifting, whose remnants are still preserved on both sides of the IGU (see Fig. 2). Such an evolution is typical of intracontinental extended crustal domains, such as for example the Espinhaço basin, within the São Francisco Craton in Brazil which formed at the same period (1.7–1.8 Ga) and that was subsequently submitted to several stages of rifting, from 1.5 to 0.8 Ga (see for example Danderfer et al., 2009). From a geodynamic point of view, it is likely that the late Mesoproterozoic/early Neoproterozoic rifting event correlates with the break-up of Rodinia, and can be considered as a prefiguration of crustal thinning and spreading that ultimately ended in the opening of the Pharusian Ocean, east of the WAC. Available geochronological data obtained on mafic complexes exposed along the main Pan-African suture show that the oceanic crust of the Pharusian ocean should be older than 800 Ma, since the oldest preserved intra-oceanic arcs formed in the Pharusian Ocean have ages around 800 Ma. These include the Bou Azzer ophiolitic gabbro (795 Ma after El Hadi et al., 2010) and the Amalaoulaou arc gabbro (793 Ma after de la Boisse, 1981 recalculated in Berger et al., 2011). Whether this Tonian rifting phase led to the formation of an oceanic basin in the Adrar des Iforas area or on the contrary aborted, is under debate as this will have important implications in term of continental fragmentation and formation of distinct terranes between the Kidal terrane and the IGU. The preservation of passive margin-type sequences covering

all these domains and the lack of high pressure rocks suggest that the Kidal terrane on one hand and the IGU and In Bezzeg granulitic units on the other hand were still forming a single crustal unit at about 1.0 Ga.

## 5.3. Neoproterozoic events

Neoproterozoic ages have been obtained in the Tilemsi/Adjel'Hoc terrane and in the Kidal terrane and Tamaradant domain. The oldest Neoproterozoic age is from a porphyroid sub-alkali gneissic granite in the eastern part of the Tilemsi/Adjel'Hoc oceanic terrane, which is dated at  $716 \pm 6$  Ma. This age correlates with build-up of the intra-oceanic Tilemsi island arc (730–710 Ma after Caby et al., 1989). It is also comparable to the 696 Ma old Kidal metaquartz diorite (Caby and Andréopoulos-Renaud, 1985), which reflects arc-related magmatism and formation of an Andean-type margin along the western edge of the Kidal terrane. Subduction related processes thus already existed at that time in the Pharusian realm, offshore of the WAC. This implies the occurrence of two coexisting subduction zones, one under the Tilemsi arc (intra-oceanic) and a second under the Kidal margin (ocean-continent) as already proposed by Liégeois et al. (1987). The oldest evidence for magmatic activity in the Tilemsi arc is from a 726 Ma-old quartz diorite (Caby et al., 1989). The diorite 03-97 dated in this study at  $643 \pm 4$  Ma, is the youngest dated material in the Tilemsi/Adjel'Hoc terrane and indicates that magma production lasted until c. 640 Ma, which represents a minimum lifetime for the arc of c. 80 Ma. Inherited components identified in the diorite ( $748 \pm 46$  Ma and  $722 \pm 20$  Ma) may reflect intra-arc cannibalization of older arc rocks, but their age is too imprecise to provide accurate constraints. The estimated lifetime for the Tilemsi oceanic island arc is similar to that of the broadly contemporaneous Amalaoulaou intra-oceanic arc, which has a lifetime of 90–130 Ma (Berger et al., 2011). Interestingly this is significantly longer than the estimated lifetime (c. 50 Ma) of typical intra-oceanic island arc, such as the Jurassic Talkeetna and Cretaceous Kohistan arcs (Garrido et al., 2007; Dhuime et al., 2009; Rioux et al., 2010; Boschet et al., 2011). If similar processes and crustal growth rates are assumed between fossil and present day island arcs (see for example Dimalanta et al., 2002), this suggests that the Cryogenian period was characterized by accretion of important volumes of juvenile crust in arc setting, as exemplified for the Arabo-Nubian Shield (Ali et al., 2009; Stern and Johnson, 2010). The 643 Ma-old age also constitutes a maximum limit for docking of the arc to the Kidal terrane. This is consistent with the c. 630 Ma age of deposition of active-margin volcanosedimentary units in the western part of the Kidal terrane, which are intruded by pre-tectonic granodioritic plutons, one of which was dated at  $635 \pm 5$  Ma close to the Tessalit-Anefif shear zone (Caby et al., 1989). This indicates that subduction below the Kidal margin lasted until c. 630 Ma. Low Th/U zircon grains from the diatexite 03-94A reflect partial melting affecting arc protoliths at  $626 \pm 8$  Ma, which we relate to the age of collision between the Tilemsi arc and the Kidal terrane. To the south, turbiditic volcanic greywackes and pillow basalts of the Tafeliant Group were deposited after 696 Ma (Caby and Andréopoulos-Renaud, 1985). Geochemical constraints of metabasalts from the Tafeliant Group are consistent with a back-arc environment. In this area, the sediments are intruded by a metadacitic dyke dated at  $623 \pm 6$  Ma, indicating that development of this back-arc basin occurred between 696 and 620 Ma. It is worth noting that a similar back-arc environment has been previously proposed by Leterrier and Bertrand (1986) for ultrabasites to gabbros and anorthosites located east of the IGU. Further south, the metadiorite from the Tamaradant domain yields an age of  $630 \pm 6$  Ma. The two samples (04-10 and 04-11) from the Tamaradant domain yield geochemical signatures consistent with a subduction context (LILE enrichment and HFSE depletion). They

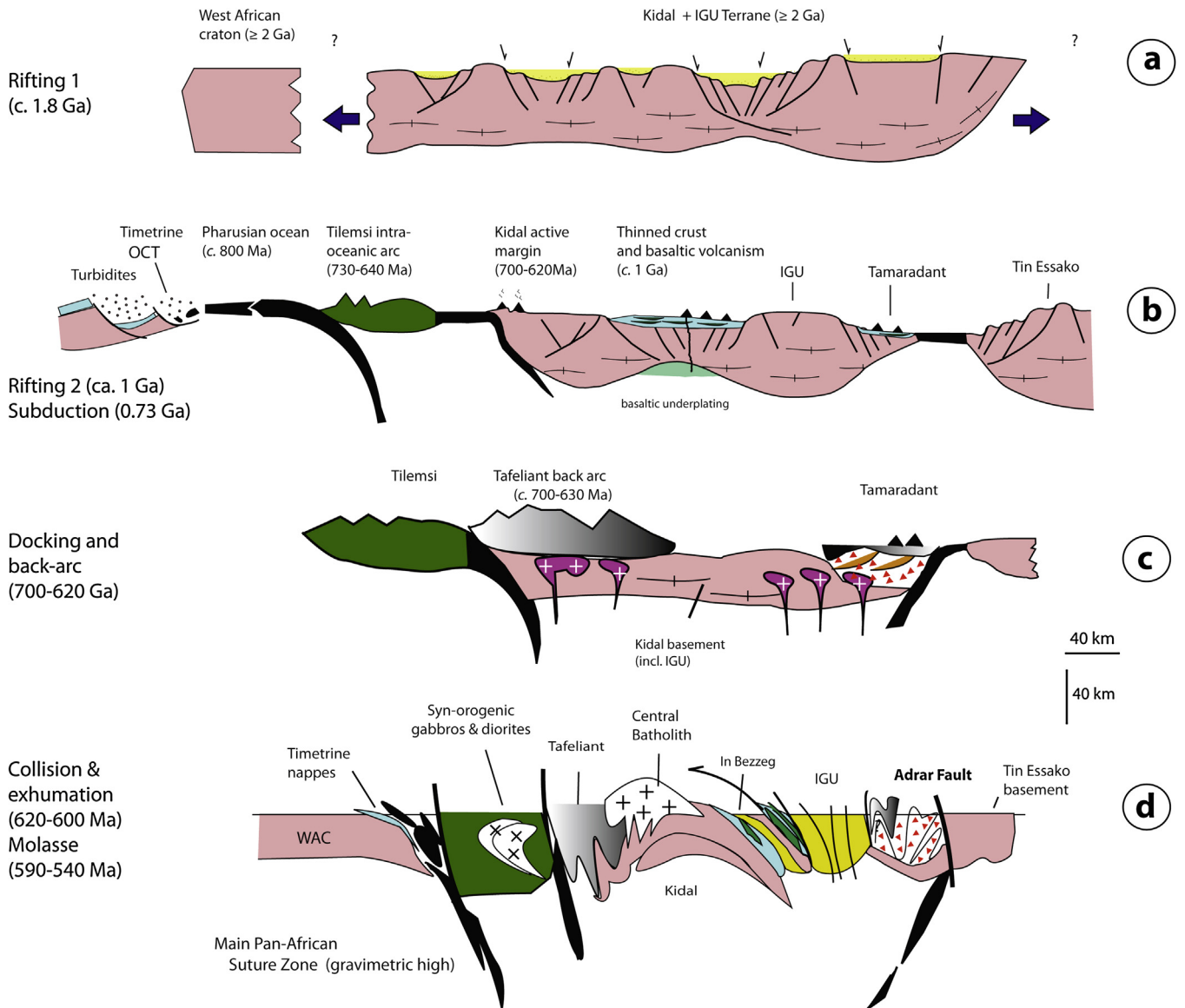


**Fig. 10.** Schematic evolutionary diagram for the Adrar des Iforas from 1.8 Ga to 540 Ma. (a) Stage 1: Statherian rifting responsible for the exhumation of the 1.98 Ga granulitic lower crust and deposition of detrital sediments (quartzites); (b) Stage 2: Second rifting event at c. 1.0 Ga that affected the Kidal/IGU terrane. This stage is characterized by rift-related sedimentation and intraplate basaltic volcanism on both sides of the IGU. Further west this extensional period resulted in the opening of the Pharusian Ocean (>800 Ma). It is postulated that an oceanic basin also formed east of the IGU, separating the latter from the Tin Essako domain, although this basin could have opened earlier, during Stage 1. Subduction of the Pharusian Ocean started at 0.73 Ga or earlier, allowing the development of the Tilemsi intra-oceanic arc and the Kidal active margin at 0.70 Ga; (c) development of a back-arc basin (Tafeliant Group) occurred between 700 and 620 Ma, possibly synchronous with subduction in the Tamaradant area. Docking of the Tilemsi arc took place at c. 630 Ma; (d) collision with the eastern margin of the WAC occurred between 620 and 600 Ma and was shortly followed by post-collisional processes.

show negative  $\epsilon Nd_i$  values ( $-8.9$  and  $-2.5$  at 660 Ma) and plot outside the MORB-OIB array in Fig. 9. Although the  $Nd_{TDM}$  model ages are consistent at 1.8 Ga they are taken as reflecting contamination by a Paleoproterozoic (or older) crustal basement. These geochemical characteristics, combined with the 630 Ma age of the intrusive metadiorite, document the development of a subduction zone, east of the IGU, probably delimited by the Adrar fault.

The ages at around 620–630 Ma are coeval with exhumation of HP rocks further north in the Tassendjanet terrane (Berger et al., 2014), thus suggesting a diachronous tectono-metamorphic and magmatic evolution between the Adrar des Iforas and the Tassendjanet terrane.

After collage, the Tilemsi arc became the active margin of the western edge of the Kidal terrane as subduction of the remains of

the Pharusian Ocean was still ongoing. In the Adrar des Iforas, collision between this active margin and the WAC is represented by the emplacement of syn-kinematic tonalite and granodiorite plutons, one of which was dated at  $620 \pm 10$  Ma (Caby and Andreopoulos-Renaud, 1989). The syn-collision foliated tonalite N188 indicates that collisional processes in the Adrar des Iforas propagated eastward and can be extended down to  $604 \pm 4$  Ma. Further South, in Gourma, UHP metamorphism of the passive margin of the West African craton took place at around 610 Ma (Ganade de Araujo et al., 2014), which is consistent with the timing of events depicted in the Adrar des Iforas. One component of the complex Central Iforas batholith (Liégeois et al., 1998) is dated at  $599 \pm 4$  Ma and defines the onset of the post-collisional events in the western Adrar des Iforas.

#### 5.4. Toward an evolutionary model

The ages reported in this study and the sequence of events depicted above allow us to propose a new geodynamic scenario for the Adrar des Iforas area (see Fig. 10). Because the different domains that constitute nowadays the Adrar des Iforas contains Paleoproterozoic basement units with comparable ages and inherited components, it is proposed that at 1.8–1.9 Ga, the Kidal terrane, the IGU and the Tamaradant domain constituted a single terrane. This terrane contains Late Archean/Early Paleoproterozoic units that are lacking in the WAC. We thus favor the hypothesis following which this terrane formed independently from the WAC, i.e. it did not represent a portion of the WAC that was subsequently fragmented. However this should be taken with caution since only very few geochronological data on the WAC, west of the Pan-African suture, are available. The IGU bears similarities with the IOGU and it is postulated that IOGU was also part of this terrane. IOGU and IGU most likely represent the deep crust of this terrane which was granulitised at around 1.98–2.0 Ga and exhumed during a Statherian episode of rifting, thus forming a c. 800 km long extended continental crust segment. This megarift was submitted to a new rifting episode at around 1 Ga, which we correlate with a global extensional regime that affected Rodinia at that time. Before this period, the relationships between this terrane and the WAC are not known (Fig. 10A). However, in the West African realm, this resulted in the creation of the Pharusian Ocean between the WAC and other crustal blocks, including the Adrar des Iforas. At around 800–750 Ma (the age of the oldest island arc crust preserved east of the WAC), this oceanic domain was subjected to subduction processes, which resulted in the creation of intra-oceanic island arcs, including the Amalaoulaou and Tilemsi arcs. This period also corresponds to a major period of island-arc activity, east of the Saharan metacraton and the accretion of juvenile crust now forming the bulk of the Arabo-Nubian Shield (Stern and Johnson, 2010). As early as 700 Ma a contemporaneous active margin also developed along the western edge of the Adrar des Iforas represented by the Kidal terrane (Fig. 10B). Docking of the Tilemsi island arc occurred at 620–630 Ma. This event was shortly followed by continental collision with the eastern passive margin of the WAC, which was subducted and underwent UHP metamorphism at around 610 Ma in the south. Post-collisional processes shortly followed at c. 600 Ma in the western Iforas, but eastward younging of intracontinental transpression along longitudinal domains and lateral motion of crustal blocks in the whole Tuareg Shield took place much later as shown by the Adrar fault molassic belt with greenschist facies metamorphic overprint. This period extended down to 540–520 Ma with deposition of molassic sediments and emplacement of alkaline ring complexes (Paquette et al., 1998).

## 6. Conclusions

The Adrar des Iforas registers the long-lived sequence of orogenic events that took place at different periods of time since the Paleoproterozoic to the Pan-African. Granulite facies metamorphism is dated at 1980–1990 Ma in the IGU and at In Bezzeg. The age of this event is similar to the age of HT granulite facies metamorphism affecting rocks of the In Ouzzal block, thus strengthening the view that these different granulitic outcrops have constituted a single coherent crustal block during the Paleoproterozoic. Worldwide, this period was synchronous to global scale collisional events that resulted in the formation of the supercontinent Columbia (Zhao et al., 2002). Following the granulite facies event, this block was submitted to a first phase of rifting at c. 1.8 Ga, during the Statherian period, which is characterized by anorogenic rhyolitic magmatism and the deposition of thick quartzite coeval with exhumation of the

lower crustal granulitic crust. In the Adrar des Iforas a renewed rifting period occurred at c. 1.0 Ga and is characterized by anorogenic basaltic extrusions and passive margin sedimentary deposits. In the Neoproterozoic, from 730 Ma, the Kidal terrane in the west became the active margin of the Adrar des Iforas due to the eastward subduction of the Pharusian Ocean. Arc related magmatic rocks also outcrop east of the IGU, in the Tamaradant area, which we relate to a coeval subduction, but with an opposite sense. The age of Neoproterozoic events in the different domains constituting the Adrar des Iforas is consistent, which indicates that they formed a coherent block. We conclude that, similarly to Central Hoggar whose different domains were grouped to form a single continental landmass (LATEA metacraton of Liégeois et al., 2003), the Adrar des Iforas (Kidal, IGU and Tamaradant domains) probably belonged to a single terrane until 1.0 Ga. This block may also include the In Ouzzal block in Algeria, which displays a similar Paleoproterozoic evolution. This terrane has been variably affected by the Pan-African orogeny and was dissected along shear zones, with differential movements of the different parts.

## Acknowledgement

The authors are grateful to the Direction Nationale de la Géologie et des Mines (Bamako) and to GEOTER for logistical support and facilities. We thank C. Nevado and D. Delmas for preparing thin sections and to F. Fernandez for SEM imaging. The authors are grateful to Jean-Paul Liégeois and Jérôme Gané whose comments significantly helped us improve the manuscript and to Yann Rolland for comments and editorial handling.

## References

- Abdelsalam, M.G., Liégeois, J.P., Stern, R.J., 2002. *The Saharan Metacraton*. *J. Afr. Earth Sci.* **34**, 119–136.
- Abouchami, W., Boher, M., Michard, A., Albarede, F., 1990. *A major 2.1 Ga old-event of mafic magmatism in West Africa: an early stage of crustal accretion*. *J. Geophys. Res.* **95**, 17605–17629.
- Ali, K.A., Stern, R.J., Mantona, W.I., Kimurab, J.I., Khameesc, A.H., 2009. *Geochemistry Nd isotopes and U-Pb SHRIMP zircon dating of Neoproterozoic volcanic rocks from the Central Eastern Desert of Egypt: new insights into the 750 Ma crust-forming event*. *Precambrian Res.* **171**, 1–22.
- Amard, B., 1983. *Découverte de microfossiles dans le Protérozoïque métamorphique de l'Adrar des Iforas (Mali): nouveaux éléments de datation de la "série à Stromatolites" en Afrique de l'Ouest*. *C. R. Acad. Sci. Paris* **296**, 85–90.
- Arevalo, R., McDonough, W.F., 2010. *Chemical variations and regional diversity observed in MORB*. *Chem. Geol.* **271**, 70–85.
- Berger, J., Caby, R., Liegeois, J.P., Mercier, J.C., Demaiffe, D., 2009. *Dehydration, melting and related garnet growth in the deep root of the Amalaoulaou Neoproterozoic magmatic arc (Gourma, NE Mali)*. *Geol. Mag.* **146**, 173–186.
- Berger, J., Caby, R., Liegeois, J.P., Mercier, J.C., Demaiffe, D., 2011. *Deep inside a neoproterozoic intra-oceanic arc: growth, differentiation and exhumation of the Amalaoulaou complex (Gourma, Mali)*. *Contrib. Mineral. Petroil.* **162**, 773–796.
- Berger, J., Ouzebane, K., Bendaoud, A., Liégeois, J.P., Kiéñast, J.R., Bruguier, O., Caby, R., 2014. *Continental subduction recorded by Neoproterozoic eclogite and garnet amphibolites from Western Hoggar (Tassendjanet terrane, Tuareg Shield, Algeria)*. *Precambrian Res.* **247**, 139–158.
- Bernard-Griffiths, J., Peucat, J.J., Fourcade, S., Kienast, J.R., 1988. *Origin and evolution of 2 Ga old carbonatite complex (Ihouaouene, Ahaggar Algeria): Nd and Sr isotopic evidence*. *Contrib. Mineral. Petroil.* **100**, 339–348.
- Bertrand, J.M., Dupuy, C., Dostal, J., Davison, I., 1984. *Geochemistry and geotectonic interpretation of granitoids from central Iforas (Mali W. Africa)*. *Precambrian Res.* **26**, 265–283.
- Black, R., Lameyre, J., Bonin, B., 1985. *The structural setting of alkaline complexes*. *J. Afr. Earth Sci.* **3**, 5–16.
- Black, R., Latouche, L., Liégeois, J.P., Caby, R., Bertrand, J.M., 1994. *Pan-African displaced terranes in the Tuareg shield (Central Sahara)*. *Geology* **22**, 641–644.
- de la Boissé, H., 1981. *Sur le métamorphisme du micaschiste éclogitique de Takamba (Mali) et ses conséquences paleogéodynamiques au Précambrien supérieur*. *C. R. Soc. Geol. Fr.* **3**, 97–100.
- Boher, M., Abouchami, W., Michard, A., Albarede, F., Arndt, N.T., 1992. *Crustal growth in West Africa at 2.1 Ga*. *J. Geophys. Res.* **97**, 345–369.
- Bosch, D., Bruguier, O., Pidgeon, R.T., 1996. *Evolution of an Archean metamorphic belt: a conventional and SHRIMP U-Pb study of accessory minerals from the Jimperding Metamorphic Belt, Yilgarn Craton, West Australia*. *J. Geol.* **104**, 695–711.

- Bosch, D., Garrido, C.J., Bruguier, O., Dhuime, B., Bodinier, J.L., Padron-Navarta, J.A., Galland, B., 2011. Building an island arc crustal section: time constraints from a LA-ICP-MS zircon study. *Earth Planet. Sci. Lett.* 309, 268–279.
- Boullier, A.M., 1979. Chariage et déformations de l'unité granulitique des Iforas au cours de l'orogenèse pan-africaine. *Rev. Geol. Dyn. Geograph. Phys.* 21, 377–382.
- Boullier, A.M., 1982. Etude structurale du centre de l'Adrar des Iforas (Mali). *Mylonites et tectogenèse*. Thesis, Institut National Polytechnique Lorraine, University of Nancy 1, France, 348 pp.
- Boullier, A.M., 1986. Sense of shear and displacement estimates in the Abeibara-Rharous late Pan-African shear zone (Adrar des Iforas Mali). *J. Struct. Geol.* 8, 47–58.
- Boullier, A.M., 1991. The Pan-African Trans-Saharan belt in the Hoggar shield (Algérie, Mali, Niger): a review. In: Dallmeyer, R.D., Lecorche, J.P. (Eds.), *The West African Orogens and Circum-Atlantic Correlatives*. IGCP, Special Publication. Springer Verlag, Berlin, pp. 85–105.
- Boullier, A.M., Barbey, P., 1988. A polycyclic two-stage corona growth in the Iforas Granulite Unit (Mali). *J. Met. Geol.* 6, 235–254.
- Boullier, A.M., Davison, I., Bertrand, J.M., Coward, M.P., 1978. L'unité granulitique des Iforas : une nappe de socle d'âge Pan-Africain précoce. *Bull. Soc. Géol. Fr.* XX, 877–882.
- Boullier, A.M., Liégeois, J.P., Black, R., Fabre, J., Sauvage, M., Bertrand, J.M., 1986. Late Pan-African tectonics marking the transition from subduction-related calc-alkaline magmatism to within-plate alkaline granitoids (Adrar des Iforas Mali). *Tectonophysics* 132, 233–246.
- Bruguier, O., Telouk, P., Cocherie, A., Fouillioc, A.M., Albaredo, F., 2001. Evaluation of Pb-Pb and U-Pb laser ablation ICP-MS zircon dating using matrix-matched calibration samples with a frequency quadrupled (266 nm) Nd:YAG laser. *Geostand. Newslett.* 25, 361–373.
- Bruguier, O., Hammor, D., Bosch, D., Caby, R., 2009. Miocene incorporation of peridotite into the Hercynian basement of the Maghrebides (Edough massif NE Algeria): implications for the geodynamic evolution of the Western Mediterranean. *Chem. Geol.* 261, 171–183.
- Caby, R., 1994. First record of Precambrian coesite from Northern Mali: implications for Late Proterozoic plate tectonics around the West African Craton. *Eur. J. Mineral.* 6, 235–244.
- Caby, R., 1996. A review of the In Ouzzal granulitic terrane (Tuareg shield, Algeria): its significance within the Pan-African Trans-Saharan belt. *J. Met. Geol.* 14, 659–666.
- Caby, R., 2003. Terrane assembly and geodynamic evolution of Central-Western Hoggar: a synthesis. *J. Afr. Earth Sci.* 37, 133–159.
- Caby, R., Andreopoulos-Renaud, U., 1983. Âge à 1800 Ma du magmatisme sub-alkalin associé aux métasédiments monocycliques dans la chaîne pan-Africaine du Sahara central. *J. Afr. Earth Sci.* 1, 193–197.
- Caby, R., Andréopoulos-Renaud, U., 1985. Étude pétrostructurelle et géochronologie U/Pb sur zircon d'une métadiorite quartzique de la chaîne pan-africaine de l'Adrar des Iforas (Mali). *Bull. Soc. Géol. Fr.* 8, 899–903.
- Caby, R., Andreopoulos-Renaud, U., 1989. Age U-Pb à 620 Ma d'un pluton synorogénique de l'Adrar des Iforas (Mali) Conséquences pour l'âge de la phase majeure de l'orogenèse Pan-Africaine. *C. R. Acad. Sci. Paris* 308, 307–314.
- Caby, R., Monié, P., 2003. Neoproterozoic subductions and differential exhumation of western Hoggar (southwest Algeria): new structural, petrological and geochronological evidence. *J. Afr. Earth Sci.* 37, 269–293.
- Caby, R., Buscail, F., 2005. Notice explicative de la carte géologique de l'Adrar des Iforas au 1/200 000. Direction Nationale de la Géologie et des Mines, Bamako Mali, 194 pp.
- Caby, R., Andreopoulos-Renaud, U., Lancelot, J.R., 1985. Les phases tardives de l'orogenèse Pan-Africaine dans l'Adrar des Iforas oriental (Mali): lithostratigraphie des formations molassiques et géochronologie U-Pb sur zircon de deux massifs intrusifs. *Precambrian Res.* 28, 187–199.
- Caby, R., Andreopoulos-Renaud, U., Pin, C., 1989. Late Proterozoic arc-continent and continent-continent collision in the Pan-African Trans-Saharan belt of Mali. *Can. J. Earth Sci.* 26, 1136–1146.
- Caby, R., Buscail, F., Dembélé, D., Diakité, Sacko, S., Bal, M., 2008. Neoproterozoic garnet-glaucophanites and eclogites: new insights for subduction metamorphism of the Gourma fold- and -thrust belt (eastern Mali). In: Ennih, N., Liégeois, J.-P. (Eds.), *The Boundaries of the West African Craton*, 297. *Geol. Soc. Spec. Pub.*, London, pp. 204–216.
- Champenois, M., Boullier, A.M., Sautter, V., Wright, L., Barbey, P., 1987. Tectonometamorphic evolution of the gneissic Kidal assemblage related to the Pan-African thrust tectonics (Adrar des Iforas Mali). *J. Afr. Earth Sci.* 6, 19–28.
- Chauvel, C., Blichert-Toft, J., 2001. A Hafnium isotope and trace element perspective on melting of the depleted mantle. *Earth Planet. Sci. Lett.* 388, 48–58.
- Danderfer, A., De Waele, B., Pedreira, A., Nalini, H., 2009. New geochronological constraints on the geological evolution of Espinhaco basin within the São Francisco Craton-Brazil. *Precambrian Res.* 170, 116–128.
- Darling, J.R., Storey, C.D., Engi, M., 2012. Allanite U-Th-Pb geochronology by laser ablation ICPMS. *Chem. Geol.* 292, 103–115.
- Davison, I., (Ph.D. thesis) 1980. A tectonic petrographical and geochronological study of a Pan-African belt in the Adrar des Iforas and Gourma, Mali. University of Leeds, England.
- Dhuime, B., Bosch, D., Bruguier, O., Caby, R., Pourtales, S., 2007. Age, provenance and post-deposition metamorphic overprint of detrital zircons from the Nathorst Land Group (NE Greenland) – a LA-ICP-MS and SIMS study. *Precambrian Res.* 155, 24–46.
- Dhuime, B., Bosch, D., Garrido, C.J., Bodinier, J.L., Bruguier, O., Hussain, S.S., Dawood, H., 2009. Geochemical architecture of the lower- to middle-crustal section of a paleo-island Arc (Kohistan complex, Jijal-Kamila area Northern Pakistan): implications for the evolution of an oceanic subduction zone. *J. Petrol.* 50, 531–569.
- Dimalanta, C., Taira, A., Yumil Jr., G.P., Tokuyama, H., Mochizuk, K., 2002. New rates of western Pacific island arc magmatism from seismic and gravity data. *Earth Planet. Sci. Lett.* 202, 105–115.
- Dostal, J., Dupuy, C., Caby, R., 1994. Geochemistry of the Neoproterozoic Tilemsi belt of Iforas (Mali Sahara) – a crustal section of an oceanic island-arc. *Precambrian Res.* 65, 55–69.
- Doukouri, S.A., Ouzegane, K., Arab, A., Kienast, J.R., Godard, G., Draren, A., Zetoutou, S., Liégeois, J.P., 2014. Phase relationships and P-T path in NCFMASHTO system of the eclogite from the Tighsi area (Egere terrane, Central Hoggar, Algeria). *J. Afr. Earth Sci.*, <http://dx.doi.org/10.1016/j.jafrearsci.2014.02.016>.
- El Hadi, H., Simancas, J., Martinez-Poyatos, D., Azor, A., Tahiri, A., Montero, P., Fanning, C., Bea, F., Gonzalez-Lodeiro, F., 2010. Structural and geochronological constraints on the evolution of the Bou Azzer Neoproterozoic ophiolite (Anti-Atlas Morocco). *Precambrian Res.* 182, 1–14.
- Ferkous, K., Monié, P., 2002. Neoproterozoic shearing and auriferous hydrothermalization along the lithospheric N-S East In Ouzzal shear-zone (Western Hoggar, Algeria North Africa). *J. Afr. Earth Sci.* 35, 399–415.
- Feeza, N., Liégeois, J.P., Abdallah, N., Cherfouh, E.H., De Waele, B., Bruguier, O., Ouabadi, A., 2010. Late Ediacaran geological evolution (575–555 Ma) of the Djian Terrane, Eastern Hoggar Algeria, evidence for a Murzukian intracontinental episode. *Precambrian Res.* 180, 299–327.
- Ganade de Araujo, C.E., Rubatto, D., Hermann, J., Cordani, U.G., Caby, R., Basei, M.A.S., 2014. Ediacaran 2,500-km-long synchronous deep continental subduction in the West Gondwana Orogen. *Nature*, <http://dx.doi.org/10.1038/ncomms6198>.
- Garrido, C.J., Bodinier, J.L., Dhuime, B., Bosch, D., Chanefo, I., Bruguier, O., Hussain, S.S., Dawood, H., Burg, J.P., 2007. Origin of the Island Arc Moho transition zone via melt-rock Reaction and its implications for intracrustal differentiation of island arcs: evidence from the Jijal complex (Kohistan complex N. Pakistan). *Geology* 35, 683–686.
- Haddoum, H., Choukroune, P., Peucat, J.J., 1994. Evolution of the Precambrian In-Ouzzal block (Central Sahara Algeria). *Precambrian Res.* 65, 155–166.
- Henry, B., Liégeois, J.P., Derder, M.E.M., Bayou, B., Bruguier, O., Ouabadi, A., Belhai, D., Amenna, M., Hemmi, A., Ayache, M., 2009. Repeated granitoid intrusions during the Neoproterozoic along the western boundary of the Saharan metacraton, Eastern Hoggar, Tuareg shield, Algeria: an AMS and U-Pb zircon age study. *Tectonophysics*, 417–434.
- Horstwood, M.S.A., Forster, G.L., Parrish, R.R., Noble, S.R., Nowell, G.R., 2003. Common Pb corrected in situ U-Pb accessory mineral geochronology by LA-ICP-MS. *J. Anal. Atom. Spectrom.* 18, 837–846.
- Irvine, T.N., Baragar, W.R.A., 1971. A guide to the chemical classification of the common volcanic rocks. *Can. J. Earth Sci.* 8, 481–497.
- Lancelot, J.R., Vitrac, A., Allegre, C.J., 1976. Uranium and lead isotopic dating with grain by grain zircon analysis: a study of complex geological history with a single rock. *Earth Planet. Sci. Lett.* 29, 357–366.
- Lancelot, J.R., Boullier, A.M., Maluski, H., Ducrot, J., 1983. Deformation and related radiochronology in a late Pan-African mylonitic shear zone, Adrar des Iforas, Mali. *Contrib. Mineral. Petrol.* 82, 312–326.
- Le Bas, M.J., Le Maître, R.W., Streckeisen, A., Zanettin, B., 1986. A chemical classification of volcanic rocks based on the total alkali-silica diagram. *J. Petrol.* 27, 745–750.
- Leterrier, J., Bertrand, J.M., 1986. Pretectonic tholeitic volcanism and related transitional plutonism in the Kidal assemblage (Iforas Pan-African Belt Mali). *J. Afr. Earth Sci.* 5, 607–615.
- Liégeois, J.P., 1988. La batholite composite de l'Adrar des Iforas (Mali). *Academie Royale des Sciences d'Outre-Mer. Classe Sci. Nat. et Med. Mémoire* 8. *Sci. Geol.* 22, 231.
- Liégeois, J.P., Black, R., 1987. In: *Alkaline Igneous Rocks*, J.G., Fitton, B.J., Upton, G. (Eds.), *Alkaline magmatism subsequent to collision in the Pan-African belt of the Adrar des Iforas (Mali)*, 30. *Geol. Soc. Spec. Pub.*, London, pp. 381–401.
- Liégeois, J.P., Bertrand, J.M., Black, R., 1987. The subduction- and collision-related Pan-African composite batholith of the Adrar des Iforas (Mali): a review. *Geol. J.* 22, 185–211.
- Liégeois, J.P., Diombara, D., Black, R., 1996. In: Michot, J., Demaiffe, D. (Eds.), *The Tessalit ring complex (Adrar des Iforas, Malian Tuareg Shield): a Pan-African, post-collisional, syn-shear, alkaline granite intrusion Petrology geochemistry of magmatic suites of rocks in the continental oceanic crust*. ULB-MRAC, Brussels, pp. 227–244.
- Liégeois, J.P., Navez, J., Hertogen, J., Black, R., 1998. Constrasting origin of post-collisional high-K calc-alkaline and shoshonitic versus alkaline and peralkaline granitoids. *Lithos* 45, 1–28.
- Liégeois, J.P., Latouche, L., Bougrara, M., Navez, J., Guiraud, M., 2003. The LATEA metacraton (Central Hoggar, Tuareg Shield Algeria): behaviour of an old passive margin during the Pan-African orogeny. *J. Afr. Earth Sci.* 37, 161–190.
- Liégeois, J.P., Abdelsalam, M.G., Ennih, N., Ouabadi, A., 2013. Metacraton: nature, genesis and behavior. *Gondwana Res.* 23, 220–237.
- Ludwig, K.R., 2000. User's manual for Isoplot/Ex v.2.3. A geochronological toolkit for Microsoft Excel. Berkeley Geochronology Center Special Publication N°1a, Berkeley, CA.

- Maluski, H., Monié, P., Kienast, J.R., Rahmani, A., 1990. Location of extraneous argon in granulitic-facies minerals: a paired microprobe-laser probe  $^{40}\text{Ar}^{39}\text{Ar}$  analysis. *Chem. Geol.* 80, 193–217.
- McDonough, W.F., Sun, S.S., 1995. The composition of the Earth. *Chem. Geol.* 120, 223–253.
- Nouar, O., Henry, B., Liégeois, J.P., Derder, M.E.M., Bayou, B., Bruguier, O., Ouabadi, A., Amenna, M., Hemmi, A., Ayache, M., 2011. Eburnean and Pan-African granitoids and the Raghane mega-shear zone evolution: image analysis, U–Pb zircon age and AMS study in the Arokam Ténéré (Tuareg shield Algeria). *J. Afr. Earth Sci.* 60, 133–152.
- Oberli, F., Meier, M., Berger, A., 2004. U–Th–Pb and Th-230/U-238 disequilibrium isotope systematics: precise accessory mineral chronology and melt evolution tracing in the Alpine Bergell intrusion. *Geochim. Cosmochim. Acta* 68, 2543–2560.
- Ouzegane, K., Kienast, J.-R., Bendaoud, A., Drareni, A., 2003. A review of Archaean and Paleoproterozoic evolution of the In Ouzzal granulitic terrane (Western Hoggar Algeria). *J. Afr. Earth Sci.* 37, 207–227.
- Paquette, J.L., Caby, R., Djouadi, M.T., Bouchez, J.L., 1998. U–Pb dating of the Pan-African orogeny in the Tuareg shield: the post-collisional syn-shear Tiouine pluton (western Hoggar Algeria). *Lithos* 45, 245–253.
- Pearce, J., 2008. Geochemical fingerprinting of oceanic basalts with applications to ophiolite classification and the search for Archean oceanic crust. *Lithos* 100, 14–48.
- Pearce, J.A., Peate, D.W., 1995. Tectonic implications of the composition of volcanic arc magmas. *Annu. Rev. Earth Planet. Sci.* 23, 251–285.
- Peucat, J.J., Capdevila, R., Drareni, A., Choukroune, P., Fanning, C.-M., Bernard-Griffiths, J., Fourcade, S., 1996. Major and trace element geochemistry and isotope (Sr, Nd, Pb, O) systematic of an Archaean basement involved in 2.0 Ga very high-temperature (1000 °C) metamorphic event: In Ouzzal Massif, Hoggar, Algeria. *J. Met. Geol.* 14, 667–692.
- Pidgeon, R., 1992. Recrystallization of oscillatory zoned zircon—Some geochronological and petrological implications. *Contrib. Mineral. Petrol.* 110, 463–472.
- Rioux, M., Bowring, S., Dudas, F., Hanson, R., 2010. Intermediate to felsic middle crust in the accreted Talkeetna arc, the Alaska Peninsula and Kodiak Island, Alaska: an analogue for low-velocity middle crust in modern arcs. *Tectonics* 29, <http://dx.doi.org/10.1029/2009TC002541>.
- Rooney, A.D., Selby, D., Houzay, J.P., Renne, P.R., 2010. Re-Os geochronology of a Mesoproterozoic sedimentary succession, Mauritania: implications for basinwide correlations and Re-Os organic-rich sediment systematics. *Earth Planet. Sci. Lett.* 289, 486–496.
- Rudnick, R.L., Fountain, D.M., 1995. Nature and composition of the continental crust—a lower crustal perspective. *Rev. Geophys.* 33, 267–309.
- Stepanov, A.S., Hermann, J., Rubatto, D., Rapp, R.P., 2012. Experimental study of monazite/melt partitioning with implications for the REE Th and U geochemistry of crustal rocks. *Chem. Geol.* 300, 200–220.
- Steiger, R.H., Jager, E., 1977. Subcommission on geochronology: convention on the use of decay constants in geo- and cosmo-chronology. *Earth Planet. Sci. Lett.* 36, 359–362.
- Stern, R.J., 2002. Crustal evolution in the East African Orogen: a neodymium isotopic perspective. *J. Afr. Earth Sci.* 34, 109–117.
- Stern, R.J., Johnson, P., 2010. Continental lithosphere of the Arabian Plate: a geologic, petrologic, and geophysical synthesis. *Earth Sci. Rev.* 101, 29–67.
- Tshibududze, A., Hein, K., Peters, L., Woolfe, A., McCuaig, T., 2013. Oldest U–Pb crystallisation age for the West African Craton from the Oudalan–Goroul belt of Burkina Faso. *South Afr. J. Geol.* 116, 169–181.
- Vavra, G., Schmid, R., Gebauer, D., 1999. Internal morphology, habit and U–Th–Pb microanalysis of amphibolite-to-granulite facies zircons: geochronology of the Ivrea zone (Southern Alps). *Contrib. Mineral. Petrol.* 134, 380–404.
- Wiedenbeck, M., Alle, P., Corfu, F., Griffin, W.L., Meier, M., Oberli, F., Von Quadt, A., Rudi, J.C., Spiegel, W., 1995. Three natural zircon standards for U–Th–Pb Lu–Hf, trace element and REE analyses. *Geostand. Newslett.* 19, 1–23.
- Williams, I.S., Claesson, S., 1987. Isotopic evidence for the Precambrian provenance and Caledonian metamorphism of high-grade paragneiss from the Seve Nappes, Scandinavian Caledonides. *Contrib. Mineral. Petrol.* 97, 205–217.
- Zhao, G., Cawood, P.A., Wilde, S.A., Sun, M., 2002. Review of global 2.1–1.8 Ga orogens: implications for a pre-Rodinia supercontinent. *Earth Sci. Rev.* 59, 125–162.